MSEAS-02

Modeling Coupled Physics and Biology in Ocean Straits with Application to the San Bernardino Strait in the Philippine Archipelago

by

Lisa Janelle Burton
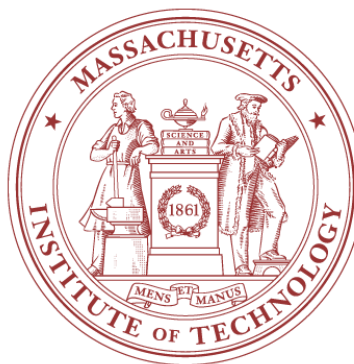
**Department of Mechanical Engineering
Massachusetts Institute of Technology**

Cambridge, Massachusetts

May 2009

Modeling Coupled Physics and Biology in Ocean Straits with Application to the San Bernardino Strait in the Philippine Archipelago

by

Lisa Janelle Burton

B.S.E., Duke University (2007)

Submitted to the Department of Mechanical Engineering
in partial fulfillment of the requirements for the degree of

Master of Science in Mechanical Engineering

at the

MASSACHUSETTS INSTITUTE OF TECHNOLOGY

June 2009

Author . . . .
Department of Mechanical Engineering
May 20, 2009

Certified by. . . . .
Pierre Lermusiaux
Associate Professor of Mechanical Engineering
Thesis Supervisor

Accepted by . . . .
David E. Hardt
Chairman, Department Committee on Graduate Theses

Modeling Coupled Physics and Biology in Ocean Straits with Application to the San Bernardino Strait in the Philippine Archipelago

by

Lisa Janelle Burton

Submitted to the Department of Mechanical Engineering
on May 20, 2009, in partial fulfillment of the
requirements for the degree of
Master of Science in Mechanical Engineering

Abstract

In this thesis, we conduct research toward understanding coupled physics-biology processes in ocean straits. Our focus is on new analytical studies and higher-order simulations of idealized dynamics that are relevant to generic biological processes. The details of coupled physics-biology models are reviewed and an in-depth global equilibrium and local stability analysis of a Nutrient-Phytoplankton-Zooplankton (NPZ) model is performed. This analysis includes parameter studies and methods to evaluate parameter sensitivity, especially in the case where some system parameters are unknown. As an initial step toward investigating the interaction between physics and biology in ocean straits, we develop and verify a new coupled physics-biology model for two-dimensional idealized physical processes including tides and apply it to the San Bernardino Strait in the Philippine Archipelago. This two-dimensional numerical model is created on a structured grid using operator splitting and masking. This model is able to accurately represent biology for various physical flows, including advection-dominated flows over discontinuities, by using the Weighted Essentially Non-Oscillatory (WENO) scheme. The numerical model is verified against a Discontinuous-Galerkin (DG) numerical scheme on an unstructured grid. Several simulations of tidal flow are completed using bathymetry and flow magnitudes comparable to those found in the San Bernardino Strait with different sets of parameters, tidal periods, and levels of diffusion. Results are discussed and compared to those of a three-dimensional modeling system. New results include: new methods for analyzing stability, the robust two-dimensional model designed to best represent advection-dominant flows with minimal numerical diffusion and computational time, and a novel technique to initialize three-dimensional biology fields using satellite data. Additionally, application of the two-dimensional model with tidal forcing to the San Bernardino Strait reveals that flow frequencies have strong influence on biology, as very fast oscillations act to stabilize biology in the water column, while slower frequencies provide sufficient transport for increased biological activity.

3

Thesis Supervisor: Pierre Lermusiaux
Title: Associate Professor of Mechanical Engineering

Acknowledgments

I would like to thank my family and friends for their constant support. Andrew, thank you for patiently reading each draft of this thesis and providing very useful criticism and ideas. Thank you for taking an interest in my work and pushing me to think more critically about my research. Last, but certainly not least, thank you for teaching me every MATLAB trick I'll ever need to know.

Mom and Luis, thank you for always having the right words to encourage me when I needed it most and for being proud of me, no matter what endeavors I pursue. Dad, thanks for always being so positive and putting things in perspective for me. Lauren, thank you for always being there for me. Thanks to my grandparents, aunts, uncles, and cousins. I'm so fortunate to have such an amazing family.

I would like to thank my advisor, Pierre, for his technical assistance and guidance with this thesis. His leadership started me on the path for this research and his enthusiasm and encouragement sustained these research efforts. Thank you to Pat for his help and patience teaching me how to work with MSEAS, for providing the biological results for the Philippines, and for the description of MSEAS. Thanks to Wayne for helping me find and make sense of data and to Oleg for useful discussions about tides and how to implement masking and the C-grid. Thanks to Themis for his passion and advice for both dynamical systems, to Matt for his potential flow and Discontinuous Galerkin code and to Arpit for his Objective Analysis plots. To all of the MSEAS group members, thanks for your discussions and constructive criticism of my research during the past two years.

Project for the Sea Surface Height anomalies and Sherwin Ladner and Bob Arnone of NRL-SSC for Sea Surface Temperature imagery.

Contents

List of Figures

10

14

List of Tables

Chapter 1

Introduction

1.1 Motivation and Background

Ocean straits and archipelagos create complex physical domains, resulting in processes spanning many time and spatial scales. These conditions lead to interesting biological phenomena, including diverse blooms of biota. Identifying which processes and conditions are necessary and sufficient for such blooms to occur is a challenging task, especially in domains as complicated as archipelagos. By isolating processes, we can improve our understanding of the relationship between physical processes and biology. We conduct research toward understanding coupled physics-biology processes in ocean straits through new analytical studies and higher-order simulations of idealized dynamics that are relevant to generic biology in straits. Specifically, we first characterize global equilibrium properties and the local stability of biological reaction equations in a non-diffusive framework without flow. We then develop and utilize a new higher-order numerical scheme for two-dimensional simulations of coupled physical-biological dynamics over straits, with a focus on tidal effects. We study tidal effects because they often strongly determine flow in straits at diurnal and semidiurnal periods, but their oscillations may be too fast for certain biological reactions.

Our research efforts are a part of the Philippines Experiment, or *PhilEx*, a five-year joint research project focused on interdisciplinary modeling, data assimilation

and dynamical studies in the straits regions of the Philippine Archipelago to better understand, model and predict sub-mesoscale and mesoscale physical and biogeochemical dynamics in sea straits. The three-dimensional ocean model fields and measurements from *PhilEx* are used in this study. Gathering biological data is frequently done by capturing water samples, using underwater vehicles, or instruments attached to a research vessel, which leads to sparse data fields in space and time. Previous research and data is scarce in the Philippines, therefore initializing models is challenging. We thus develop a new method to initialize coupled physics-biology with sparse initial data.

The Philippines region has very interesting dynamics including a wide range of physical processes, a seasonal monsoon, and transport through straits from various ocean basins. The San Bernardino Strait in the Philippines connects the Visayan Sea with the Pacific Ocean. Experimental data suggests that the San Bernardino Strait hinders flow of intermediate and deep waters from entering the archipelago [41]. Tides in this region reduce the mean flow through the strait by nonlinear rectification [27], which causes considerable phase and amplitude shifts [37]. Both topography and intense tidal mixing are strongly influential in this strait [27]. Thus, the topography and flow from the San Bernardino Strait in the Philippine Archipelago is used to create realistic test cases. The location of the San Bernardino Strait within the Philippine Archipelago is shown in Figure 1-1.

Previous research on the topic of tides and biology shows that tidal mixing produces increased biomass. This research has been performed both experimentally and theoretically, though it is difficult to sample biology fine enough to resolve some of the features predicted. Tidal effects on biology have been primarily explored in the open ocean [5], [19], fjords [31], banks [21] and estuaries [50]. These studies examine the source of dense biomass concentrations due to tidal pumping and forcing. Aside from straits with both historical data and thorough understanding of the tidal effects, such as the Strait of Gibraltar [39], no research has been conducted, to the author's knowledge, on the topic of general biology in ocean straits including coupled biology-tidal effects. The work completed in this thesis is an initial step to understanding

Figure 1-1: The San Bernardino Strait connects the Visayan Sea with the Pacific Ocean in the Philippine Archipelago.

the relationship between biology and tidal frequency, in particular the interactions of tidal scales and biological scales over bathymetry.

1.2 General Modeling Content

Part of our work is linked to the *PhilEx* research conducted by the MSEAS group. For this research, the MIT Multidisciplinary Simulation, Estimation, and Assimilation Systems (MSEAS) [2] is utilized. It consists of a set of mathematical models and computational methods for ocean predictions and dynamical diagnostics, for optimization and control of autonomous ocean observation systems, and for data assimilation and data-model comparisons. MSEAS is used for basic and fundamental research and for realistic simulations and predictions in varied regions of the world's ocean, recently including monitoring [35], naval exercises including real-time acoustic-ocean predictions [59] and environmental management [11]. Several different models are included in the system, including a free-surface primitive-equation dynamical model

which uses two-way nesting free-surface and open boundary condition schemes [26]. This new free-surface code is based on the primitive-equation model of the Harvard Ocean Prediction System (HOPS). Additionally, barotropic tides are calculated from the inverse tidal model [38].

For *PhilEx*, the modeling domains include three different resolution sizes. The smallest domains have $1km$ resolution and are nested inside $3km$ resolution domains, which are nested in our largest domain (with a $9km$ resolution). These domains are shown in Figure 1-2.
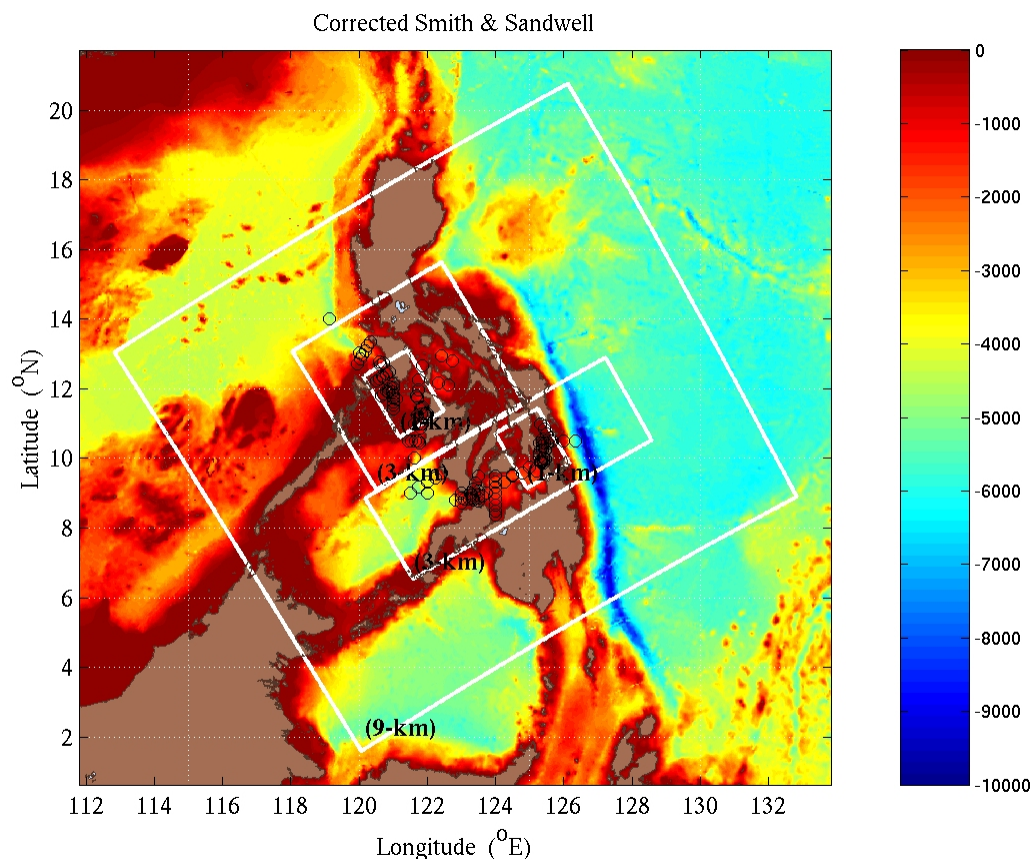
Figure 1-2: Nested domains used in MSEAS for *PhilEx*. Three different resolution sizes are used ($1km$, $3km$, and $9km$).

MSEAS is used to estimate the evolution of physical and biological three-dimensional ocean fields [42]. One example of a typical estimate is Figure 1-3, showing sea surface temperature in the Philippines. Physical variables computed include velocity,

temperature and salinity. Biological variables depend on the biological model used.

1.3 Thesis Overview

In Chapter 2, we discuss physical and biological models. For the biology, Nutrient-Phytoplankton-Zooplankton (NPZ) models (for a two-dimensional simulation) and more complex biogeochemical models (for a three-dimensional simulation) are discussed. To determine parameter limitations and sensitivity, we perform new global equilibrium and local stability analyses in Chapter 3 of the biological reaction equations in a non-diffusive, conservative framework without physics. General analytical methods to determine equilibria and stability properties for a parameter set are developed and demonstrated. Conditions necessary for stability and instability are discussed and application to the domain including advection and diffusion is presented. To study idealized coupled physical and biological dynamics accurately, we implement and compare various numerical schemes in Chapter 4 to identify high-order schemes with low numerical diffusion able to represent a wide range of processes, including the advection dominant case (which is prone to oscillations). All details of the development of the simulation are outlined and the result is a new scheme resistant to oscillations with easy implementation of boundary conditions and low numerical diffusivity. In Chapter 5, we use this numerical scheme to study the effects of tides in a two-dimensional strait-like domain, varying biological parameters, tidal frequency, and levels of diffusion. We then present our new approaches for the initialization of a three-dimensional biological model in MSEAS using sparse data which is based on region-specific analytic chlorophyll profiles. The biology fields are compared to the two-dimensional fields. All results are reviewed and summarized in Chapter 6.
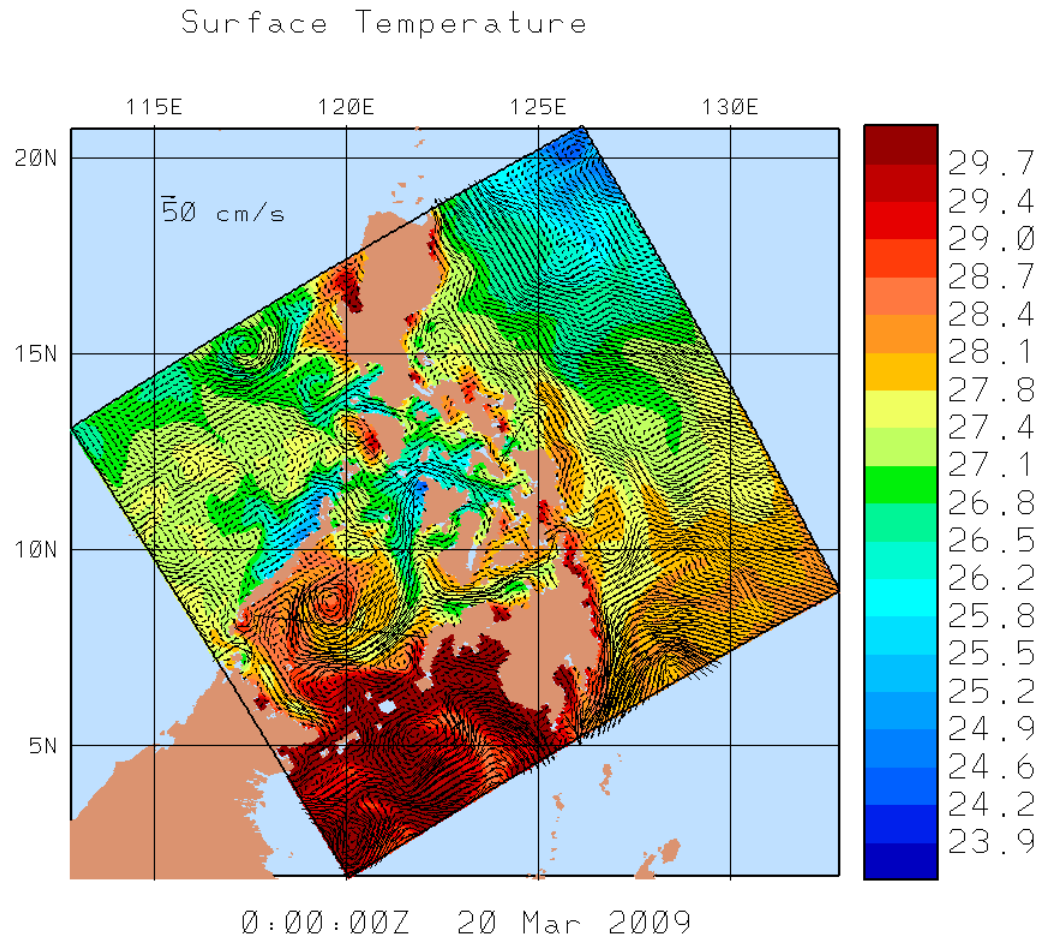
Figure 1-3: An example output from MSEAS showing surface temperature and current for the archipelago domain. Cross-sectional plots are also produced along select straits [43].

Chapter 2

Modeling Physics and Biology

In this chapter, we discuss details of coupled physics-biological modeling. Models of varying levels of complexity are explored and two models are selected for analysis in subsequent chapters. The first model described is a simplified NPZ (Nutrient-Phytoplankton-Zooplankton) model for an idealized system in two spatial dimensions. This model allows closed form analytic results that reveal important characteristics of the system and allow parameter sensitivity studies. The second model described is significantly more complex, including additional biological and chemical variables. This later model is sufficiently sophisticated to provide accuracy and precision required for three dimensional modeling using MSEAS. We show that these models are appropriate tools to use for an initial assessment of the relationship between physics and biology. Various ways to represent biological processes are compared and discussed.

2.1 Biology in the Ocean

Unlike most physical systems, equations to model biological systems in the ocean have not yet been derived from first principles and conservation laws. Instead, the governing equations for biological systems are built from observations. These empirical equations often contain several region-specific parameters to describe growth rates, death rates, and other processes [16]. While the equations model *how* the state

variables interact, the parameters control the characteristics of interaction, including the *rates* of growth or death.

To study the relationship between physics and biology, it is common to examine the lower trophic levels of biology. Modeling is often limited to an isolated part of the food web, such as the cycle between nutrients, phytoplankton, and zooplankton. Phytoplankton feed on nutrients and are consumed by zooplankton. When zooplankton die, bacteria eventually convert the zooplankton back to nutrients. The growth rate of each of these organisms is dependent on the environment and the specific quantities of the other organisms. As such, the relationship between the different organisms is highly coupled. The presence or absence of one organism determines the growth possible by another.

The relationships which represent biological interaction between organisms, called *reaction* or *source* terms, can be expressed in various ways and depend on several parameters. These parameters, discussed in Section 2.2, can be a function of space and time and are region-dependent. Sufficient data is needed to specify temporal and spatial variation of parameters. Temporal variations include seasonal, weekly, or daily scales and examples of spatial variations include varying parameters from one region to another, or in depth. For the present research, we are interested in parameters appropriate for the Philippines but we will start with constant parameters because of sparse data in this region.

Environmental factors important to biological growth include light (solar irradiance), bottom depth, availability of nutrients and physical processes such as turbulence, internal waves, and eddy transport [17]. These factors can directly affect single or multiple state variables. (A *biological state variable* is usually the biomass concentration of an organism such as zooplankton, phytoplankton, and nutrients.) For instance, only phytoplankton require light. They must live near the ocean surface to absorb light for photosynthesis. Experiments in some regions have shown that phytoplankton growth can be hindered by too little or *too much* light. Because phytoplankton require light, there exists a critical depth where insufficient sunlight eliminates the possibility of phytoplankton (and thus zooplankton) growth, assuming

a domain without flow. *Critical depth* is defined as the depth where photosynthetic gain of phytoplankton cells are balanced by respiratory losses, which can be different than the depth of the *euphotic zone*, where light is sufficient to support plant growth [33].

If flow, such as a downward vertical velocity or diffusion, is present, phytoplankton may be transported from above the critical depth down to light-deficient areas, in which case the depth of the euphotic zone and the critical depth do not coincide. These depths vary highly with location, depending on the local turbidity of the water and the attenuation of light with depth. In Chapter 3, we discuss the validity of critical stability depth (found in the reference frame without physics) when advection and diffusion are present. In general, in open ocean conditions, the greatest local variation in biomass is in vertical distribution because of light-dependence and ocean flows, which are commonly much stronger in the horizontal direction than in the vertical.

Only some species of plankton are capable of independent vertical movement. Excluding these, plankton and nutrients act as passive tracers in the flow because their self-movement in comparison to the flow is negligible [18]. Therefore biology, which act as passive tracers, can be good indicators of flow direction and strength. Physical processes that increase vertical velocities and mixing often produce interesting biological behaviors. We will model physical processes by considering advection (transport by ocean currents) and diffusion (mixing processes) [17]. When nutrient-rich waters are upwelled, a more productive environment is created because phytoplankton gain access to these nutrients. Predicting and understanding processes such as upwelling is key in understanding how changing conditions will affect marine life, an important food source to the world. Currently, regions of coastal upwelling are responsible for approximately half of the fish harvest in the world, though they only occupy 0.1% of the ocean's surface area [12]. Further, advection and diffusion can raise or lower the critical depth (compared to the critical depth of the physics-free reference frame). Consider an extreme case with very high diffusion. High rates of mixing create an averaged field, so that the concentration of phytoplankton at the surface matches

the value at the ocean floor. Therefore, no critical depth exists and phytoplankton growing at one depth are transported quickly to the entire water column.

Although we are only considering lower trophic levels in our models, the behavior and trends are indicative of higher trophic levels. The relationship between the two is sometimes extremely short. For example, whales consume krill (a type of zooplankton), which consume phytoplankton. All higher trophic level activity depends on these primary producers. In general, we assume zooplankton are consumed by fish, which are either caught by man or eventually recycled into nutrients [16].

2.2 Two-dimensional Idealized Case: Nutrient-Phytoplankton-Zooplankton Model

There are several types of biological ocean models ([49], [30]). We focus on the NPZ (Nutrient-Phytoplankton-Zooplankton) food-web model for our idealized simulation. It is a concentration-based model, with nitrogen or carbon as a currency. An NPZ model is chosen because it is one of the most basic ways to represent the biological-physical interactions for lower trophic levels [20]. NPZ models accurately represent a wide range of biological behaviors, as evidenced by many example of successful usage, both quantitatively and qualitatively. NPZ models are not commonly used for predictive purposes, but are useful in understanding past trends and behaviors. NPZ models are appropriate for mesoscale physical processes because of matching time scales with biological interactions.

The NPZ model preserves first order interactions, but is simplified enough to permit analytic, closed form results with or without numeric methods. An NPZ model assumes that zooplankton feed on phytoplankton, which feed on nutrients. Zooplankton and phytoplankton each have a natural mortality rate. When zooplankton and phytoplankton die naturally, we assume that they directly become nutrients. Figure 2-1 shows a graphical representation of the NPZ model just described. Other food-web models that include additional compartments and complexities are used in

MSEAS. One of them is discussed in Section 2.3.
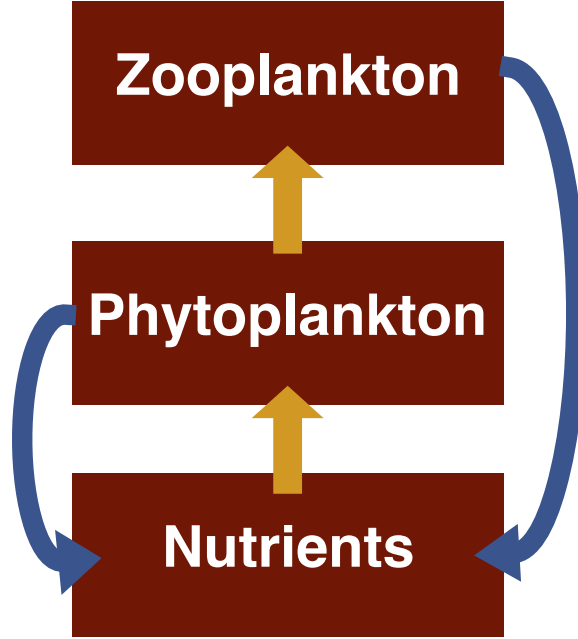
Figure 2-1: Schematic diagram of an NPZ model. The yellow up arrows indicate consumption and the blue down arrows indicate recycling into nutrients.

Empirical equations developed for these models are nonlinear. Consequently, no analytic solution exists. To better understand the biological dynamics of the NPZ model, the strongly nonlinear biological equations should first be understood in the reference frame without physics (advection or diffusion). The reference frame without physics can be compared to a closed ocean system where the fluid motion is not allowed and no mixing is present. Only the biological organisms are allowed to react. With parameters constant in space, the only variation is in depth because of the vertical light decay. In Chapter 3, we explore the stability and behavior of the biological equations without advection and diffusion, and test these behaviors when advection and diffusion are present.

2.2.1 Biological Field Equations

A typical NPZ biological system is represented by a set of generic Advection-Diffusion-Reaction (ADR) equations, with concentration of biomass (ϕ_i) acting as the state

Reaction term	Representation	Description
uptake(P,N)	$f(I)g(N)$	Phytoplankton response to irradiance & Phytoplankton nutrient uptake
grazing(P,Z)	$h(P)$	Zooplankton grazing on phytoplankton
death(P)	$i(P)$	Phytoplankton death rate
death(Z)	$j(Z)$	Zooplankton death rate
regeneration(P,Z)	$(1-\alpha)h(P)$	Inefficiency of zooplankton grazing
assimilation(P,Z)	$\alpha h(P)$	Efficiency of zooplankton grazing

Table 2.1: Descriptions of generic biological reaction terms

variable. The second term of Equation 2.1 is advection, the third diffusion, and the last term represents the collection of biological reaction terms.

$$\frac{\partial \phi_i}{\partial t} + \nabla \cdot (\mathbf{u}\phi_i) = \nabla \cdot \kappa \nabla \phi_i + \mathcal{B}(\phi_1, ..., \phi_i, ..., \phi_N) \tag{2.1}$$

where $(\phi_1...\phi_N)$ are the N state variables, κ is the diffusion coefficient, and $\mathbf{u}$ is the velocity vector. These equations are also valid for the more complex model described in Section 2.3.

$\mathcal{B}(\phi_1, \phi_2, ..., \phi_N)$ couples the equations for different organisms.

Biological reactions typically modeled in NPZ equations are described by [18] and [20] and summarized in Table 2.1. The reaction terms listed in the table can take many forms, depending on the relationship modeled. For instance, to model zooplankton death rate ($j(Z)$) and the phytoplankton response to irradiance ($f(I)$) several different relationships can be used and are shown in Figures 2-2 and 2-3. The curves in Figure 2-2 present reaction terms for zooplankton death rate for various level of complexity. It is clear that the nonlinear term models the same behavior of quadratic death rate for low concentrations of zooplankton and matches linear death rate for high concentrations of zooplankton, with a smooth transition in between for mid-range concentrations. Figure 2-3 demonstrates the response of phytoplankton to irradiance. Again, we see that adding complexity allows behavior at both low and high irradiance to be specified. The last curve (according to the legend) models a response for phytoplankton, which is sensitive to both too little and too much light.
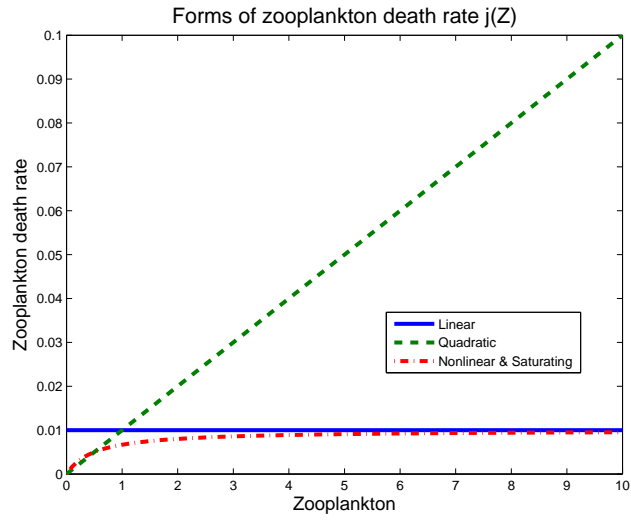
Figure 2-2: Various forms of zooplankton death rate versus concentration of zooplankton (mg/m^3).
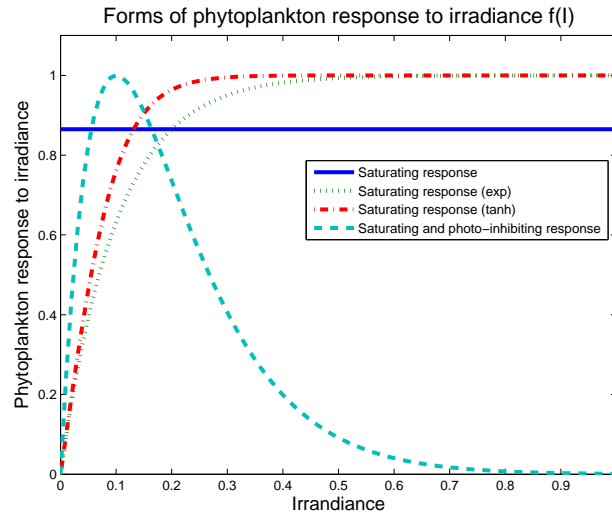
Figure 2-3: Phytoplankton response to irradiance versus non-dimensional levels of irradiance.

$$\frac{\partial N}{\partial t} + \nabla \cdot (\mathbf{u}N) = \nabla \cdot \kappa \nabla N - uptake\,(P,N) + regeneration\,(P,Z)$$
$$\frac{\partial P}{\partial t} + \nabla \cdot (\mathbf{u}P) = \nabla \cdot \kappa \nabla P + uptake\,(P,N) - grazing\,(P,Z) - death\,(P) \quad (2.2)$$
$$\frac{\partial Z}{\partial t} + \nabla \cdot (\mathbf{u}Z + w_z Z) = \nabla \cdot \kappa \nabla Z + assimilation\,(P,Z) - death\,(Z)$$

This set of three coupled, strongly nonlinear partial differential equations describe both the reaction due to biological interactions and the physics of the flow (advection and diffusion) using only one type of nutrient (N), phytoplankton (P), and zooplankton (Z). Understanding the simplest model is an important initial step, as complexities can be added later, for example, when a more complicated model is necessary or when the behavior is known from observational data.

More complicated models, as presented in Section 2.3, include additional compartments, such as detritus, chlorophyll, and multiple types of limiting nutrients, phytoplankton, and/or zooplankton. Note that the class of NPZ models discussed are conservative, in that the biological reaction terms sum to zero (any loss or gain of one compartment is accounted for in other compartments).

For an initial study of biological interactions, the forms for the biological terms are the same as those used in [18], which includes the Ivlev form of grazing and the Michaelis-Menten form for uptake.

$$\frac{\partial N}{\partial t} + \nabla \cdot (\mathbf{u}N) = \nabla \cdot \kappa \nabla N - ue^{z/h}\frac{PN}{N+k_s} + d_p P + d_z Z + (1-a)\frac{g}{\nu}Z\left(1-e^{-\nu P}\right)$$
$$\frac{\partial P}{\partial t} + \nabla \cdot (\mathbf{u}P) = \nabla \cdot \kappa \nabla P + ue^{z/h}\frac{PN}{N+k_s} - d_p P - \frac{g}{\nu}Z\left(1-e^{-\nu P}\right)$$
$$\frac{\partial Z}{\partial t} + \nabla \cdot (\mathbf{u}Z + w_z Z) = \nabla \cdot \kappa \nabla Z + a\frac{g}{\nu}Z\left(1-e^{-\nu P}\right) - d_z Z$$

$$(2.3)$$

Where the parameters in the above set of coupled equations are defined as:

u Phytoplankton uptake rate

k_s Saturation rate of phytoplankton

N_T Total biomass

d_p Mortality rate of phytoplankton

g Grazing rate of zooplankton (2.4)

a Assimilation (efficiency) rate

d_z Mortality rate of zooplankton

h e-folding depth for light (photosynthesis)

ν Parameter for Ivlev form of grazing

If we assume the zooplankton modeled is not a species which is capable of independent motion in the vertical direction, and if all physical advection and mixing coefficients are the same for all variables, the three coupled equations can be reduced to two by assuming a fixed biomass N_T and substituting $N = N_T - P - Z$.

$$
\begin{aligned}
\frac{\partial P}{\partial t} + \nabla \cdot (\mathbf{u}P) &= \nabla \cdot \kappa \nabla P + u e^{z/h} \frac{P(N_T - P - Z)}{N_T - P - Z + k_s} - d_p P - \frac{g}{\nu} Z \left(1 - e^{-\nu P}\right) \\
\frac{\partial Z}{\partial t} + \nabla \cdot (\mathbf{u}Z) &= \nabla \cdot \kappa \nabla Z + a \frac{g}{\nu} Z \left(1 - e^{-\nu P}\right) - d_z Z
\end{aligned}
\tag{2.5}
$$

For the idealized studies, Equations 2.5 are modeled for a two-dimensional vertical slice of the ocean. A stability analysis of Equations 2.5 is presented in Chapter 3.

2.3 Three-dimensional Realistic Case: Seven Compartment Biogeochemical Model

The ocean modeling system used, MSEAS, is a generic system designed for interdisciplinary nowcasting, forecasting, and data-driven simulations. MSEAS has been extensively verified in various regional experiments ([25],[36],[48]). The model uses

4D physics based on the Primitive Equations (PE) (see [6] for details).

MSEAS is capable of implementing several different biological models (discussed in [56]). The biological model used for this work couples with the physics and is governed by ADR equations for six state variables: zooplankton, detritus, nitrate, ammonium, chlorophyll a and phytoplankton. A schematic of this system is shown in Figure 2-4 from [6]. The biological reaction terms $\mathcal{B}(\phi_1, ..., \phi_i, ..., \phi_7)$ and corresponding parameters are shown in [6]. The added complexity of this model is apparent when Figures 2-1 and 2-4 are compared. From Figure 2-4, we can see that phytoplankton consumes both nitrate and ammonium, instead of just one nutrient, like in the NPZ model. Additionally, the model used in MSEAS includes detritus, chlorophyll and an optical model for solar irradiance.
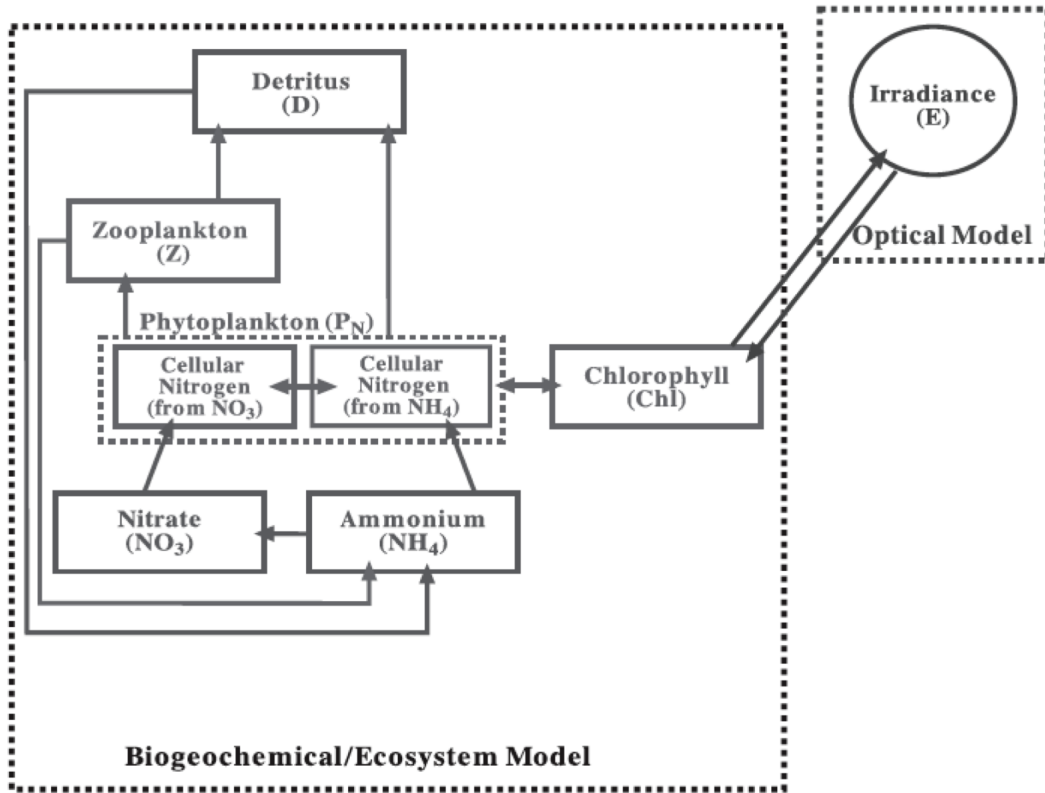
Figure 2-4: The biological model used in MSEAS [6].

A more complex model allows us to model additional processes and stages and is

often more realistic. However, it presents the challenge of initializing the system (now in three spatial dimensions and for six state variables, compared to two dimensions with three variables as in the NPZ model), and additional difficulty in understanding the strongly nonlinear coupled equations. While we were able to simplify Equation 2.3 to Equations 2.5, no such simplification is possible for the MSEAS model. Initialization of the system depends on the data available in the region of interest. Details on the initialization of the biological system for the Philippines domain are discussed in Chapter 5.

Both models chosen for analysis and simulation of coupled physics and biology have been previously tested and verified. Each has its advantages: the NPZ model offers the ability to obtain closed form solutions describing the system, while the model used in MSEAS is capable of modeling more complex, realistic behaviors. These models are thus appropriate tools to use for understanding the relationship between coupled physics and biology in the Philippine Archipelago, a region where relatively little data is available. However, after more information is known about the region, we may find it suitable to use different reaction terms or a different model that is more fitting.

Chapter 3

Stability and Equilibria of the Nutrient-Phytoplankton-Zooplankton Model

Understanding the detailed relationships between the state variables of Equation 2.3 solely by examining terms is very challenging. The biological reaction terms are strongly nonlinear and depend on parameters that may take different values for different regions. It is common to use coupled biological-physical models in regions where not all of the parameters are known. In this case, it is important to know which range of parameter values give physical solutions and which cause unstable or unrealistic solutions. Additionally, if parameters are estimated (either because they are unknown or because several different values have been recorded for a region), knowing how sensitive the equations are to a particular parameter indicates the necessary level of accuracy for the parameter estimates.

In this chapter, we consider the reference frame without physics (that is, advection or diffusion) to express important equilibrium and global stability properties in an *analytic, closed form* fashion, purely in terms of the system parameters. While numerical models are very powerful tools in simulating coupled physics and biology, an analytic stability analysis allows us to learn a substantial amount of global information quickly and easily by evaluating first-order dependencies and relationships

between parameters, stability, and equilibria. These results are particularly useful if some of the parameters are known so that there are fewer degrees of freedom to analyze. The use of Direct Numerical Simulation to obtain comparable global results would require significant time and effort to tune parameters and analyze test cases.

More specifically, Section 3.1 presents a novel global stability analysis of the biological equations (without advection or diffusion) conducted to evaluate the sensitivity of the strongly nonlinear equations to parameter values, behavior of the equilibria states, as well as appropriate ranges for the parameter values. In Section 3.2, we focus more on local stability, studying critical stability depths and presenting a new general method of stability analysis showing results for varying total amount of biomass concentration in the system (N_T). Lastly, the applicability of the stability analysis in the dynamics model (*including* physics) is addressed.

3.1 Equilibria Solutions and Regions

To obtain static equilibria solutions, we consider Equations 2.5 without advection or diffusion:

$$
\begin{aligned}
\frac{dP}{dt} &= ue^{z/h}\frac{P(N_T - P - Z)}{N_T - P - Z + k_s} - d_p P - \frac{g}{\nu}Z\left(1 - e^{-\nu P}\right) \\
\frac{dZ}{dt} &= a\frac{g}{\nu}Z\left(1 - e^{-\nu P}\right) - d_z Z
\end{aligned}
\tag{3.1}
$$

Note that these equations are identical to the biological equation in the Lagrangian frame, including advection, where $\frac{d}{dt}$ is the material derivative. Equations 3.1 are set to zero to solve for the steady equilibria. Once the system is in steady state, it does not change with time, so we set the time derivative to zero to solve for P and Z in this state. As mentioned in Chapter 2, we have constant total biomass N_T in the system if we assume there is no independent swimming zooplankton, so our nutrient equation is simply $N = N_T - P - Z$. These equations essentially represent how phytoplankton and zooplankton change in time due to the biological reaction terms

38

only. For biological modeling in a region with sufficient information, N_T may be modeled as varying in space (more commonly in depth only) or in time. In that case, the following analysis is appropriate for any point in time with constant biomass. Commonly, N_T is modeled as constant in space and time, in which case the analysis is valid in the entire field.

The steady state equations (Equations 3.1) give three sets of equilibria (Equations 3.2-3.4). The first equilibrium is:

$$
\begin{aligned}
N &= N_T \\
P &= 0 \\
Z &= 0
\end{aligned}
\tag{3.2}
$$

Equations 3.2 are the solutions we expect in deep waters where phytoplankton are unable to survive, thus zooplankton have nothing to feed on. Therefore, nutrients are responsible for the full biomass value. The second equilibrium is:

$$
\begin{aligned}
N &= -k_s - \frac{\beta(z)k_s}{d_p - \beta(z)} \\
P &= k_s + N_T + \frac{\beta(z)k_s}{d_p - \beta(z)} \\
Z &= 0
\end{aligned}
\tag{3.3}
$$

Equations 3.3 will always give negative amounts of biomass, an unphysical solution, and thus we are not interested in these steady state values. The third equilibrium is:

$$
\begin{aligned}
N &= N_T + \frac{\gamma}{\nu} - \rho \mp \sqrt{\rho^2 - s} \\
P &= -\frac{\gamma}{\nu} \\
Z &= \rho \pm \sqrt{\rho^2 - s}
\end{aligned}
\tag{3.4}
$$

where

$$\rho = \frac{1}{2}\left(k_s + N_T + \frac{\gamma}{\nu}\left(1 + \frac{a}{d_z}(d_p - \beta(z))\right)\right)$$

$$s = \frac{a\gamma}{d_z\nu}\left(d_p\left(\frac{\gamma}{\nu} + N_T + k_s\right) - \beta(z)\left(\frac{\gamma}{\nu} + N_T\right)\right)$$

$$\gamma = \ln\left(1 - \frac{d_z\nu}{ag}\right)$$

$$\beta(z) = ue^{z/h}$$

It is important to note that $\gamma \leq 0$ and $0 \leq \beta(z) \leq u$ because all parameters in Equation 3.1 are positive. Further, $\beta(z)$ can be thought of as a generalized depth that does not require specification of e-folding depth h (describing how light decays in depth) or uptake rate u. For near surface depths, $\lim_{z\to 0} \beta(z) = u$ while for depths far below the surface, $\lim_{z\to -\infty} \beta(z) = 0$.

Equations 3.4 are the most interesting because they represent the physically realistic biological equilibrium in the upper layer of the ocean. Altering the system parameters can change the equilibrium from positive to negative and real to imaginary. Knowing that γ is always non-positive and ν is always positive guarantees a positive value of phytoplankton equilibria. Phytoplankton equilibria is independent of depth z or $\beta(z)$, so this result is valid (positive and real) for the entire water column above the critical depth. Below the critical depth, phytoplankton cannot survive and nutrients dominate. More technically, the *critical depth* is the depth where photosynthetic gain of phytoplankton cells are balanced by respiratory losses [33]. Because of mixing, the critical depth does not necessarily correspond to the depth of the euphotic zone, where light is sufficient to support plant growth.

For initial analysis, we will use the parameter values used in [18] to study the behavior of the last set of equilibria. These values are:

$$u = 0.6\mu\text{mol day}^{-1}$$

$$N_T = 3\mu\text{mol L}^{-1}$$

$$k_s = 0.1\mu\text{mol day}^{-1}$$

$$d_p = 0.016\mu\text{mol day}^{-1}$$

$$g = 0.1\mu\text{mol day}^{-1} \tag{3.5}$$

$$a = 0.4$$

$$d_z = 0.08\mu\text{mol day}^{-1}$$

$$h = 17\text{m}$$

$$\nu = 0.1\mu\text{mol}^{-1}$$
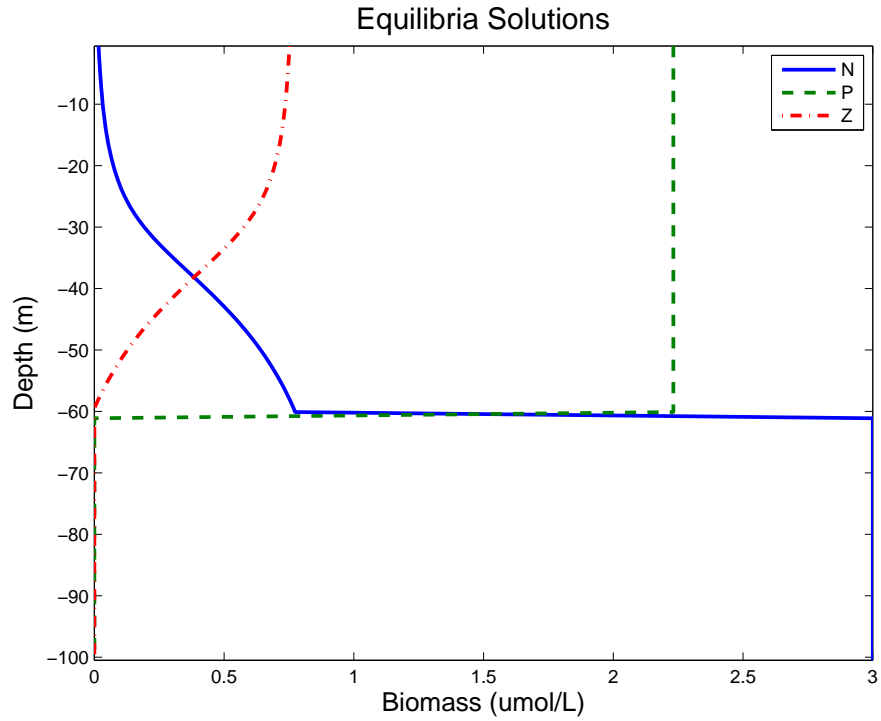
Figure 3-1: Equilibrium solution for N, P, and Z based on the parameters in Equation 3.5.

Figure 3-1 shows a one-dimensional (in depth) view of Equations 3.4. Even though

phytoplankton feeding decays in depth because they require light for photosynthesis, the phytoplankton equilibria do not vary with depth, until the solutions become unphysical and equilibria change. Below the critical depth, we impose the equilibria solution for deep water (Equation 3.2). In cases where the critical depth is known, that depth can be imposed directly. The variation in depth due to light decay is reflected in the distributions of nutrients and zooplankton: phytoplankton feed more slowly at lower depths, so more nutrients are available. In turn, zooplankton's prey (phytoplankton) is growing much more slowly at low depths, so it has less to feed on. These equilibria were verified numerically by allowing Equations 3.1 to reach steady state. The simulated profile in depth was identical to the analytical equilibrium in depth.
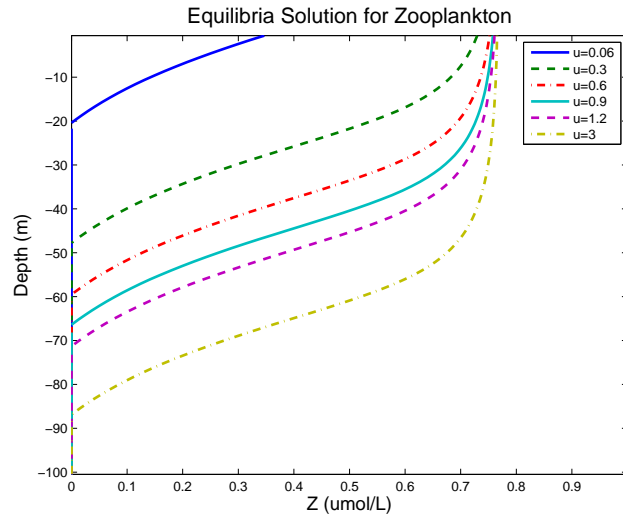
Figure 3-2: Equilibria solutions for Z for various values of phytoplankton uptake rate u.

Parameter values can alter the equilibrium solutions drastically. For example, Figure 3-2 illustrates the relationship between phytoplankton uptake rate u and zooplankton equilibrium. The result is intuitive: as phytoplankton uptake rate increases, phytoplankton consume nutrients more quickly, therefore there are more phytoplankton for zooplankton to prey on. The zooplankton equilibria change for all depth values, though for large uptake rate, the solution near the surface asymptotically

approaches a constant zooplankton value ($Z \to 0.75 \mu mol/L$). In contrast, varying assimilation rate a (Figure 3-3) alters the solution near the surface and for the two largest a values, the solution below $30m$ appears identical. Assimilation rate indicates how efficient zooplankton are in grazing on phytoplankton. It is clear that with nine parameters in a coupled strongly nonlinear system (each parameter corresponding to different behaviors), it is difficult to imply behavior and stability properties without careful analysis.
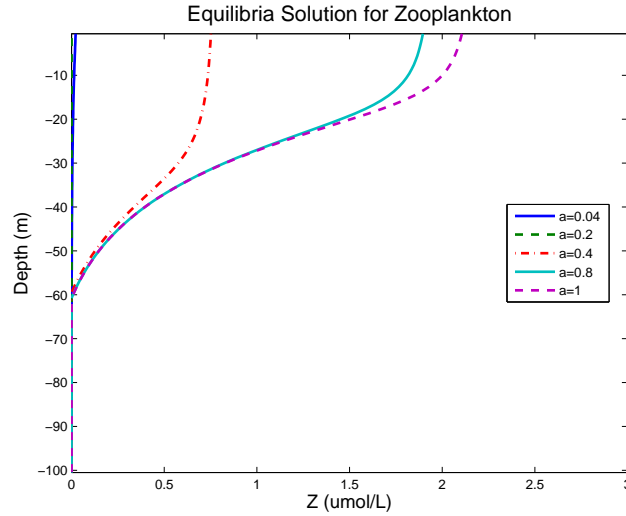
Figure 3-3: Equilibria solutions for Z for various values of assimilation rate a.

The third set of equilibria (Equations 3.4) is examined more closely by applying a dynamical systems approach to biological dynamics. We determine the relationship between values of ρ and s and whether the equilibria solution is physical (both real and positive) or not. Additionally, more than one physical solution is present for some values of ρ and s. Table 3.1 summarizes these results for zooplankton. From this table, we can predict the number of physical solutions, given the sign of ρ and s. There is always just one equilibrium for phytoplankton, for all ρ and s values, and the nutrient equilibrium can be extracted directly from the zooplankton equilibrium. We are interested in the variation with $\beta(z)$, as we expect a change in depth in nearly every realistic case. For a specific region with constant parameter values, it is possible to have a different number of solutions in different depth regions because of

43

the dependence on light. A change in the number of solutions commonly indicates a change in stability, so studying where these changes occur is a useful first step in stability analysis. We refer to a region (either in depth or another parameter) with the same stability properties as a "stability region." For instance, if the same number of solutions are predicted for $z = 0m$ to $z = -50m$, then this is one stability region.

From Figure 3-4, the number of different stability regions that exist in depth for a given value of N_T can be identified by determining the sign of ρ and s as depth increases. There is a transition from one region to another when either ρ or s changes sign. With information of ρ and s evaluated for one value of $\beta(z)$, we know everything about which regions are where for each value of N_T. It is important to have some initial information because we only know when ρ or s change sign, but not the sign to which they change. Also note that a limitation of this approach is if ρ or s have a minimum or maximum of zero, instead of changing signs at zero. This case has not been observed for any of the parameter sets tested, but should be verified when this approach is used.
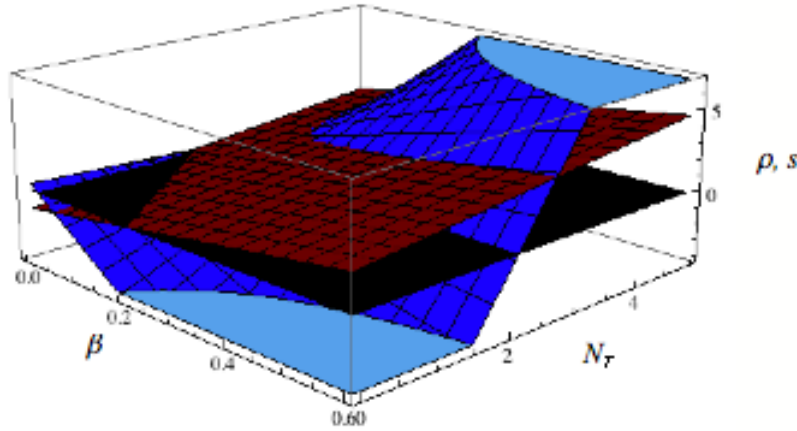
Figure 3-4: ρ and s for a range of N_T and β values.

Figure 3-4 shows ρ and s for a range of β and N_T values. For larger values of β and N_T, we see that both are positive (and $\rho^2 > s$) so there are two solutions in this region (from Table 3.1). For lower values of β and N_T, there are several different regions where one or neither ρ or s are positive. We can conclude that there are zero

Z **equilibrium**	$\rho > 0$ **when** $0 \leq \beta(z) \leq \beta_{c\rho}$	$\rho < 0$ **when** $\beta_{c\rho} \leq \beta(z) \leq u$
$s > 0$ **when** $0 \leq \beta(z) \leq \beta_{cs}$	2 solutions if $\rho^2 > s$ 1 solution if $\rho^2 < s$	No solutions
$s < 0$ **when** $\beta_{cs} \leq \beta \leq u$	1 solution (positive branch)	1 solution (positive branch)

Table 3.1: Number of zooplankton equilibrium points with ρ, s, and $\beta(z)$. β_{cs} is the depth where s changes sign and $\beta_{c\rho}$ is the depth where ρ changes sign.

or one solutions in this region. All four combinations listed in Table 3.1 are possible, as we can see in Figure 3-4.

While the three-dimensional plot is useful in providing a general idea of where region transitions are for given values of β and N_T, specific values of N_T should be examined to understand details of where region transitions occur. (This is done at the end of this section, with results in Appendix A.) We define critical stability values of depth as β_{cs} and $\beta_{c\rho}$ for a region transition (when s or ρ change sign, respectively). They are expressed in terms of the system parameters, including N_T:

$$
\begin{aligned}
\beta_{cs} &= d_p \frac{\left(k_s + N_T + \frac{\gamma}{\nu}\right)}{N_T + \frac{\gamma}{\nu}} \\
\beta_{c\rho} &= d_p + \frac{d_z}{a}\left(1 + \frac{\nu}{\gamma}\left(k_s + N_T\right)\right)
\end{aligned}
\tag{3.6}
$$

These critical stability depths are then used to find the range of N_T for which there are different stability regions with different limits. The critical values of N_T which define these ranges are:

$$
\begin{aligned}
N_{Tc\rho} &= -\left(\frac{\gamma}{\nu}\left(\frac{d_p a}{d_z} + 1\right) + k_s\right) \\
N_{Tcs} &= -N_{Tc\rho} - \frac{\gamma}{\nu}\frac{d_p a}{d_z}
\end{aligned}
\tag{3.7}
$$

Because γ is always negative, $N_{Tcs} > N_{Tc\rho}$. The three different ranges of N_T with unique stability properties are shown in Table 3.2.

Table 3.2 is constructed using the critical stability values of Equations 3.6 and 3.7, which indicate when a sign change of ρ or s occur, and Table 3.1, which determines

Z	Region 1 $0 \le \beta < \beta_{c1}$ $-\infty < z < z_{c1}$	Region 2 $\beta_{c1} < \beta < \beta_{c2}$ $z_{c1} < z < z_{c2}$	Region 3 $\beta_{c2} < \beta \le u$ $z_{c2} < z \le 0$
$0 < N_T < N_{Tc\rho}$	$s > 0$ $\rho < 0$ No solutions	$s < 0$ $\rho < 0$ One solution	$s < 0$ $\rho > 0$ One solution
$N_{Tc\rho} < N_T < N_{Tcs}$	$s < 0$ $\rho < 0$ One solution	$s < 0$ $\rho > 0$ One solution	$s < 0$ $\rho > 0$ One solution
$N_T > N_{Tcs}$	$s < 0$ $\rho > 0$ One solution	$s > 0$ $\rho > 0$ Two solutions	$s > 0$ $\rho > 0$ Two solutions

Table 3.2: Number of zooplankton equilibrium based on total biomass (N_T), depth, and the sign of ρ and s. β_{c1} and β_{c2} are chosen based on the values of $\beta_{c\rho}$ and β_{cs}. For instance, if $\beta_{c\rho} > \beta_{cs}$, then $\beta_{c1} = \beta_{cs}$ and $\beta_{c2} = \beta_{c\rho}$.

$N_{Tcs} = 2.31$	$\beta_{cs} = 0.016$	$\beta_{c\rho} = 0.002$
$N_{Tc\rho} = 2.13$	$\beta_{cs} = 0$	$\beta_{c\rho} = 0.036$

Table 3.3: Critical values for parameter values listed in Equation 3.5, also presented in Figure 3-5.

how many solutions of Z exist, given the sign of ρ and s. Table 3.2 assumes $\rho > 0$ and $s > 0$ for $N_T < N_{Tcs}$ for $\beta = 0$ as initial conditions. If this assumption is not true, a similar table can easily be constructed using the above approach. The critical values hold for any initial condition. These ideas are clarified with an example. For the parameter values listed in Equation 3.5 the corresponding critical values are presented in Table 3.3 and in Figures 3-5 and 3-6.

Figures 3-5 and 3-6 provide a new technique of examining the number of solutions for different regions of N_T. The values of β where solution properties change are as predicted in Equation 3.6. Figure 3-5 is shown in terms of β and Figure 3-6 in terms of z. Again, plotting the graph in terms of β allows us to describe the system more generally, as the depth decay scale h and uptake rate u are not specified and are left completely general.

Holding N_T constant at $N_T = 2, 2.2$, and 3 $\mu mol/L$ (values above, in between, and below the critical values that define the ranges of N_T) for the case shown in
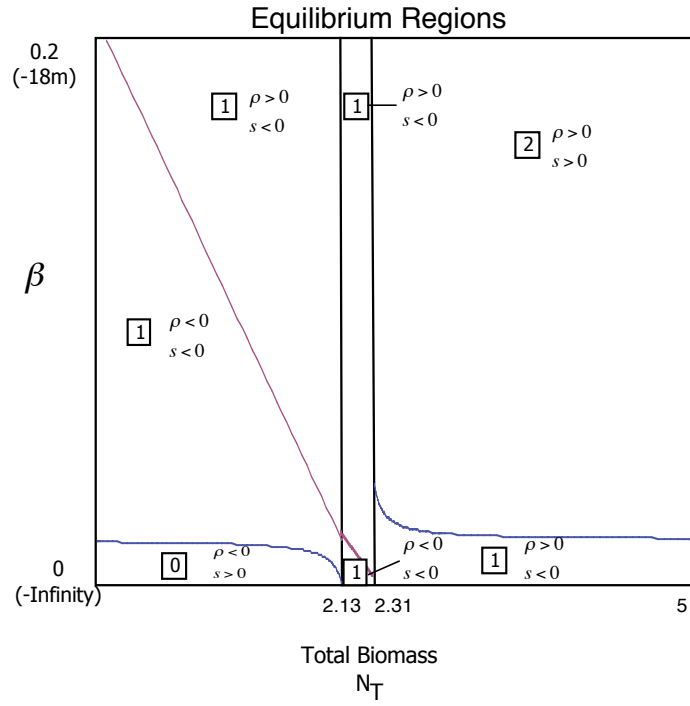
Figure 3-5: Stability regions in terms of $\beta(z)$ predicted by Equation 3.6 and 3.7 for parameters in Equation 3.5. Increasing values of β are closer to the sea surface. The boxed numbers indicate the number of equilibrium solutions for Z.
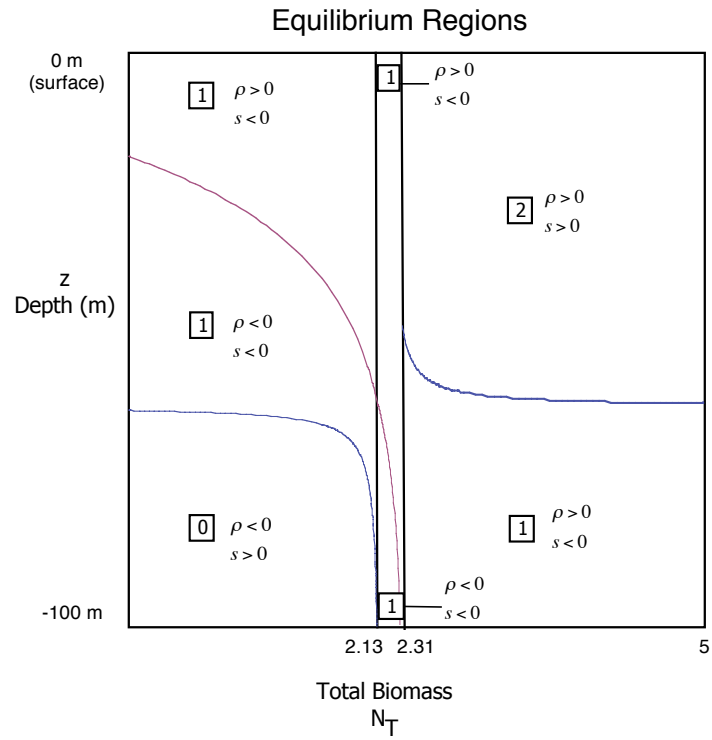
Figure 3-6: Stability regions in terms of z predicted by Equation 3.6 and 3.7 for parameters in Equation 3.5. The boxed numbers indicate the number of equilibrium solutions for Z.

Figure 3-5 are presented in Appendix A. The final figures of Appendix A show that the number of solutions for Z predicted using Table 3.1 are correct. The last figure also reveals that the positive root of Z never gives positive nutrient concentration (for those parameter values used).

Being able to identify the values of depth $\beta(z)$ and biomass N_T where solutions exist and defining the number of such equilibrium solutions is very powerful. Stability properties may change at the transitions across regions. These ranges are specified by the values of the equation parameters and bring us closer to identifying ranges of parameters for stable solutions.

3.2 Stability of the Linearized System

Using the information about equilibria discussed in Section 3.1, an analysis of the linearized equations (in the reference frame without physics) around the equilibria solutions reveals stability properties for the general solution regions. Equations 3.1 are linearized around the equilibria (P_0 and Z_0 from Equations 3.4, using the "negative" Z root) and the result is a system of two ordinary differential equations:

$$\begin{bmatrix} \frac{dP}{dt} \\ \frac{dZ}{dt} \end{bmatrix} \approx \begin{bmatrix} M_{PP} & M_{PZ} \\ M_{ZP} & M_{ZZ} \end{bmatrix} \begin{bmatrix} P_0 \\ Z_0 \end{bmatrix} \tag{3.8}$$

where M_{ij} is the linear coefficient of j for the i equation and is comprised entirely of system parameters. For a local stability study, we focus on the matrix that describes the first order behavior of the system (matrix $\mathbf{M}$). The eigenvalues of the Jacobian of Equation 3.8 indicates local stability: if the real part is positive, we expect unstable behavior and if the real parts of both eigenvalues are negative, the solutions are stable. If the real part of the eigenvalue is zero, an oscillatory solution results, assuming the imaginary part of the eigenvalue is non-zero. Equation 3.9 is the Jacobian of the linearized system, where P_0 and Z_0 are the equilibrium values.

$$
J = \begin{bmatrix} A_{11} & A_{12} \\ A_{21} & A_{22} \end{bmatrix}
$$

where

$$
A_{11} = -d_p - e^{-P_0\nu} g Z_0 + \frac{e^{\frac{z}{h}} u \left(k_s \left(N_T - 2P_0 - Z_0 \right) + \left(-N_T + P_0 + Z_0 \right)^2 \right)}{\left(k_s + N_T - P_0 - Z_0 \right)^2} \tag{3.9}
$$

$$
A_{12} = \frac{\left(-1 + e^{-P_0\nu} \right) g}{\nu} - \frac{e^{\frac{z}{h}} k_s P_0 u}{\left(k_s + N_T - P_0 - Z_0 \right)^2}
$$

$$
A_{21} = a e^{-P_0\nu} g Z_0
$$

$$
A_{22} = -d_z + \frac{a \left(1 - e^{-P_0\nu} \right) g}{\nu}
$$

The corresponding eigenvalues of the Jacobian can be expressed in closed form using the general expression for eigenvalues of a 2x2 matrix:

$$
\begin{aligned}
\sigma_1 &= \frac{1}{2} \left(A_{11} + A_{22} - \sqrt{A_{11}^2 + 4A_{12}A_{21} - 2A_{11}A_{22} + A_{22}^2} \right) \\
\sigma_2 &= \frac{1}{2} \left(A_{11} + A_{22} + \sqrt{A_{11}^2 + 4A_{12}A_{21} - 2A_{11}A_{22} + A_{22}^2} \right)
\end{aligned}
\tag{3.10}
$$

Although we can see that the eigenvalues of the Jacobian can easily be expressed in closed form from Equations 3.9 and 3.10, the result includes numerous terms. If some system parameters are known, the effect of the range of the unknown parameter values can be expressed analytically by taking the derivative of the eigenvalues with respect to the unknown parameter. Identifying where the real part of the eigenvalue is negative and positive gives defined ranges of stability and instability in terms of the unknown parameter.

Using the parameters from Equation 3.5, we assume here that all parameters but N_T are known and perform the stability analysis for total biomass. In Chapter 4, we initialize a two-dimensional simulation using a specified N_T, so it is important to know if a particular region (with a specific N_T value) would give a stable or unstable solution so as to anticipate the local behavior of the time-dependent solutions.
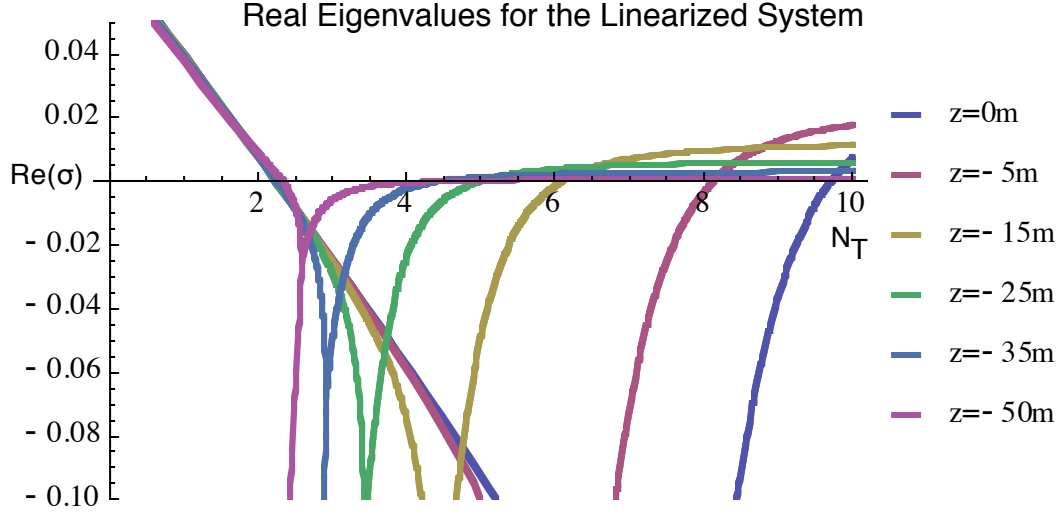
Figure 3-7: Real part of the eigenvalues for the Jacobian of the linearized system evaluated at the equilibrium with varying total biomass.

The real eigenvalues for Equations 3.8 (Figure 3-7) show regions of negative (indicating decay, therefore stable) and positive (indicating growth, therefore unstable) values. The range of N_T for non-positive real eigenvalues shrinks in depth, so the range of N_T for the system to be in a stable regime is defined by the lowest depth of interest or $z = -50m$ (the approximate limit for which NPZ equations were originally derived [20]). Another interesting property to note is shown in Figure 3-8 where there is a critical depth value for a disappearing bifurcation. This figure shows that this value for our given parameters is about $z = -62m$, as the bifurcation is seen for all values above $z = -61m$, but disappears for $z = -62m$.

Figure 3-9 confirms the stability of the region limited by $z = -50m$. The equilibrium solutions are stable for $N_T = 2.5, 3, 3.5, 4$ $\mu mol/L$ but not for $N_T = 2$ and 5 $\mu mol/L$, as predicted in Figure 3-7. It is interesting to note that the analysis of equilibrium points (Figures 3-5 and 3-6 and Table 3.1) reveals just one of the critical values, the lower bound of an acceptable range of N_T for stable equilibria ($N_T = 2.31$ $\mu mol/L$ for the example above), while looking at the real eigenvalues of the linearized system evaluated at the equilibria reveals a more restricted range with an upper and lower bound, dependent on the value of depth. While the analysis presented in Sec-
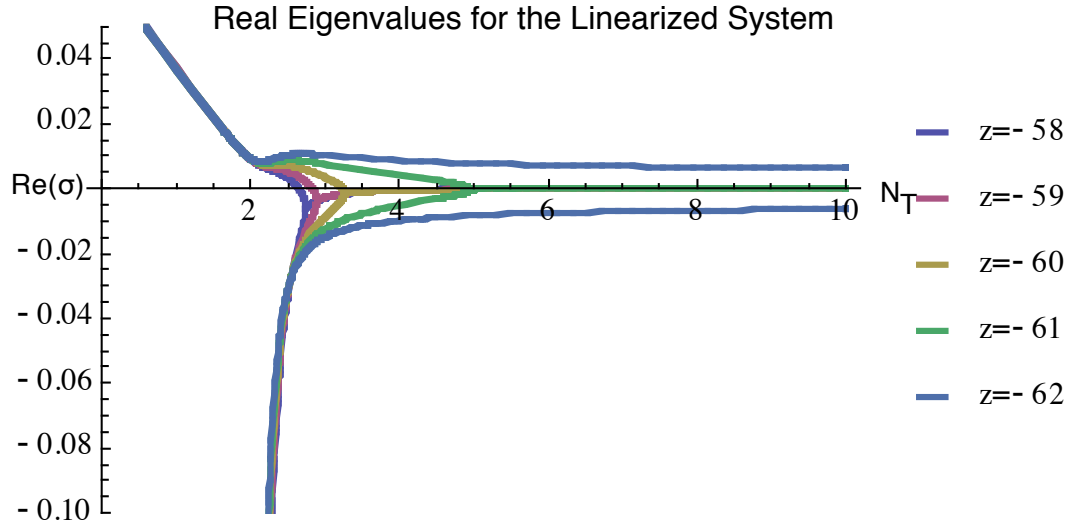
Figure 3-8: Real part of the eigenvalues for the Jacobian of the linearized system. A bifurcation vanishes as $z \to -62m$.
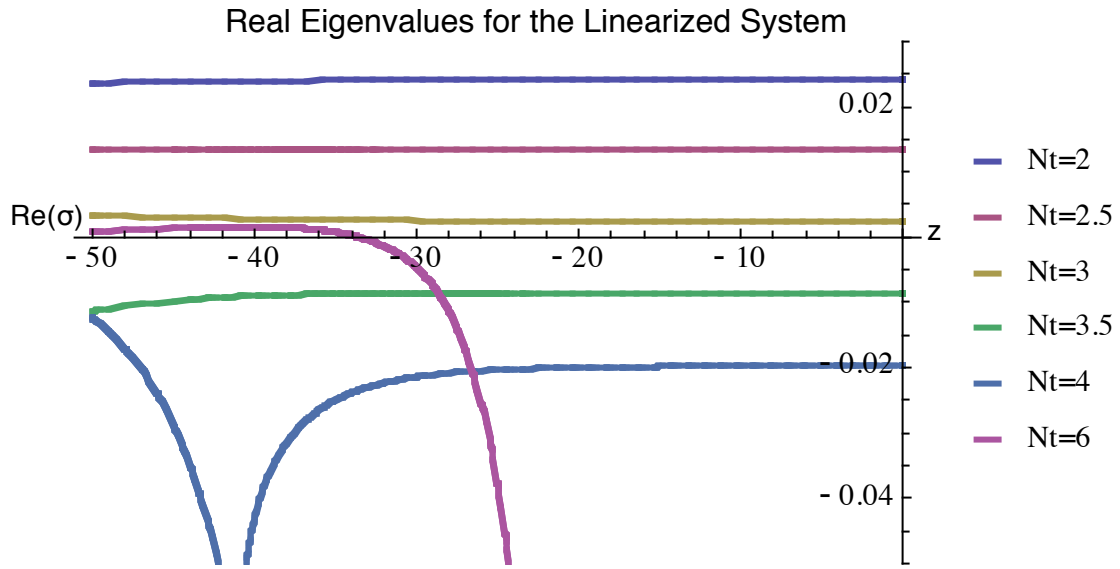
Figure 3-9: Real part of the eigenvalues for the Jacobian of the linearized system evaluated at the equilibrium with varying N_T.

tion 3.1 does provide useful information globally, it does not give us complete N_T ranges of local stability.

Figures 3-10 and 3-11 show identical analysis as presented for Figure 3-7 through Figure 3-9, but now the Jacobian is evaluated at the positive root of the Z equilibrium solution of Equations 3.4.
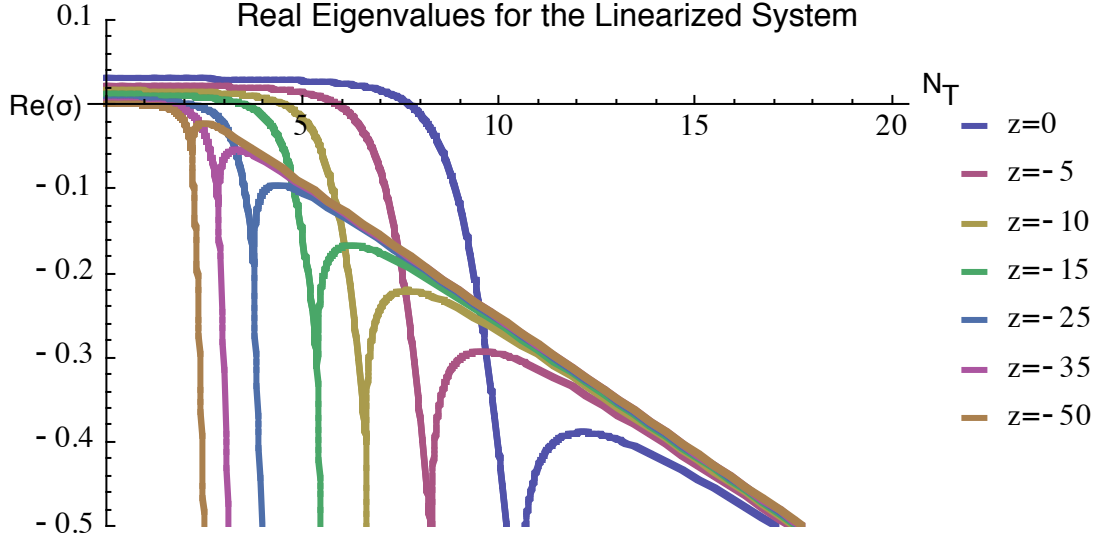
Figure 3-10: Real part of the eigenvalues for the Jacobian of the linearized system evaluated at the equilibrium (positive Z root) with varying depth.

Unlike the previous case, the growth rates for the positive root of Z are limited by $z = 0m$, not $z = -50m$. The critical lower bound N_T value is 7.7 $\mu mol/L$. Beyond this lower bound, there are positive growth rates. Figures 3-11 and 3-12 show that all $N_T < 7.7$ $\mu mol/L$ have positive growth rates at the surface ($z = 0m$).

Those critical values for N_T found in Section 3.2 do not reveal anything about the stability properties of the linearized equations around the positive Z equation because they described the transition of the negative Z root appearing or disappearing (see Table 3.1). We focus on the "negative" root because the positive root of the Z equilibrium is limited in producing real, positive values, while the negative Z root gives physical results ($Z > 0$) more often for our parameter set. The stability regions (in N_T) for both roots are summarized in Table 3.4.

Having a stable solution does not imply that it is a physical solution (real and
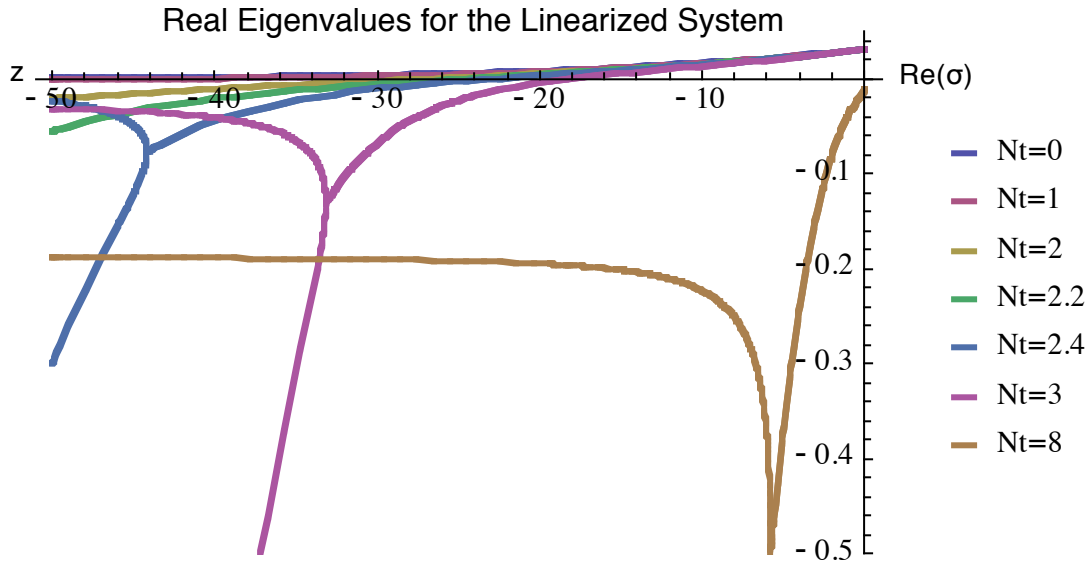
Figure 3-11: Real part of the eigenvalues for the Jacobian of the linearized system evaluated at the equilibrium (positive Z root) with varying total biomass.
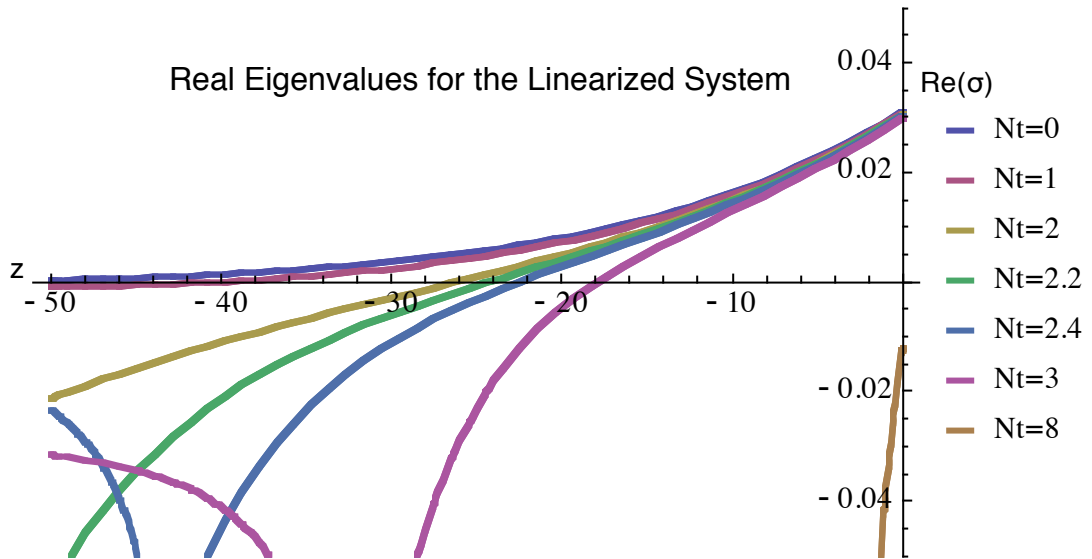
Figure 3-12: Real part of the eigenvalues for the Jacobian of the linearized system evaluated at the equilibrium (positive Z root) with varying total biomass.

Linearized Equations with:	Z^+ equil. pt.	Z^- equil. pt.
Stable if	$N_T > 7.7$	$2.31 < N_T < 4.44 \, for \, z_{MAX} = -50m$
Unstable if	$N_T < 7.7$	$N_T < 2.31 \, or \, N_T > 4.44 \, for \, z_{MAX} = -50m$

Table 3.4: Stability regions (in total biomass, limited by $z = 0$) for parameter values listed in Equation 3.5.

positive). In fact, the last graph of Appendix A shows that the positive root of the Z equilibrium never gives a positive N value. So, while the positive root of the Z equilibrium may give stable results, they are not physical. An example is presented in Figure 3-13. While both of these equilibrium solutions are within the stable regime of N_T and z, only the negative root is physical (positive for N, P, and Z).
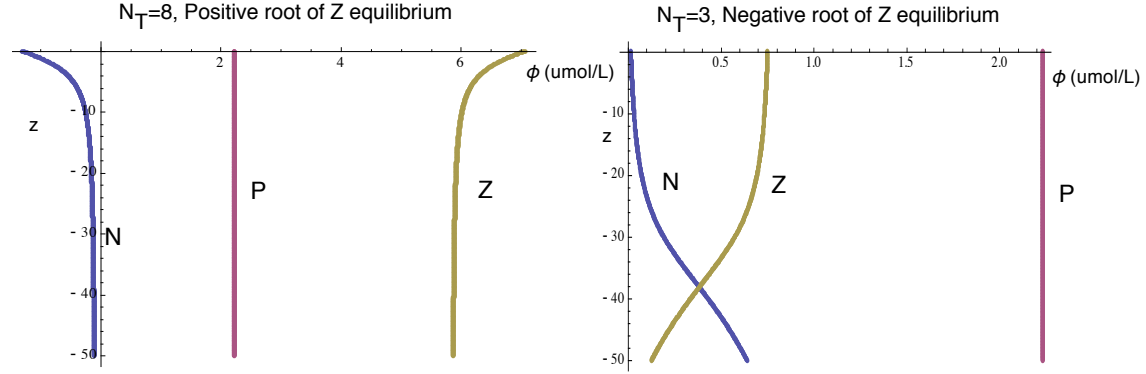
Figure 3-13: Stability does not imply a physical solution. Though $N_T = 8$ gives a stable solution, it is unrealistic, with negative nutrient values.

Closed form expressions for stability ranges of parameters can be derived for k_s, d_p and ν and the new above method we developed can be applied to analyze local stability. The parameters d_z, a and g do not give closed form solutions, but similar analysis can be performed with the aid of numerical "root finding" schemes. These expressions are shown in Table 3.5. The critical stability depths, β_{cs} and $\beta_{c\rho}$, are always in closed form.

The predictions of critical stability depths and stability regions in terms of N_T presented in this section are tested using phase portraits, which plot the evolution of Equations 3.1 in time. These results are represented in the phase space, P versus Z. The phase portraits allow us to verify our new predictions for equilibrium points and

Parameter (ϕ)	$\phi_{c\rho}$	ϕ_{cs}
N_T	$-\left(\frac{ad_p\gamma}{d_z\nu} + \frac{\gamma}{\nu} + ks\right)$	$-\left(\frac{\gamma}{\nu} + k_s\right)$
k_s	$-\left(\frac{ad_p\gamma}{d_z\nu} + \frac{\gamma}{\nu} + N_T\right)$	$-\left(\frac{\gamma}{\nu} + N_T\right)$
d_p	$-\frac{d_z}{a\gamma}\left(\gamma + k_s\nu + N_T\nu\right)$	–
ν	$-\frac{\gamma}{d_z}\frac{ad_p+d_z}{k_s+N_T}^*$	$-\left(\frac{\gamma}{k_s+N_T}\right)$
a	$-\frac{d_z}{d_p\gamma}\left(\gamma + k_s\nu + N_t\nu\right)^*$	–
d_z	$-\left(\frac{ad_p\gamma}{\gamma+k_s\nu+N_T\nu}\right)^*$	–

Table 3.5: Stability region limits, defined by parameters. Starred values must be solve numerically because those parameters are included in γ.

stability of those points.

3.2.1 Phase Portraits

We created phase portraits of P versus Z using the nonlinear coupled NPZ equations without advection or diffusion (Equations 3.1). Appendix B shows these phase portraits for $N_T = 2, 3, 5$, and 8 $\mu mol/L$. For the last three values, phase portraits are shown both for the full range of values as well as for a smaller range surrounding the analytical equilibrium point ($N_T = 2$ $\mu mol/L$ has an equilibrium point that is not physical and therefore is not shown). The x-axis is concentration of zooplankton Z while the y-axis is phytoplankton concentration P. The equilibrium points are listed for each depth level and N_T value. Only values under the line $P = N_T - Z$ are considered, as this defines the region where the solutions are physical (from the restriction $N_T = N + P + Z$). Based on the real part of the eigenvalue of the Jacobian for the linearized system, each equilibrium point is predicted to be *stable* (S, real eigenvalue is negative and there is decay) or *unstable* (U, real eigenvalues is positive and there is growth). These conclusions are summarized in Table 3.6 (from Figure 3-7).

Though the stability points are sometimes difficult to distinguish in the graphs of Appendix B, the location and stability are all accurately predicted by the analytical solutions. While phase portraits are very powerful, it is much more difficult to determine an equilibrium point without an analytical solution, especially in cases where

Stability	$z = 0m$	$z = -25m$	$z = -50m$
$N_T = 2 \ \mu mol/L$	U	U	U
$N_T = 3 \ \mu mol/L$	S	S	S
$N_T = 5 \ \mu mol/L$	S	U	U
$N_T = 8 \ \mu mol/L$	S	U	U

Table 3.6: Results of the phase portraits in Appendix B.

the attraction region is very narrow.

The analytic results presented in this chapter are verified by phase portrait analysis. These results provide insight into the stability and behavior of the dynamic system that would otherwise be impossible to obtain directly with a more complex model that only permits numerical analysis.

3.3 Applicability to the Dynamic Environment

While the results derived in previous sections are useful in describing the system, they are even more powerful if they indicate something about the dynamic environment. Using the numerical scheme discussed in Chapter 4, the system was evolved for 100,000 time steps (1,000 days) to simulate "steady state" and determine if the behavior predicted for the system without physics also held for the steady state case. An elliptical bathymetry was placed on the ocean floor to create vertical velocities, an important contribution to biological interaction. Initially, only advection is imposed, and then diffusion is added later. Waters below $z = -50m$ were initialized using Equation 3.2 and the top $50m$ was initialized with Equation 3.4 (using the "negative" Z root). Additional details about the implementation of the numerical simulation are found in Chapter 4.

The simulation initialized with $N_T = 3 \ \mu mol/L$ gave a stable steady state result, as shown in Figure 3-14. This is the expected result because the upper bound for stability is $N_T = 4.44 \ \mu mol/L$ for the domain without physics. The entire water column was studied for stability, but Figure 3-15(a) (and all other figures showing profiles) focuses on the profiles in the upper $50m$ because this is the region initialized

with the equilibrium solution of interest. Figure 3-15(a) shows the profiles for each node in the horizontal dimension in the domain at steady state for all three state variables. From these profiles, we see no evidence of unstable behavior. Figure 3-15(b) would show cross-hatching at any depth where an unstable solution is predicted for the domain without physics, but the euphotic zone is entirely stable in this case. Lastly, Figure 3-15 presents the real eigenvalues for $N_T = 3 \ \mu mol/L$ in the domain without physics. In this case, they are all negative.

Figure 3-14: Steady state solution (for advection only) for nutrient, phytoplankton, and zooplankton for initial biomass of $N_T = 3 \ \mu mol/L$.
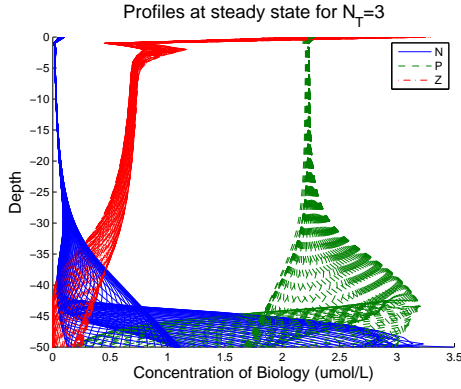
(a) Profiles in depth for the steady state solution initialized with $N_T = 3$ $\mu mol/L$. This solution is stable.
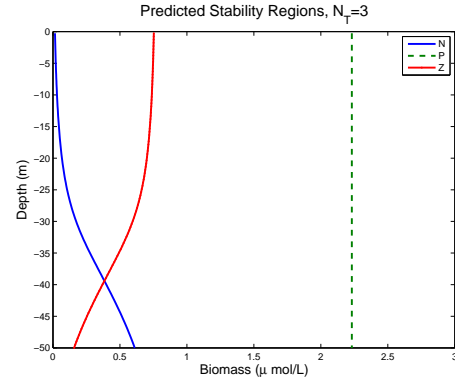
(b) The entire euphotic zone is predicted to be stable from our analysis in the domain without physics.
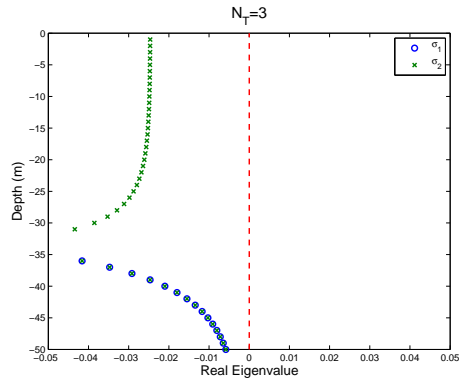
(c) Real eigenvalues in depth for $N_T = 3$ $\mu mol/L$. No positive eigenvalues indicate that the solution is stable in the domain without physics.

Figure 3-15: Comparison of stability in domain with and without physics for $N_T = 3$ $\mu mol/L$.

$N_T = 5 \ \mu mol/L$, just outside of the predicted stability region, also has a steady state result (Figure 3-16), even though the lower portion of the euphotic zone is predicted to be unstable (Figure 3-17(b)) in the domain without physics. Figure 3-17(c) shows that while the real eigenvalues are positive for the lower euphotic zone, these values are very close to zero. Therefore, adding physics (advection only) to the system seems to have a stabilizing effect. The profiles for the steady state solution are presented in Figure 3-17(a).

Figure 3-16: Steady state solution (for advection only) for nutrient, phytoplankton, and zooplankton for initial biomass of $N_T = 5 \ \mu mol/L$.
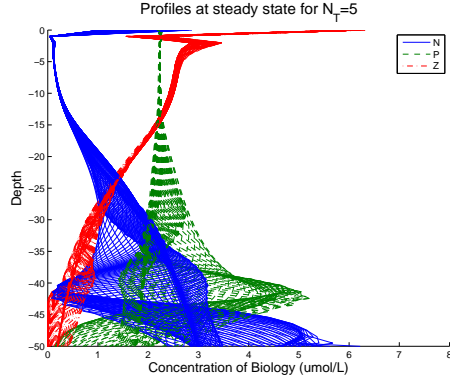
(a) Profiles in depth for the steady state solution initialized with $N_T = 5 \ \mu mol/L$. Again, the solution is stable.
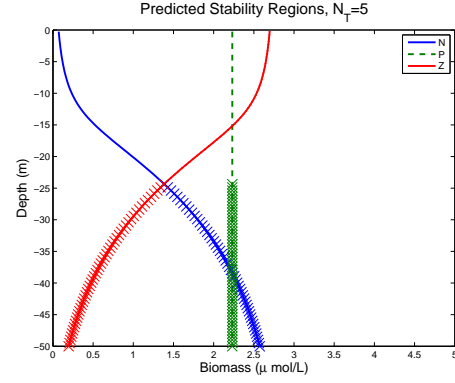
(b) Predicted stable and unstable regimes of the equilibrium solution. The cross-hatched portion is where we expect an unstable solution.
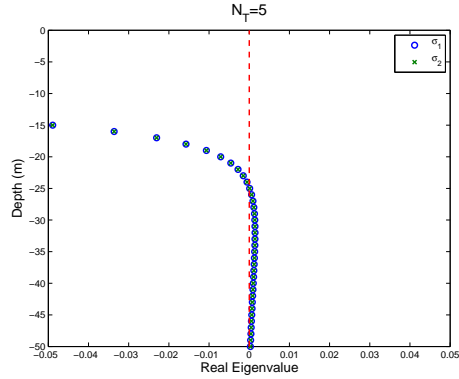
(c) Real eigenvalues in depth for $N_T = 5$ $\mu mol/L$. While eigenvalues for the lower euphotic zone are positive, they are very near zero. We do not see unstable behavior because the physics stabilize the solution.

Figure 3-17: Comparison of stability in domain with and without physics for $N_T = 5$ $\mu mol/L$.

Domains with more total biomass in the system have higher real positive eigen-values (Figure 3-19(c)), so their growth rate becomes larger as N_T grows. A steady state solution was not found for $N_T = 12 \ \mu mol/L$ (Figure 3-18) because values near the surface were oscillatory. The profiles for the state at 100,000 time steps, or 1,000 days, (Figure 3-19(a)) show very noisy values of biology near the surface, due to the unstable nature of this case. Note the physical and biological time scales are com-parable: it takes 25 days for the mean flow to advect over the bathymetry, while the time scale for biological reaction is about 30 days. As Figure 3-19(b) shows, the entire euphotic zone is predicted to be unstable in the domain without physics, with real eigenvalues much larger than in the previous case, as shown in Figure 3-19(c). Therefore, while rapid growth does not occur for large N_T values, solutions are likely unphysical and our stability analysis in the domain without physics gives us a conser-vative estimate of appropriate values of total biomass to use for the system to remain stable. While regions with very small real eigenvalues stabilized when advection was added, larger positive real eigenvalues did not. While it is possible for the biology to become unstable, at least for some short period of time, knowing these limitations by examining the parameters in the domain without physics is powerful. When physics are added, it can become challenging to distinguish which effects are due to biological reactions and which are due to the interaction of physics and biology.

We expect diffusion to have a stabilizing effect. Performing an identical simulation with $N_T = 12 \ \mu mol/L$, but now including a diffusion constant of $\kappa = 0.1$ in the $x-$ and $z-$direction, we obtain Figure 3-20. Comparing the profiles of this case (Figure 3-21) to the case without diffusion (Figure 3-19(a)) reveals that the oscillations have subsided because of the diffusion introduced in the system and a steady state is attainable (Figure 3-20).

3.4   Discussion

Steady equilibria for an NPZ model were found and used to determine relationships between critical stability depth, biomass, and the number of positive, real solutions
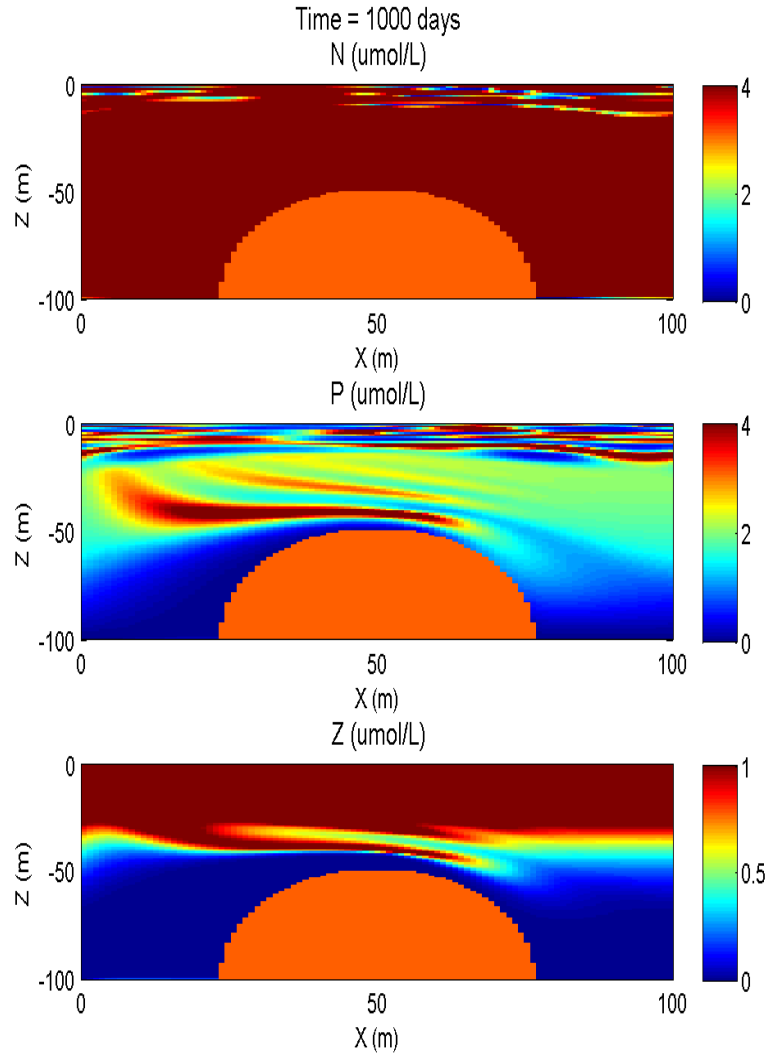
Figure 3-18: Solution (for advection only) for nutrient, phytoplankton, and zooplankton for initial biomass of $N_T = 12 \ \mu mol/L$.
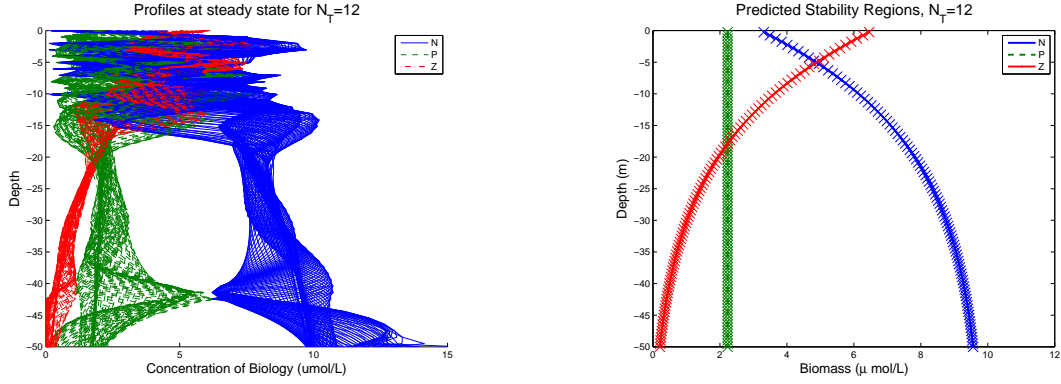
(a) Profiles in depth for the solution initialized with $N_T = 12$ after 100,000 time steps (1,000 days). The oscillatory behavior about $-20m$ indicates unstable behavior. No steady state solution was found for this case.

(b) The entire euphotic zone was predicted to be unstable for $N_T = 12$ $\mu mol/L$.
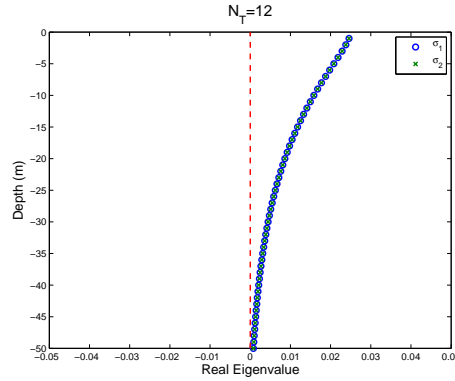
(c) Real eigenvalues in depth for $N_T = 12$ $\mu mol/L$. The magnitude of the real eigenvalues decay in depth. Comparing this figure to Figure 3-19(a), it seems that adding physics to a domain can stabilize real eigenvalue of about 0.01 and below, but any value greater than this led to unstable behavior.

Figure 3-19: Comparison of stability in domain with and without physics for $N_T = 12$ $\mu mol/L$.
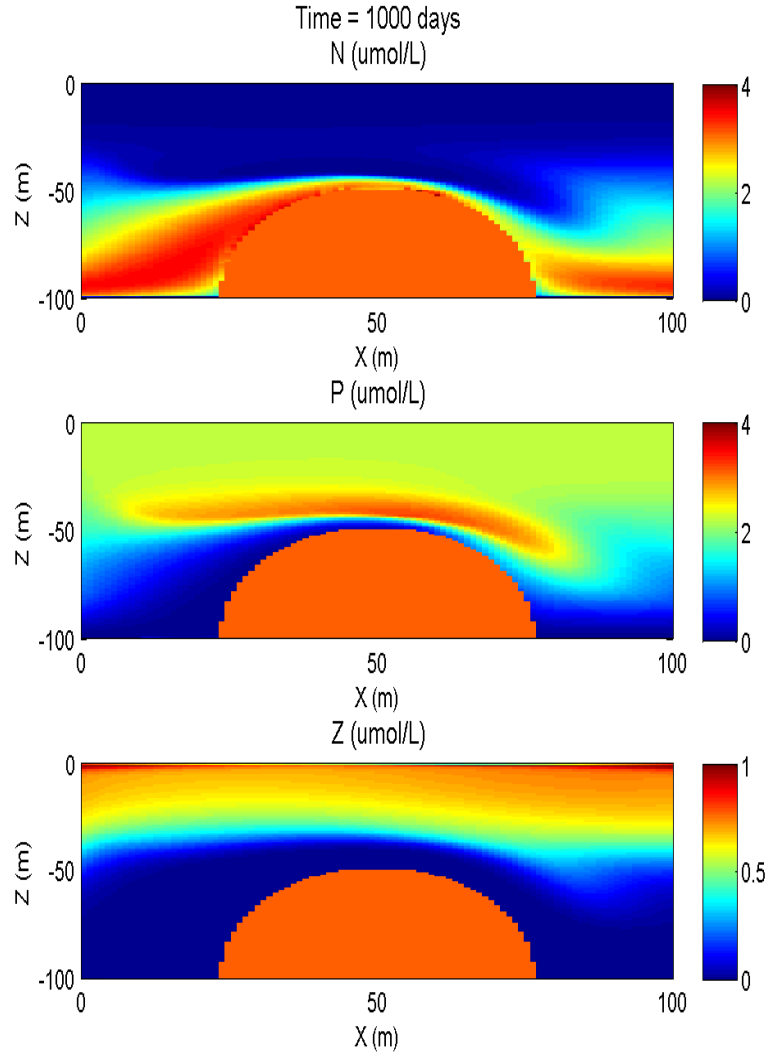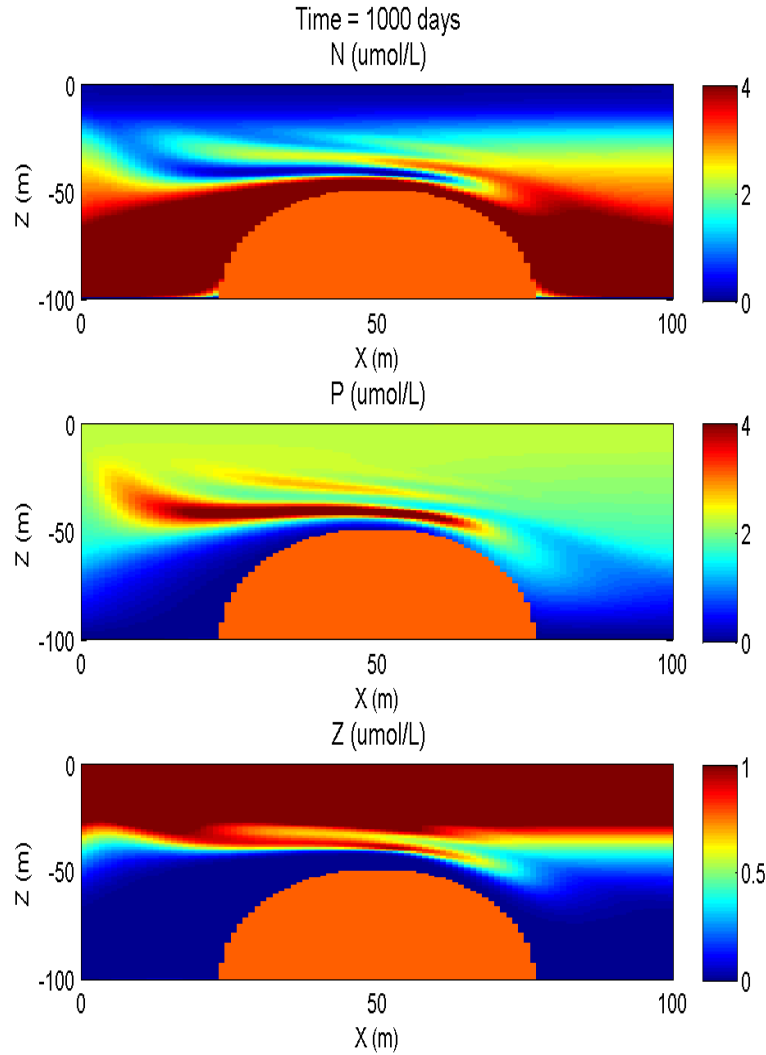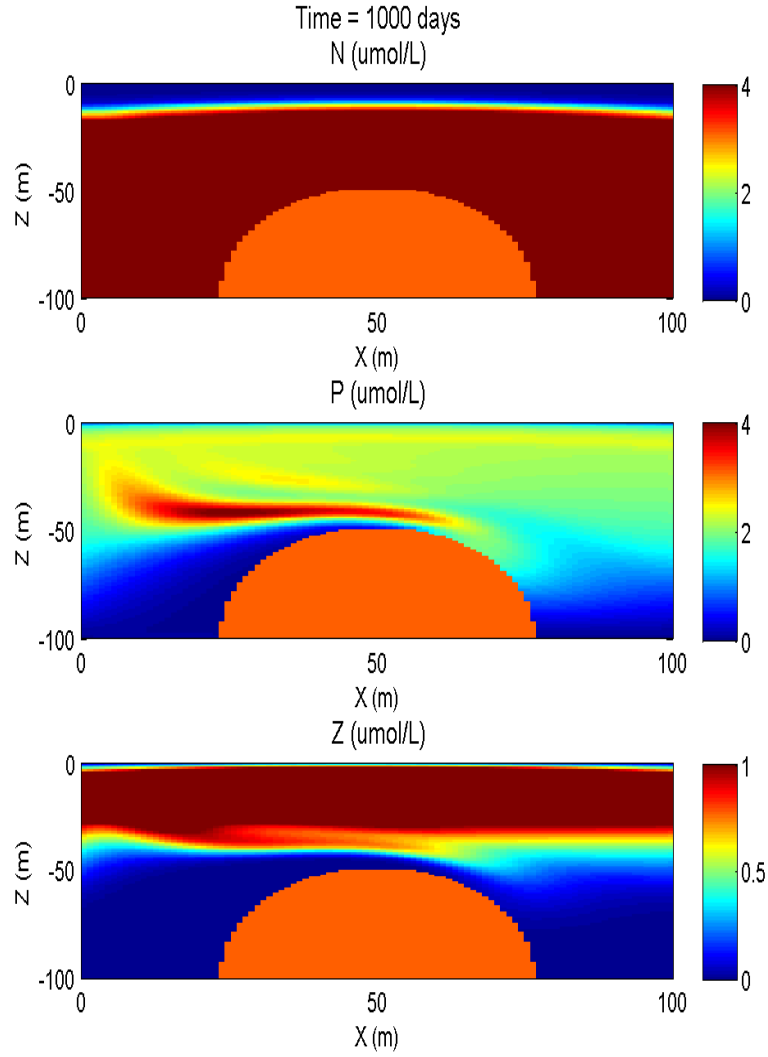
Figure 3-20: Steady state solution (for advection and diffusion) for nutrient, phytoplankton, and zooplankton for initial biomass of $N_T = 12 \ \mu mol/L$. Diffusion acts to stabilize the previously unstable solution.
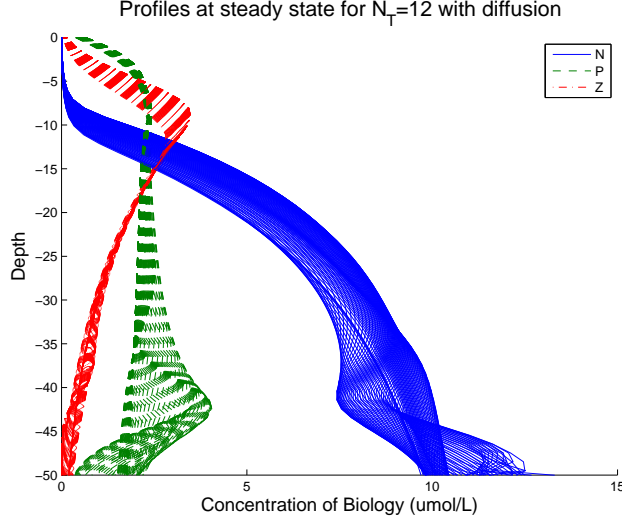
Figure 3-21: Profiles in depth for the steady state solution initialized with $N_T = 12$ $\mu mol/L$ including diffusion. Unlike the previous case without diffusion, a steady state was obtainable. Diffusion acts to stabilize the solution.

for the zooplankton concentration equilibrium. Expressing the Z equilibrium in terms of two other parameters, ρ and s, at a known depth is sufficient to characterize the number of equilibrium solutions in the entire water column, when the expressions for critical stability depths and biomass values are used. These expressions are general in terms of the system parameters. Conditions on the number of solutions were summarized in Table 3.1. We concluded that with one set of initial information (the sign of ρ and s at a known depth) was sufficient to characterize the number of solutions for the Z equilibria for the whole space. With this information, similar conclusions about the N equilibria are known.

Identifying these equilibrium regions indicated possible changes of local stability, which was further investigated by examining the linearized version of Equations 3.8. By taking the eigenvalues of the Jacobian, evaluated at the equilibria (Equation 3.4), local stability properties of depths and values of biomass were identified based on the sign of the real part of the eigenvalues. Another interesting feature arose as a critical stability depth was found where a bifurcation disappeared. This approach can easily be applied to any of the parameters and expressions listed in Table 3.5.

Phase portraits were created to verify the analytical results using numerical meth-

ods and were presented in Appendix B. Though some phase portraits match the analytical results better than others, all appear to match our analytical predictions. These results in the reference frame without physics were then tested in a dynamic physically-forced environment. A numerical simulation was evolved for many time steps to reach "steady state" if it existed. Three initial conditions, which are predicted to be (i) stable, (ii) near stability, and (iii) further from stability, were implemented and tested. The numerical simulations showed that initial conditions predicted to be stable or near stability give a stable steady state. Initial conditions in the unstable regime maintained magnitudes of biomass on the order of the initialized values, but steady state solutions were not found because the solution in the top $15m$ was oscillatory. Lastly, diffusion was added to the unstable case and we showed that a steady state was now attainable, therefore diffusion has a stabilizing effect.

The new methods for both global and local stability presented here are most useful when some parameters of a system are known and sensitivity and stability properties of the remaining parameters are needed. Depth should always be compared along with the parameters of interest, because it will always vary and identifying a critical depth where equations change dynamical properties is important.

Chapter 4

Two-Dimensional Idealized Numerical Simulation

A two-dimensional idealized numerical model, designed to investigate the influence of physical processes on biology, as well as the intrinsic biological dynamics, requires an appropriate numerical scheme that accurately solves the partial differential equations (PDEs) describing the system. Specifically, our goal is to discretize Equations 2.3 using a scheme capable of modeling a wide range of biological-physical processes, including cases dominated by advection. We first describe the general setup of the simulation, with details on boundary conditions and initial conditions. This includes numerical implementation using masking on the Arakawa C-grid and the Operator Splitting Method (OSM). Next, we compare the central difference, donor-cell, hybrid and weighted essentially non-oscillatory (WENO) numerical schemes used to discretize a simplified version of Equations 2.3. While our numerical simulation is designed to model both physics and biology, the physics limit which schemes can be used because some physical processes are more challenging to accurately represent with numerical methods. For example, spurious oscillations, which appear similar to the well-known Gibbs phenomenon but arise differently, commonly occur in the advection-dominant case when discontinuities in the velocity or tracer field are present [51]. Therefore, to isolate and study the manifestation of oscillations in the advection-dominant case, we test all schemes in a one-dimensional domain with advection only.

Additionally, we study numerical diffusion, which is particularly important when modeling biological processes because an accurate solution cannot be found if the reaction and diffusion terms are affected by numerical errors.

In this chapter, we focus on determining the most appropriate scheme to minimize spurious oscillations with low computational costs and low numerical diffusion by comparing several numerical schemes. The numerical diffusion and oscillatory nature of the schemes are studied. Numerical diffusion is diffusion introduced from discretizing the differential equations which causes the system to behave differently than the intended physical system. A comparison of several schemes reveals that the WENO scheme is the most suitable for the idealized simulations. The resulting simulation is verified against a simulation using Discontinuous Galerkin on an unstructured grid with identical conditions.

4.1 Problem Setup

Equations 2.3 are discretized in a two-dimensional vertical "slice" of the ocean strait (where x is the horizontal dimension and z is the vertical dimension). Any smooth bathymetry can be implemented. By assuming a two-dimensional inviscid, incompressible field, we can obtain a velocity field by solving the potential flow for any particular bathymetry. Because we ignore viscosity, we do not expect the solution near the sea bottom to be realistic, as there will be no boundary layer. Solving potential flow ensures that the flow satisfies continuity and assumes no flow may exit the sea surface or sea bottom. Code to solve for potential flow was developed by Ueckermann [58]. Once the numerical simulation is verified for a potential velocity field, other realistic flow fields can be used. For instance, taking a representative averaged flow through a strait generated from the primitive equations using MSEAS can be implemented to obtain a more realistic simulation.

4.1.1 Operator Splitting Method

The Operator Splitting Method (OSM) allows us to decouple problems and solve the equations in a single dimension. OSM, also known as time splitting or the method of fractional steps, is used to solve partial differential equations for initial value problems, usually in multidimensions [46]. If an initial boundary value problem can be expressed as a linear sum of operators (the operators themselves are not restricted to be linear), the original PDE can be split into terms based on these operators. The operators are applied to ϕ (the tracer, or in our case, biological concentration of a state variable) additively, yet this does not restrict the PDE itself to be linear [61]. For Equation 2.3, the advection and diffusion terms are discretized and solved in one direction (x) only, with the resulting solution of this step serving as the initial condition for the terms in the alternate direction (z). This process is repeated for each time step. OSM significantly reduces the computational cost by enabling us to solve the PDE in small time steps in a single direction only [46], allowing us to use banded algorithms. The OSM is limited in that it is most useful if the boundaries can be represented as a simple geometry, a restraint already present due to using a structured grid. Only boundaries that can be expressed as strictly perpendicular to one of the two axes (x and z) can be represented exactly.

4.1.2 Boundary and Initial Conditions

Boundary conditions are selected to be periodic in the x-direction, so that all biology leaving the system on one side enters the system on the other. For the sea surface boundary, a Neumann no flux boundary condition is imposed. Additionally, a Neumann boundary condition is implemented on the bathymetry. Therefore, because we have no flux conditions at the top and bottom boundaries and periodic boundaries on the sides, no biology leaves or enters the system. These boundary conditions create a conservative system: the initial total biomass N_T will remain constant for all time.

Initial conditions are the steady equilibria of the NPZ equations without flow, Equations 3.4. These equilibria are discussed in Chapter 3 and shown in Figure 4-1.
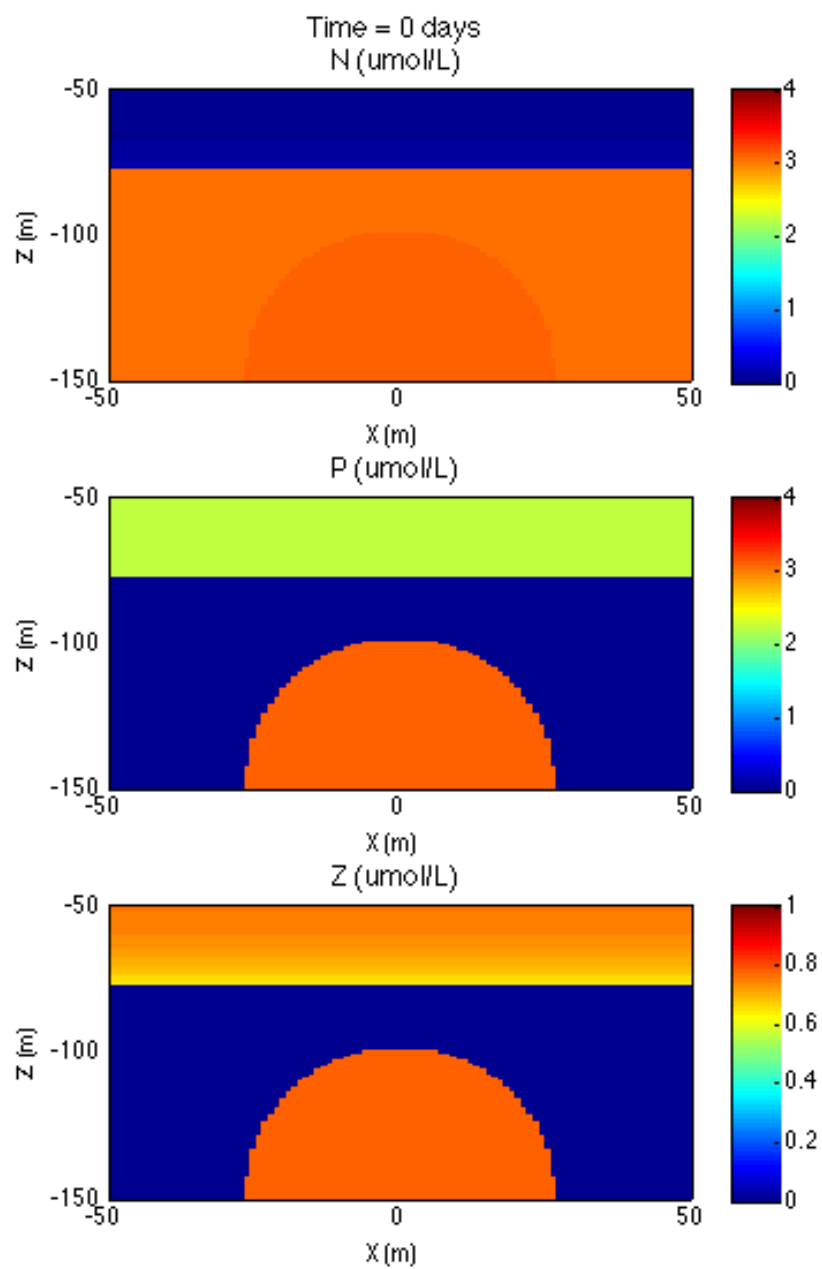
Figure 4-1: Initial conditions for nutrients, phytoplankton, and zooplankton.

4.1.3   Bathymetry, Masking, and the C-grid

An Arakawa C-grid is a staggered grid that simplifies enforcement of the continuity of mass by specifying separate node locations for the horizontal velocity, the vertical velocity, and the concentration a of biological state variable (the *tracer*) [4]. In this chapter, *tracer* and *concentration of biological state variable* will be used interchangeably. Space between nodes is constant in the grid, as shown in Figure 4-2. For this setup, there are I nodes in the horizontal direction and J nodes vertically. Node numbering begins at the top right corner and is separate for each type of node (vertical velocity, horizontal velocity, and the tracer), so that there are IxJ nodes of each type. $\phi_{i,j}$ refers to the tracer node that is ith from the left, jth from the top.

Using a C-grid allows boundary conditions to be implemented easily by applying a masking technique. First, three masks are constructed by identifying which tracer nodes lie under the bathymetry. For the C-grid, each mask is a IxJ matrix of ones and zeros. These masks are later applied to the gradient and divergence operators of the partial differential equation to enforce boundary conditions.

The three masks created "mask" all nodes under the bathymetry and any node neighboring those masked tracer nodes [37]. These masks are constructed as follows: the first mask corresponds to the tracer nodes and is called the tracer mask (M_T). Zeros are placed at any tracer node under the bathymetry, while the remaining nodes are given a value of one. For Figure 4-2, the six circular nodes behind the striped area are masked (assigned a value of zero) and all other circular nodes are one, as shown in Figure 4-3. To construct the horizontal velocity mask (M_H), M_T is shifted in the positive x-direction one node and multiplied by itself, so that the result is an IxJ matrix with the nodes surrounding the masked tracer nodes in the horizontal direction assigned zeros and all other entries assigned ones. Again using the elliptical bathymetry from Figure 4-2, nine square nodes are given zeros. All horizontal nodes neighboring "masked" tracer nodes are now masked. Similarly, to create the vertical velocity mask (M_V), M_T is shifted down and multiplied by itself. The vertical velocity mask does not differ from the tracer mask (in this case) because of how the nodes
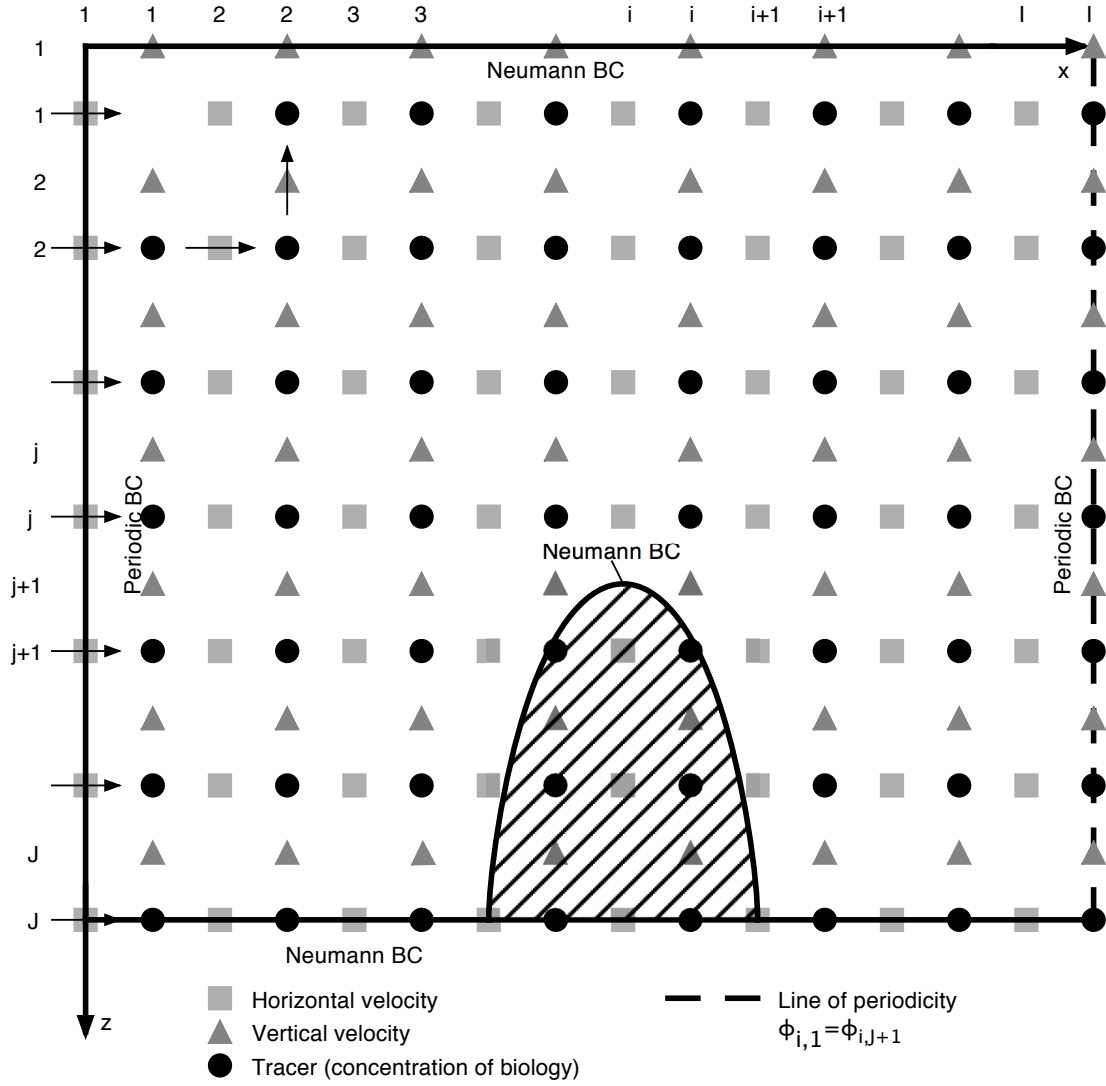
Figure 4-2: Arakawa C-grid in the idealized simulation domain with periodic boundary conditions in x and Neumann boundary conditions on the ocean bottom and air-sea interface. Tracer, horizontal velocity, and vertical velocity nodes are distinguished by circles, squares, and triangles, respectively. The area under the striped half-ellipse is bathymetry.

are numbered and the Neumann boundary conditions on the top and bottom. Figure 4-3 illustrates the end result of masking, with all masked nodes marked with an X, assuming the setup and elliptical bathymetry of the left frame of Figure 4-3.
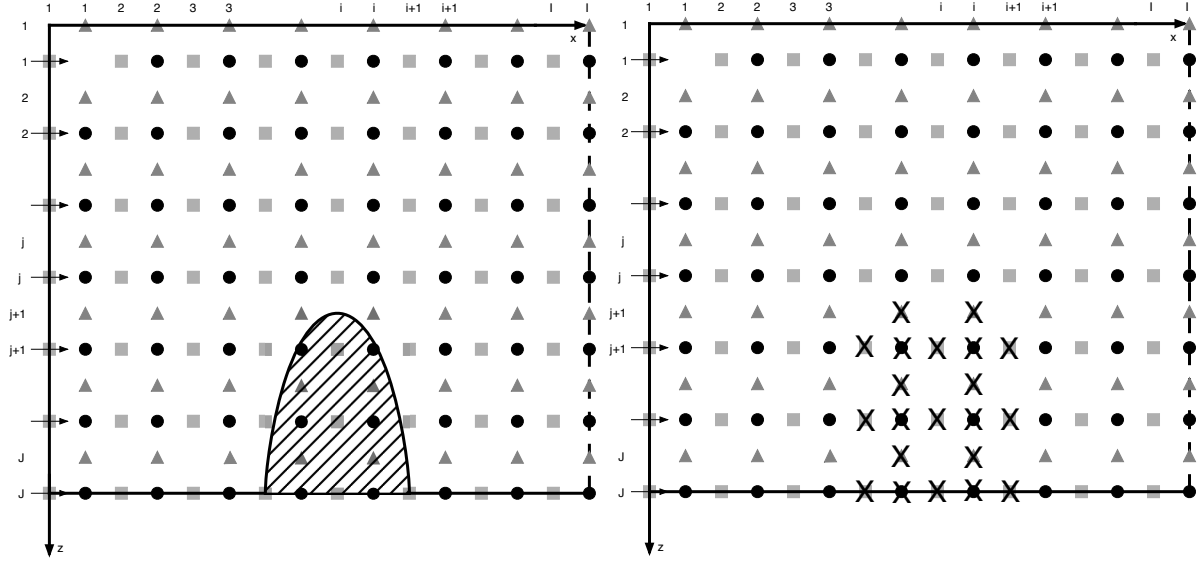
Figure 4-3: Placement of Xs in the figure on the right correspond to zeroes in the mask matrices. A one is placed in the matrix for any node without an X for the bathymetry shown on the left.

The divergence operator ($\nabla\cdot$) of the variable in a differential equation maps from a velocity node to a tracer node and is imposed by Hadamard (element-wise) multiplication of the velocity mask. In other words, the operation is discretized on the velocity nodes and the solution is placed on tracer nodes. A gradient operator (∇) maps from a tracer node to a velocity node and is implemented by a Hadamard multiplication of the tracer mask. The advective flux term of Equation 2.3 is simply the divergence of velocity multiplied by the tracer, while the diffusive flux term is the proportional to the divergence of the gradient of velocity. Therefore, the boundary conditions for the advection terms are applied by Hadamard multiplying the discretized derivative by the velocity mask, while the boundary conditions for the diffusion terms are implemented in two steps: first, by performing a Hadamard multiplication of the tracer mask and the first discretization step, and then multiplying the second discretization

75

step by either the horizontal or vertical velocity mask (depending on the dimension discretized). These operations set the advective and diffusive fluxes to zero at the boundaries. A detailed description of masking using matrix operators is available in Appendix B of [37]. For example, in one dimension for node i one obtains (using an average of tracer values at the velocity nodes and the central difference scheme):

$$\frac{\partial(u\phi)}{\partial x}\bigg|_i^{k+1} = \frac{\phi_{i+1}^{k+1}u_{i+1}^{k+1}M_H(i+1) + \phi_i^{k+1}(u_{i+1}^{k+1}M_H(i+1) - u_i^{k+1}M_H(i)) - \phi_{i-1}^{k+1}u_i^{k+1}M_H(i)}{2\Delta x}$$

$$\kappa\frac{\partial^2\phi}{\partial x^2}\bigg|_i^{k+1} = \kappa\frac{(\phi_{i+1}^{k+1} - \phi_i^{k+1})M_T(i+1) - (\phi_i^{k+1} - \phi_{i-1}^{k+1})M_T(i)}{(\Delta x)^2}M_H(i)$$

$$(4.1)$$

where ϕ_i is the tracer (on a tracer node), u_i is the velocity (on a velocity node), $M(i)$ is the ith element of the appropriate mask, M_T, M_H, or M_V, and $k+1$ is the next time step $(t + dt)$. The first equation is for advection and the second for diffusion. Applying the masks ensures that the operation only occurs if the node is not masked. Because we use OSM, we will apply the masks in one dimension for our idealized simulation, as in Equations 4.1.
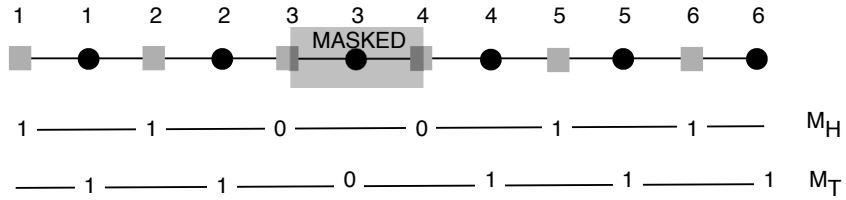
Figure 4-4: A one-dimensional view of masking for the example shown in Equation 4.2. Because we use OSM, this example is representative of our implemented scheme. The velocity mask is shown on the second line and the tracer mask is on the third line.

For the one-dimensional example shown in Figure 4-4, if we want to find $\frac{\partial\phi}{\partial t}\big|_2^{k+1}$ (ignoring diffusion, so that the change in ϕ is determined by the advection derivative at $i = 2$) we see, using Equation 4.1:

$$\left.\frac{\partial \phi}{\partial t}\right|_2^{k+1} = -\left.\frac{\partial (u\phi)}{\partial x}\right|_2^{k+1} = -\left(\frac{\phi_3^{k+1} u_3^{k+1} + \phi_2^{k+1}(u_3^{k+1} - u_2^{k+1}) - \phi_1^{k+1} u_2^{k+1}}{2\Delta x} M_H(2)\right)$$

with $M_H(2) = 1$ and $u_3^{k+1} = \phi_3^{k+1} = 0$ so that

$$\left.\frac{\partial \phi}{\partial t}\right|_2^{k+1} = u_2^{k+1}\left(\frac{\phi_2^{k+1} + \phi_1^{k+1}}{2\Delta x}\right)$$

$$(4.2)$$

We know that the tracer (ϕ) is always non-negative (because our tracer is concentration of biology) and that velocity (u) can be either positive or negative. Therefore, when the velocity node to the right of a tracer node is masked, the change of ϕ in time increases (decreases) with the magnitude of the positive (negative) velocity times the average concentration of biology at that velocity node, as expected.

4.2   Comparison of Numerical Schemes

With the problem setup complete, we compare numerical schemes by testing each in both the two-dimensional domain just described and a one-dimensional domain. The two-dimensional test cases reveals an overall view of features in the domain and the one-dimensional case allows us to isolate and more clearly understand the specifics of each scheme. Any features seen in the solution should be from the evolution of the equations, not an artifact of the numerics. Spurious oscillations are common near discontinuities in the advection-dominant case, so all test cases focus on how well the schemes represent advection only. Therefore, there is no diffusion or interaction between biology in any of the figures in this section. We are focused on representing the following equation, which is a simplified version of Equations 2.3 without diffusion or biological interaction:

$$\frac{\partial \phi}{\partial t} = -\frac{\partial (u\phi)}{\partial x} - \frac{\partial (w\phi)}{\partial z} \qquad (4.3)$$

We have already discussed stability of the biological terms in Chapter 3 and it is well known that adding diffusion stabilizes a system, so the best scheme to represent

Equations 4.3 will also be the best scheme to represent Equations 2.3 (our NPZ equations with advection, diffusion and biological reaction terms). In the remainder of this chapter, we show that the WENO scheme outperforms the central difference, donor-cell scheme and hybrid schemes in preserving the behavior and physics of the system. For each of the schemes discussed, we first examine the two-dimensional case, then a one-dimensional case to test the scheme in a "worst-case" scenario, and lastly we compare the cost efficiency of the schemes that accurately represent the modeled dynamics.

4.2.1 One-dimensional and Two-dimensional Test Cases

To compare numerical schemes, a one-dimensional test case was created. By masking a single node, the boundary conditions and masking of the more general case are tested. An initial Gaussian distribution is advected in the positive x direction and encounters a "blocked" node at one-third the domain length from the leftmost boundary ($x = -17$ in Figure 4-5). The boundary condition in x is periodic and 200 nodes are used to represent the domain. This test case uses a one-dimensional version of Equation 4.3 and the initial setup is shown in Figure 4-5.

Because this test case is one-dimensional with periodic boundary conditions and a blocked node, all of the tracer concentration initialized in the system should accumulate against the blocked node. This is one of the most challenging cases to model numerically because the tracer values at neighboring nodes are very different, which, for many schemes, leads to spurious oscillations at these discontinuities.

The two-dimensional test case uses the setup described in Section 4.1.2 with 100 nodes in both x and z. The initial field is shown in Figure 4-6.

4.2.2 Central Difference Scheme

A second-order central difference scheme (CDS), implicit in time, is frequently used in discretizing PDEs because it is higher order accurate, simple to implement, and more stable than its time-explicit counterpart. A two-dimensional simulation with
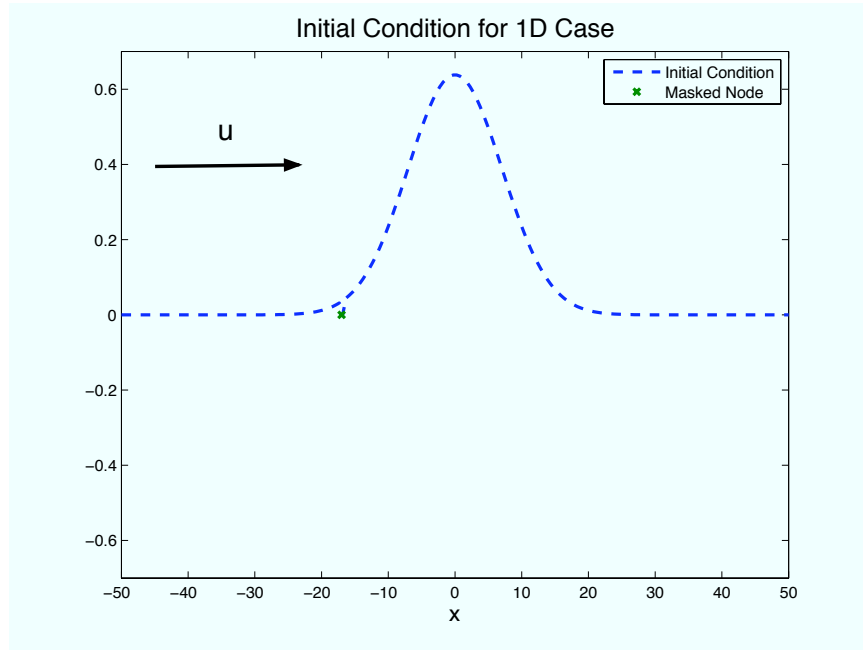
Figure 4-5: Initial condition for the one-dimensional test case.
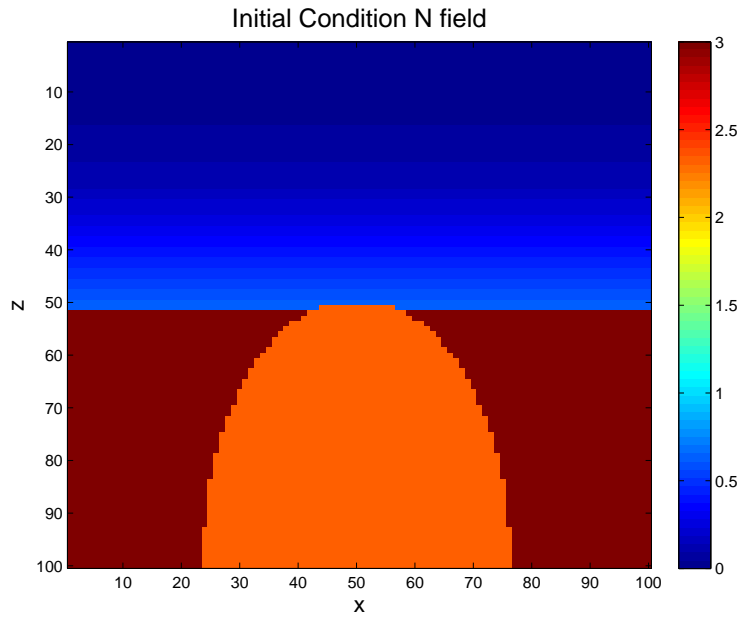
Figure 4-6: Initial condition for the two-dimensional test case.

advection *and* sufficient diffusion did not reveal any physically unrealistic features. However, in an identical simulation *without* diffusion, oscillations quickly formed at the bathymetry boundary, as in Figure 4-7. After more time, the maximum and minimum values reached several orders of magnitude above and below zero, respectively. When the bathymetry was removed, CDS with advection only did not create unrealistic results.
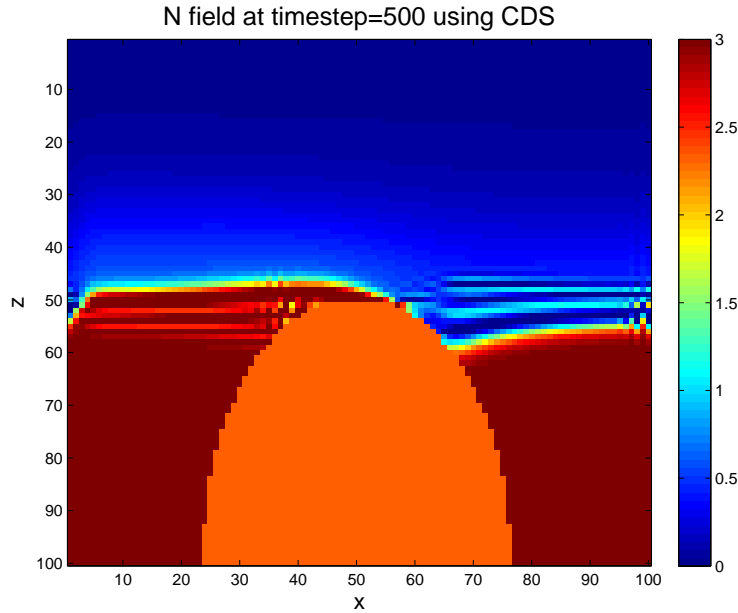
Figure 4-7: Central difference scheme in two dimensions. Spurious oscillations form at the bathymetry boundary.

Figure 4-5 shows the initial distribution (dashed line) of the one-dimensional case and the state after one cycle, or the time for a particle to advect around the domain exactly once (2010 time steps). The distribution is advected at a rate of five length units per time unit. Again, we expect all of the concentration in the system to accumulate in the node just before the masked node, leading to an impulse-type distribution. Instead, as we see in Figure 4-8, as soon as a small amount of concentration accumulates at the masked node, values of ϕ alternate between positive and negative values and grow in amplitude and propagate against the flow and enter the domain on the right because of the periodic boundary conditions.
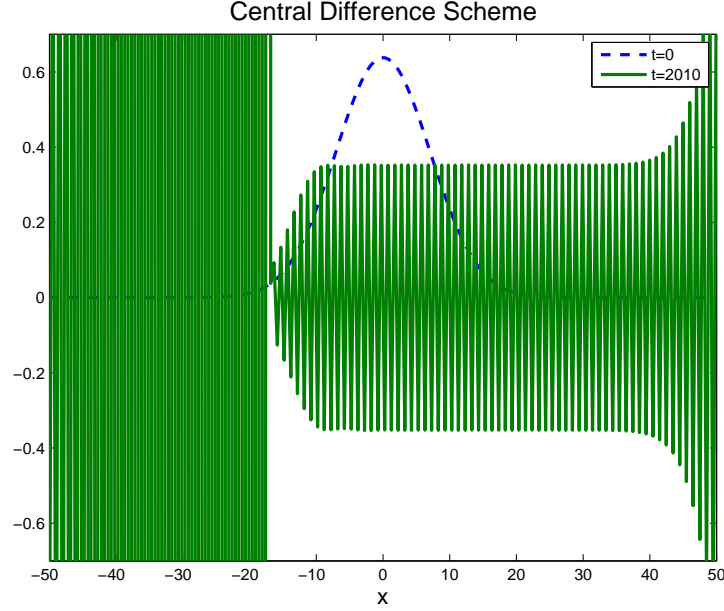
Figure 4-8: One-dimensional advection of central difference scheme with a masked node at $x = -17$. Oscillations quickly grow and propagate against the direction of flow.

The source of oscillations is illustrated with an example. If we assume constant, positive velocity u over all I nodes, using Equation 4.1 and ignoring diffusion, the change in ϕ_i with time becomes (for any interior node i):

$$\frac{\partial \phi_i}{\partial t} = -\frac{\partial (u\phi_i)}{\partial x} = u\left(\frac{\phi_{i-1}^{k+1} - \phi_{i+1}^{k+1}}{2\Delta x}\right) \tag{4.4}$$

The change of ϕ_i in time is determined by the difference in the neighboring nodes to the left $(i - 1)$ and right $(i + 1)$. Note that Equation 4.4 is now identical to a central difference scheme. First, consider the case when $(i + 1)$ is the first interior node outside of the masked node, as in Figure 4-9. If ϕ_{i+1} is very large (as we predict with a positive flow), $\frac{\partial \phi_i}{\partial t}$ will be negative.
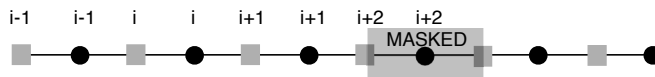
Figure 4-9: Equation 4.4 is true for interior nodes ($i - 1$ and i, in this figure).

In general, ϕ_{i+1} increases with every time step as concentration accumulates at the boundary, and will eventually (if not immediately) become larger than ϕ_{i-1}. How quickly this occurs depends on the initial condition and the magnitude of the flow. Physically, after sufficient time, we expect the ith node (and all nodes before it) to decrease to zero, so that all of the concentration in the system is in the $(i + 1)$th node. However, this is not possible using CDS. The change of ϕ_i in time will be negative because ϕ_{i+1} is very large, while ϕ_{i-1} should be the value of the advected initial condition, as in Figure 4-10, which shows the solution after three time steps. The positive values beyond the masked node are the initialized tracer values. These have not yet been affected by the oscillations.
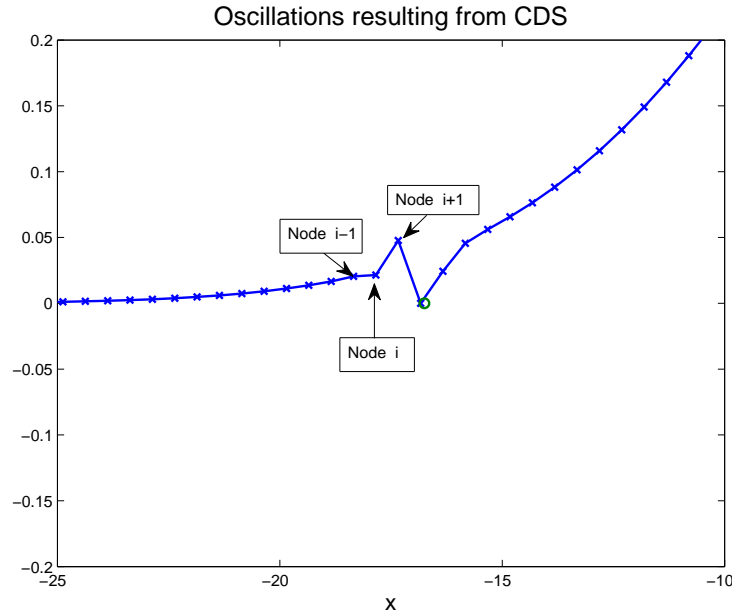
Figure 4-10: One-dimensional case after three time steps. Because concentration accumulates at the boundary $(i+1)$ and becomes larger than ϕ_{i-1}, the finite difference scheme used estimates a decrease in ϕ_i at every time step, so ϕ_i becomes more and more negative.

Once oscillations are present, they quickly grow in amplitude, as shown in Figure 4-11. The outer envelope containing the oscillations grows, therefore, $\phi_{i+1} > \phi_{i-1}$ if both are positive and $\phi_{i+1} < \phi_{i-1}$ if both are negative. From Equation 4.4, we know that ϕ_i increases if its neighbors are negative and decreases if they are positive, thus

promoting alternating, oscillatory behavior to increase in amplitude, as nodes become more and more positive or more and more negative. These oscillations propagate upstream and enter the domain on the right side because of the periodic boundary condition.
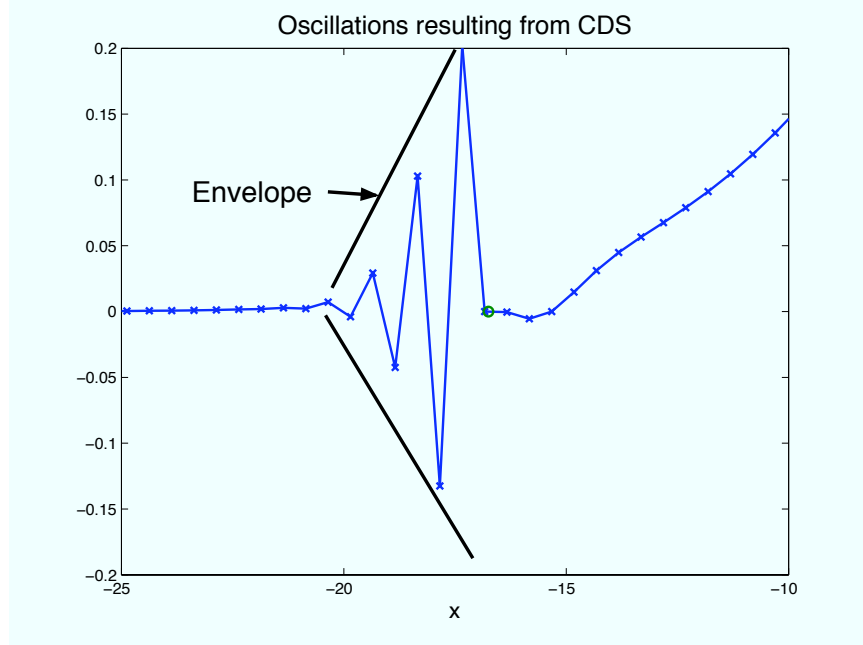
Figure 4-11: Oscillations grow in amplitude and propagate because of their alternating nature. The circular marker indicates the masked node.

The one-dimensional simulation revealed that the CDS incorrectly estimated the tracer value when a discontinuity was present. In the case with constant velocity, CDS attempts to approximate the first order derivative of ϕ with respect to x (Equation 4.4). If the tracers form a very nonlinear function, which occurs when high concentration builds up against bathymetry, severe overestimates and underestimates of the derivative lead to oscillations. Estimating derivatives of strongly nonlinear functions is a well-known limitation of finite differences.

While CDS is an appropriate scheme for many locally smooth problems, we must use another scheme that is able to model the advection dominant case and allow accumulation against bathymetry. In the two-dimensional idealized numerical simulation, vertical flow will usually prevent the tracer from building up against the bathymetry,

so the one-dimensional case presented here can be thought of as a "worst case" scenario. Further, different velocity fields and initial conditions may produce oscillations much more slowly or may never produce oscillations at all. However, we require a robust scheme that does not severely limit which physical processes and initial conditions we are able to use.

4.2.3 Donor-Cell Scheme

The donor-cell scheme is a first-order numerical scheme in space, as described by [23]. This scheme is typically used for terms of the form $\frac{d(u\phi)}{dx}$ with u and ϕ on a staggered grid, thus it is easily adaptable to our problem setup. For a positive flow, a derivative at i is estimated by taking the difference of that node with $i-1$, the node in the direction from which the concentration flows. Alternately, the derivative for a negative flow uses nodes i and $i+1$. The donor-cell scheme uses two neighboring points in its stencil, therefore the oscillations that appeared previously when using the CDS scheme are not expected to occur. Again, the time discretization is implicit. The overestimating/underestimating which is severe when a derivative is calculated based on immediate neighbors will not occur when the value of the ith node is included in the discretization. This scheme is expressed in Equation 4.5 to represent the advective term.

$$\left.\frac{\partial(u\phi)}{\partial x}\right|_i = \frac{(\phi_{i+1}(u_{i+1} - |u_{i+1}|) + \phi_i(u_{i+1} + |u_{i+1}| - u_i + |u_i|) + \phi_{i-1}(-u_i - |u_i|))}{2\Delta x}$$

(4.5)

As expected, a simple test of the donor-cell scheme in the two-dimensional domain did not reveal any oscillations. A one-dimensional test (identical to the test case in Section 4.2.2) showed that, in fact, all of the concentration advected to the masked node accumulated without oscillation (Figure 4-13).

Figure 4-14 presents a comparison of the numerical diffusivity and computation times of the CDS and donor-cell schemes after propagating one cycle (2010 time
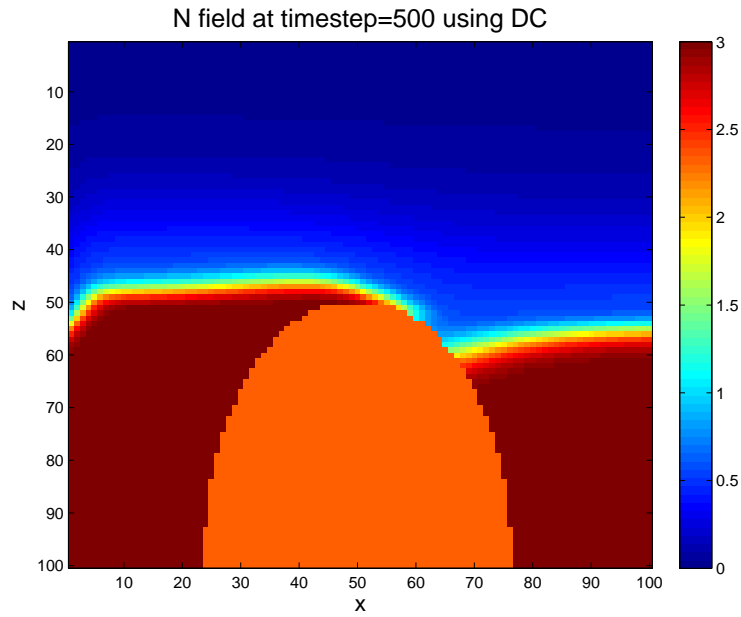
Figure 4-12: Two-dimensional test case using the donor-cell scheme. There are no oscillations, but numerical diffusion is present.
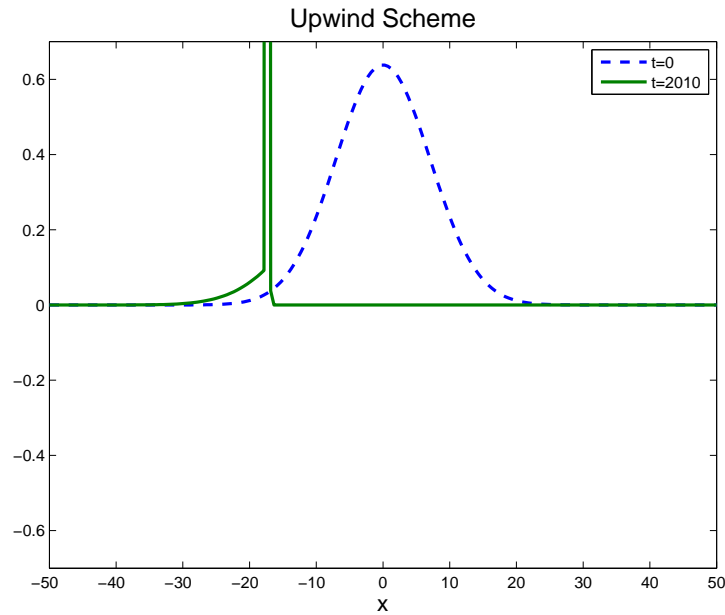

Figure 4-13: One-dimensional advection of donor-cell scheme with a masked node at $x = -17$. Unlike the case using CDS, the concentration accumulated at the boundary does not produce oscillations.

steps) in the one-dimensional domain without a masked node. Normalized spread is used as an indicator of numerical diffusion. After the Gaussian distribution is propagated, the spread of the distribution is measured at half of the maximum. This value is normalized by the initial spread measured at half the height of the initial peak. Therefore, a spread value of one indicates the distribution is perfectly unchanged after one cycle. Computation time is the averaged time, in seconds, it took to complete the computations for one cycle using MATLAB 7.4.0. Graphs shown are qualitatively informative: computational time on different machines or programs are likely to give different results, but the comparison between the two schemes remains qualitatively valid. Several different grid resolutions (from 15 to 400 nodes) give a range of spread and computation times.

For the spread versus computational time graph, we look for the scheme that has both low spread and low computational time. From Figure 4-14, we see that CDS outperforms the donor-cell scheme for all but very low resolutions. After computational times above ten seconds, the spread does not continue to decrease, but instead levels to just above one. The donor-cell scheme is diffusive, even for very high resolution grids.

For the donor-cell scheme, oscillations could not propagate because there is enough numerical diffusion in the system to smooth large negative and positive values before they are able to grow and spread. The CDS is much less diffusive, but is oscillatory. An ideal scheme would combine the avoidance of oscillations of the donor-cell scheme and the low numerical diffusivity of CDS. Therefore, the next numerical scheme we examined is a hybrid scheme, which is a weighted combination of donor-cell and CDS.

4.2.4   Hybrid Scheme

The hybrid scheme offers a weighted combination of CDS and donor-cell. The donor-cell and CDS are combined according to a weight γ: $(1-\gamma)$(D-C) $+\gamma$ CDS, where D-C is the result from the donor-cell scheme. A very low value of γ is close to first-order accuracy, like the donor-cell scheme, while a value near unity is closer to second-order accurate, like the CDS.
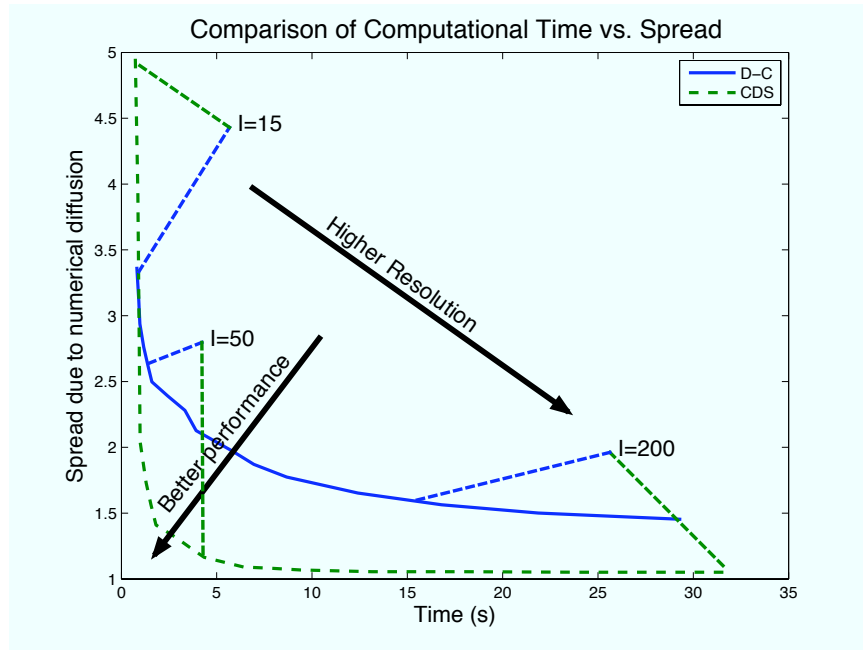
Figure 4-14: Comparison of computational time and numerical diffusion for the donor-cell scheme (D-C) and central difference scheme. Excluding very low resolution cases, the central difference scheme has much less diffusion than the donor-cell scheme. Number of nodes used to discretize the domain is shown for $I = 15$, 50 and 200.

Applying the hybrid scheme to the two-dimensional test case (Figure 4-15) reveals oscillations for higher γ values, which disappear for lower γ values. We are effectively introducing numerical diffusion by decreasing γ and for some critical value, there is enough diffusion to average the oscillations quickly enough so that they do not grow and propagate, as with the CDS case. This critical value depends on the local gradient of concentration, the rate of advection and the grid resolution.
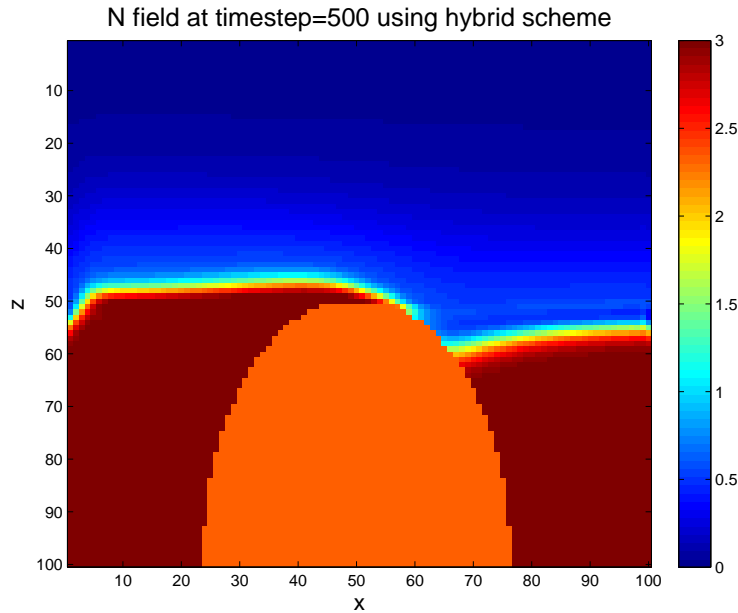
Figure 4-15: Two-dimension test case using $\gamma = 0.5$ is absent of oscillations and less diffusive than the donor-cell scheme.

By examining various γ values (0.75, 0.5, and 0.25) in the one-dimensional test case, it is clear that lower values of γ produce oscillations with smaller amplitudes that propagate more slowly, or do not propagate after a certain distance. Figures 4-16(a) – 4-16(c)) show Gaussian distributions advected over the same number of time steps with identical speeds and masked nodes. While all three values of γ produce oscillations, it is less severe for smaller values of γ. Still, for even very small γ (0.005), small oscillatory behavior can be seen (Figure 4-16(d)). Therefore, using the hybrid scheme does not give us the non-oscillatory, non-diffusive results we desire.
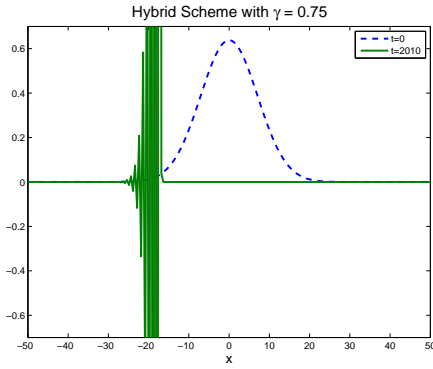
(a) One-dimensional advection of hybrid scheme with $\gamma = 0.75$ with masked node at $x = -17$.
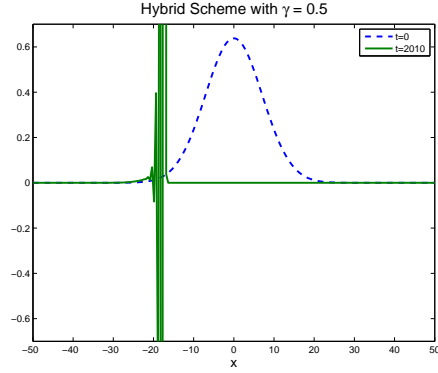
(b) One-dimensional advection of hybrid scheme with $\gamma = 0.5$ with masked node at $x = -17$. Oscillations have smaller amplitude and have propagated less than in the $\gamma = 0.75$ case.
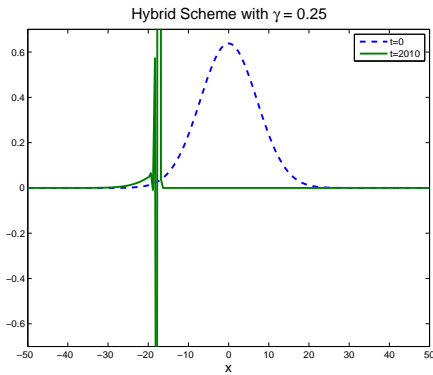
(c) One-dimensional advection of hybrid scheme with $\gamma = 0.25$ with masked node at $x = -17$. Again, we see smaller oscillations in the cases with larger γ values.
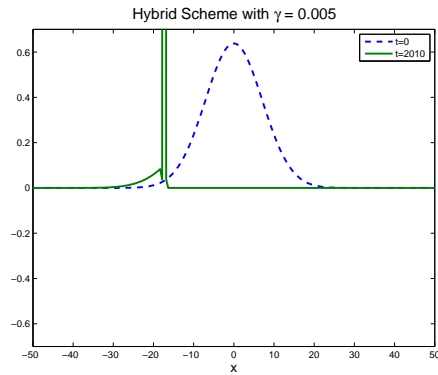
(d) One-dimensional advection of hybrid scheme with $\gamma = 0.005$ with masked node at $x = -17$. Even for very small γ, oscillatory behavior is present.

Figure 4-16: Hybrid scheme with various values of γ. Even for very small γ, oscillatory effects are present.

4.2.5   Weighted Essentially Non-Oscillatory (WENO) Scheme

The WENO scheme ([51]) is a higher-order accurate finite difference or finite volume scheme specifically created for problems (often in computational fluid dynamics) which contain piecewise smooth solutions with discontinuities. While the discretized equation is linear, a nonlinear adaptive procedure is used to avoid discontinuities in the interpolation process by choosing the smoothest stencil *locally*. WENO chooses a convex combination of all possible stencils, instead of using the single smoothest stencil (as is the case with the Essentially Non-Oscillatory (ENO) scheme [28]). These schemes have been particularly successful in many problems, especially those containing shocks or compressible turbulence simulations [51], but this scheme has not yet been applied to coupled physics-biology modeling.

Because masking is used in the numerical simulation for idealized physics and biology, there are zero velocity values and fixed tracer values under this mask. Outside of the bathymetry, however, there are nonzero and changing values, especially for nutrients, which dominate in deep water. Therefore, a sharp discontinuity is present at the boundary of the bathymetry and the previously used finite difference methods unsuccessfully attempt to estimate the derivative of a nonlinear function using conventional methods.

To avoid numerical diffusion, a finer mesh or higher-order scheme is necessary. However, we are limited to the mesh size due to computational cost, and higher order schemes introduce oscillations near a discontinuity, which do not decay in magnitude when the mesh is refined. Prior to the WENO scheme, many people used explicit artificial viscosity or limiters to eliminate or reduce such oscillations. However, artificial viscosity depends on fine tuning the individual problem at the discontinuity and the limiters force accuracy to become first order near all extrema, including smooth extrema. In addition, limiters are not self-similar (mesh size dependent parameter exists) [51].

The order of accuracy for the WENO scheme is determined by the number of stencils, and number of points in those stencils. As shown in Figure 4-17, we use

three stencils, each with three points, so that the scheme is fifth-order accurate in smooth regions and third-order accurate near discontinuities. Note that this scheme, unlike the previous schemes, is explicit in time. However, the numerical stability issues commonly associated with explicit schemes do not arise in using WENO. We implement this scheme in one dimension (due to the OSM) on a uniform staggered grid (Arakawa C-grid).
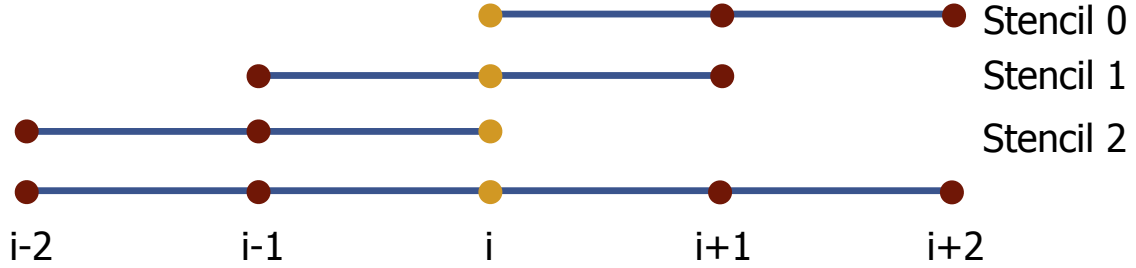
Figure 4-17: Three stencils used in the WENO scheme.

A weight ω_r is assigned to each stencil r, determined by a smoothness indicator β_r. The smoothness indicators are computed using the local smoothness of the concentration values ϕ, or "cell-averaged" described by [51]. Boundary values (values of the tracer on the velocity nodes) of this function are reconstructed using Equations 4.7 (only the case for positive flow, or "upwind" flow, is shown). To account for flows in both directions, an analogous scheme was constructed for negative flow. Negative flow is also referred to as "downwind."

$$\omega_r = \frac{\alpha_r}{\sum_{s=0}^{2} \alpha_s} \quad \text{for } r = 0, 1, 2$$

where

$$\alpha_r = \frac{d_r}{(\epsilon + \beta_r)^2}$$

$$d_0 = \frac{3}{10}, d_1 = \frac{3}{5}, d_2 = \frac{1}{10}$$

$$\beta_0 = \frac{13}{12} (\phi_i - 2\phi_{i+1} + \phi_{i+2})^2 + \frac{1}{4} (3\phi_i - 4\phi_{i+1} + \phi_{i+2})^2$$

$$\beta_1 = \frac{13}{12} (\phi_{i-1} - 2\phi_i + \phi_{i+1})^2 + \frac{1}{4} (\phi_{i-1} - \phi_{i+1})^2$$

$$\beta_2 = \frac{13}{12} (\phi_{i-2} - 2\phi_{i-1} + \phi_i)^2 + \frac{1}{4} (\phi_{i-2} - 4\phi_{i-1} + 3\phi_i)^2$$

$$(4.6)$$

where $\epsilon = 10^{-6}$ to avoid a zero denominator, $\omega_r \geq 0$ and $\sum_r \omega_r = 1$ for stability and consistency, and d_r is always positive and $\sum_r d_r = 1$ for consistency. When a discontinuity is encountered, the weights associated with the stencils that cross that discontinuity become nearly zero so that only stencils that do not cross the discontinuity are used.

$$\hat{\phi}_i = \frac{1}{3}\phi_{i-2} - \frac{7}{6}\phi_{i-1} + \frac{11}{6}\phi_i$$

$$\hat{\phi}_{i+1} = -\frac{1}{6}\phi_{i-1} + \frac{5}{6}\phi_i + \frac{1}{3}\phi_{i+1}$$

$$\hat{\phi}_{i+2} = \frac{1}{3}\phi_i + \frac{5}{6}\phi_{i+1} - \frac{1}{6}\phi_{i+2}$$

$$(4.7)$$

where $\hat{\phi}$ values are tracers values on *velocity* nodes and ϕ are tracer values on *tracer* nodes. The weighted combinations give a new approximation to the tracer value on the *velocity* node, ϕ^*.

$$\phi_i^* = \omega_0 \hat{\phi}_{i+2} + \omega_1 \hat{\phi}_{i+1} + \omega_2 \hat{\phi}_i$$

And thus Equation 4.3 becomes:

$$\left. \frac{\partial \phi}{\partial t} \right|_i = -\frac{u_{i+1}\phi_{i+1}^* - u_i \phi_i^*}{\Delta x}$$

It is apparent that a staggered grid is advantageous when implementing the WENO scheme, as both velocity and tracer nodes are frequently used. The "boundary values" referred to by Shu, et. al. ([51]), correspond to the nodes for horizontal (vertical) velocity in the x (z) direction. "Cell-centered" values are the tracer nodes, used for the biological concentration values.

The two-dimensional test case using WENO presents a realistic solution free of oscillations, as shown in Figure 4-18. Several different bathymetries, flows (which satisfy CFL), and values of concentrations were tested and oscillations never occurred. The WENO scheme successfully avoids oscillations.
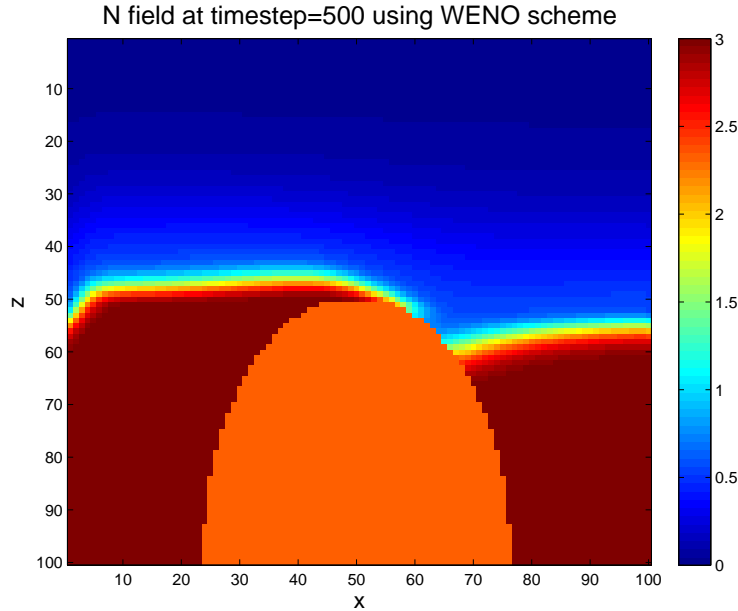

Figure 4-18: The WENO scheme is not oscillatory and produces a realistic result.

Performing the same one-dimensional test case as the other numerical schemes

demonstrates that the concentration accumulates against the masked node (Figure 4-19), as with the donor-cell scheme.
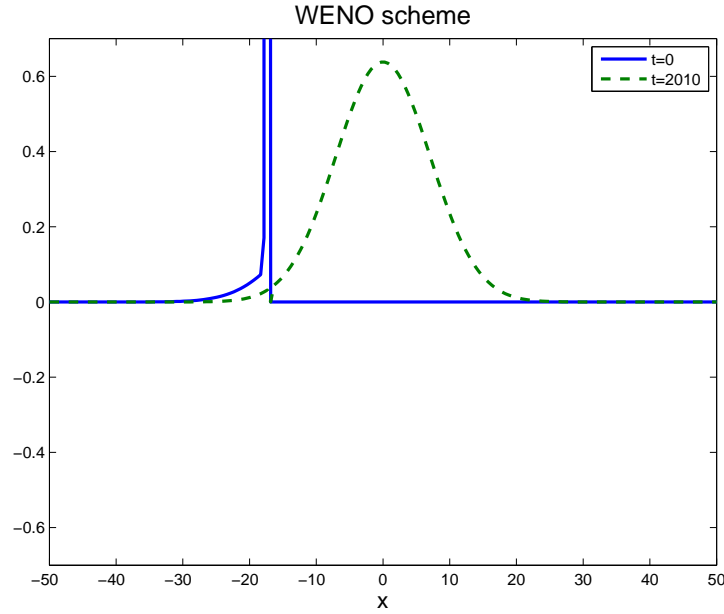

Figure 4-19: One-dimensional advection of WENO scheme with a masked node at x=-17.

The WENO scheme is only attractive compared to the donor-cell scheme if it is less numerically diffusive for comparable computational cost and resolution. Figure 4-20 illustrates that, for higher resolutions, the WENO scheme outperforms the donor-cell scheme. This graph was constructed using the same methods described in Section 4.2.3. We can see that for comparable computational times, WENO is much less diffusive for the higher resolution schemes. Conversely, if we set a limit for maximum spread allowed, the WENO scheme has much faster computation times for normalized spread values below about 2.4. The donor-cell scheme performs better only for very low resolutions (less than 60 nodes). For our purposes, resolutions this low will never be used.

The donor-cell scheme uses matrix inversion to compute the tracer values for the next time step. For a time-varying velocity, which will be used for many simulations (for example, to model tidal forces), this matrix is inverted for each time step, for as
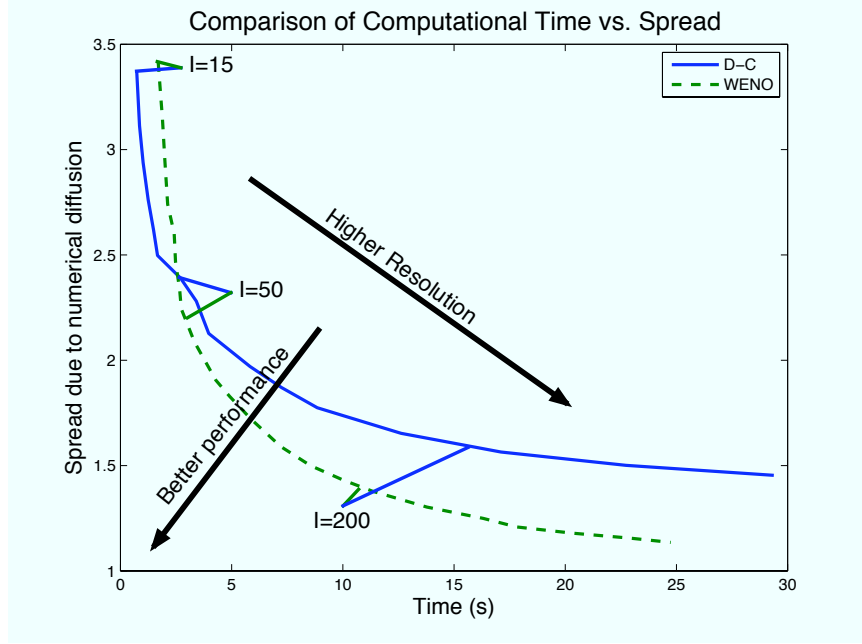
94

Figure 4-20: Comparison of computational time versus spread due to numerical diffusion for the donor-cell and WENO schemes. WENO is faster and less diffusive for higher resolutions. Number of nodes used to discretize the domain is shown for $I = 15$, 50 and 200.

many rows and columns exist (due to the OSM). Therefore, the matrix is inverted IxJxTS times, if TS is the total number of time steps. The matrix is nearly tridiagonal however, because of the periodic boundary conditions, there are extra entries not on the main diagonal or the immediate off-diagonals. The Thomas Algorithm takes advantage of a tridiagonal matrix structure and significantly reduces the number of operations needed to compute an inverse. For a tridiagonal system with extra entries from periodic boundary conditions, a modified version of the Thomas Algorithm, using the Sherman-Morrison formula, can be used [9].

Computation times and diffusion were remeasured using the adapted Thomas Algorithm, and the results for the donor-cell scheme using the traditional inversion, the donor-cell scheme using the adapted Thomas Algorithm and the WENO scheme were compared, as shown in Figure 4-21.

However, while the adapted Thomas Algorithm does outperform the traditional inversion using the donor-cell scheme, Figure 4-21 shows that the WENO scheme is
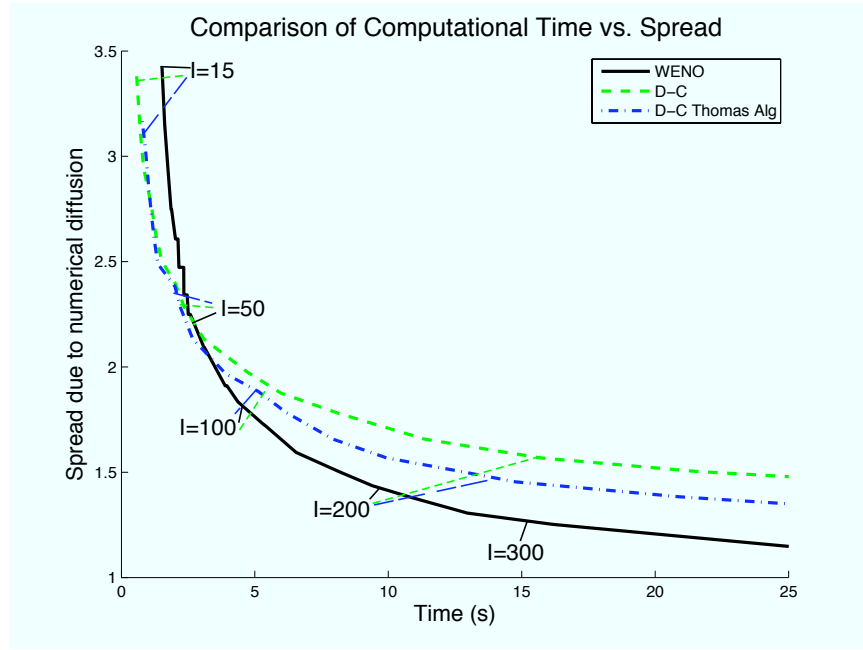
Figure 4-21: While the modified Thomas Algorithm donor-cell scheme outperforms the traditional donor-cell scheme, the WENO scheme is better for all but low resolutions. Diffusion and time are labeled by number of nodes used to discretize the domain (I =15, 50, 100, 200 and 300). Only I =300 is shown for the WENO scheme because the other two schemes have computation times greater than 25 seconds for 300 nodes.

still superior except for low resolution grids. To model biological behavior, high resolution is important to be able to resolve features on the order of meters, especially in the vertical direction. Therefore, the WENO scheme is used in all following idealized numerical simulations to represent the advection terms in x and z of Equations 2.3. The diffusion terms are implemented using a second-order CDS to minimize computational costs.

After examining several schemes, the WENO scheme is the only one that avoids oscillations and is higher order accurate. The central difference scheme developed oscillations very quickly, but had low numerical diffusivity for high resolutions. The donor-cell scheme was non-oscillatory, but suffers from worse numerical diffusion for comparable computational costs. The hybrid scheme required extremely low values of the weight parameter γ to avoid oscillations, essentially becoming the donor-cell scheme.

4.2.6   Verification of the WENO Scheme

To verify the results seen from using the WENO scheme, we compare the simulation developed in this chapter with a simulation on an unstructured grid using a Discontinuous-Galerkin (DG) scheme [47] (simulation developed in [57]). Matching bathymetries, boundary conditions, flow fields and initial conditions were used and are the same as discussed in Section 4.1. The streamlines for the flow are presented in Figure 4-22. The biological equations use parameters from Equation 3.5.

Figure 4-23 presents a comparison between the two schemes for three different times. While the initial frames are almost identical, some differences are seen when the fields are evolved in time. Namely, the WENO scheme is a more diffusive than the DG scheme, which is able to resolve sharp gradients. However, for comparable computational times, we are able to increase the resolution of the simulation that uses the WENO scheme, so numerical diffusivity will decrease. The DG scheme produces artificial and persistent oscillations, called Gibbs phenomena, at the interface where the tracer fields are discontinuous. Additionally, slight accumulation of biomass occurs on the left side of the bathymetry for the DG scheme only, though we do not expect
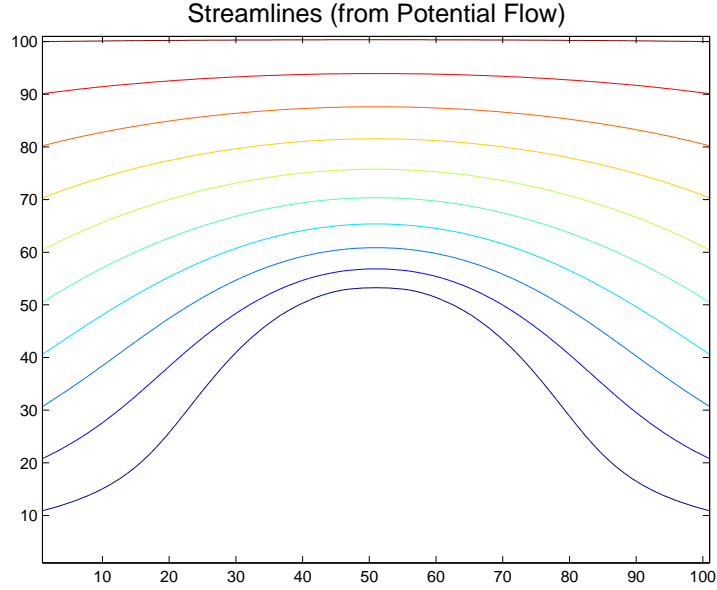
Figure 4-22: Streamlines for potential flow over an elliptical bathymetry.

results near the boundary to be reliable because of the limitations of potential flow. The basic biological features are very similar, both qualitatively and quantitatively. Therefore, because an analytical solution is not obtainable, the very good agreement between the two independent methods to represent the same system indicates that both schemes accurately represent the coupled physics and biology of Equations 2.3.

Numerical models for coupled physics and biology are commonly restricted to include some minimum amount of diffusion to avoid oscillations. Using the WENO scheme allows us to investigate a range of physical processes without needing to fine tune case-specific parameters or be restricted to a specific set of initial conditions or velocity fields. Using OSM and masking on a C-grid simplifies implementation of the WENO scheme. The combination of techniques presented here can solve many coupled systems of advection-dominant PDEs and can be applied to applications other than coupled physics and biology.
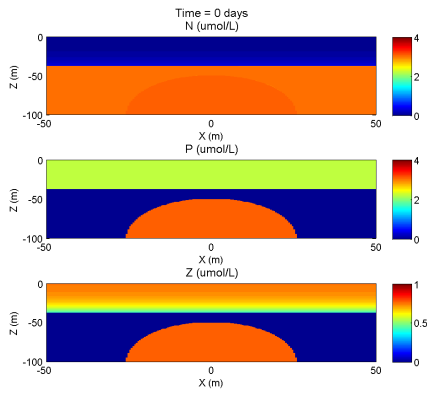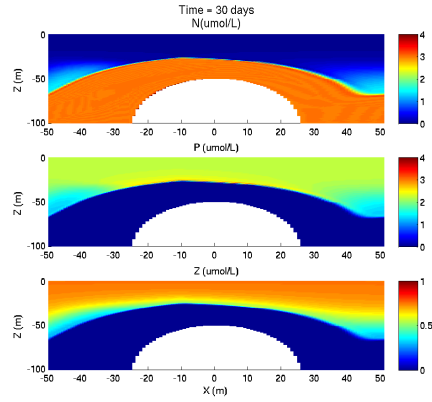
(a) Simulation using WENO scheme at t=0 days.
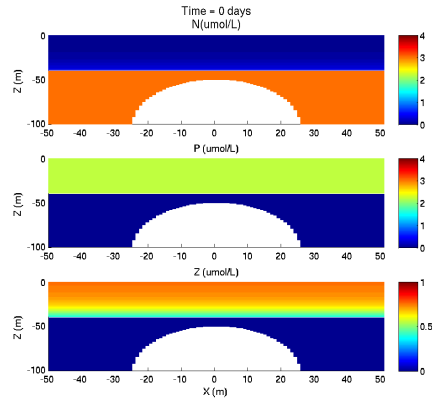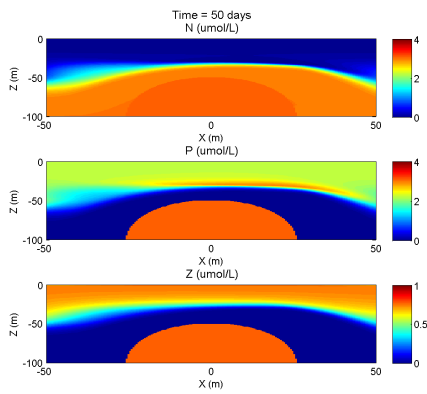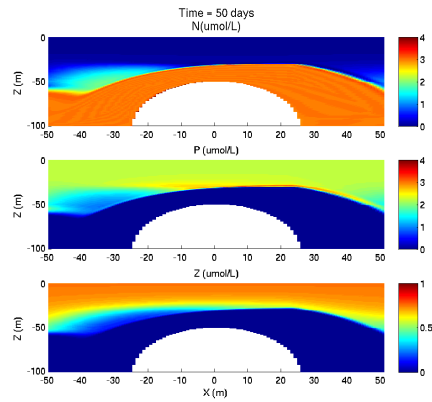

(b) Simulation using DG scheme at t=0 days.
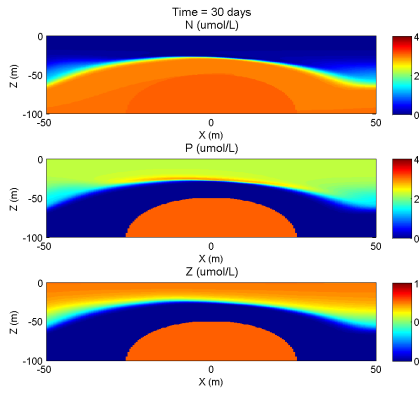
(c) Simulation using WENO scheme at t=30 days.

(d) Simulation using DG scheme at t=30 days.

(e) Simulation using WENO scheme at t=50 days.

(f) Simulation using DG scheme at t=50 days.

Figure 4-23: Comparison between simulations using the WENO scheme and Discontinuous-Galerkin [57].

Chapter 5

Physical-Biological Interactions with Tides in the San Bernardino Strait

In this chapter, we compare two- and three-dimensional realistic simulations of the interaction between tides and biology in the San Bernardino Strait. Tides can produce strong mixing in coastal waters, create internal waves over bathymetry, and suspend bottom sediment. Such mixing can create interesting biological features, even in two dimensions. Thus we will focus on the relationship between tides and biology as an example of the range of features that our two-dimensional idealized simulation is able to represent. Tidal frequencies range from semi-diurnal to diurnal to even longer periods. We will consider a range of tidal frequencies, but will focus on periods less than one month. A more detailed discussion of tides can be found in [54].

Similar cases are initialized in both two and three dimensions with bathymetry and initial conditions motivated by San Bernardino Strait. For the two-dimensional case, details of the bathymetry, velocity field, initial conditions, boundary conditions and parameters are discussed in Section 5.1. Cases with different tidal frequencies, parameters and levels of diffusion are examined and compared.

The three-dimensional case is simulated in MSEAS. Details of initialization, flow fields, bathymetry and parameters are discussed in Section 5.2. We present a new

technique of initializing the biology field using Objective Analysis and region-specific chlorophyll profiles. The results from the three-dimensional case are studied and compared to the two-dimensional case.

5.1 Two-dimensional Simulation

We conduct two-dimensional idealized simulations of tidal forcing in a strait to determine the effects on biology. The setup is motivated by the San Bernardino Strait in the Philippines, which shows strong tidal forcing from the *PhilEx* Regional Cruise IOP09, conducted in February and March of 2009. The WENO scheme, discussed in Chapter 4, is used to discretize Equations 2.3 in order to represent the interaction between biology and physics.

Literature cites nitrogen as the limiting nutrient for most of the Philippine Archipelago and surrounding areas, with the exception of summer, when phosphorus may simultaneously become deficient ([8], [7], [60], [40], [55]). Parameters for the NPZ equations (Equations 2.3) were found in literature for the Philippines and surrounding areas. These values and sources are presented in Table 5.1.

Parameter	Source
$u = 1.4\frac{\mu\text{mol}}{\text{day}}$	[29]
$N_T = 3\frac{\mu\text{mol}}{\text{L}}$	
$k_s = 0.9\frac{\mu\text{mol}}{\text{day}}$	[29]
$d_p = 0.1\frac{\mu\text{mol}}{\text{day}}$	[22]
$g = 1\frac{\mu\text{mol}}{\text{day}}$	[32]
$a = 0.75$	[15]
$d_z = 0.2\frac{\mu\text{mol}}{\text{day}}$	[22]
$h = 17\text{m}$	[18]
$\nu = 0.2\mu\text{mol}^{-1}$	[22]

Table 5.1: Region specific parameters for the Philippine Archipelago.

5.1.1 Bathymetry

For the bathymetry used in the two-dimensional case, we developed an algorithm to find the deepest path through the San Bernardino Strait using data with one-minute resolution from Smith and Sandwell (v.10.1) [53] in the domain 124^oE-125^oE and $12^oN-13.1^oN$ (Figure 5-1). The algorithm uses a modified Dijkstra's algorithm [14], also known as the "shortest path algorithm," altered by recording the depth at each point instead of the distance between two points. The algorithm begins on the southern border of the domain and marches northward row by row. As described, the algorithm will provide a collection of deepest points that are not in any sense connected to form a path. To introduce the notion of a path, we imposed a limiter so that points selected in adjacent rows are restricted to be at most one column apart; the path is restricted to moving to a neighboring node (either one node north, one node northeast, or one node northwest). The sum of depths is recorded for each path; this is our metric for determining the "deepest path" through the strait. As the algorithm marches northward, only the sums and paths for the deepest paths are kept at each stage, as the deepest path for any new path starting from the current row would use the paths already recorded for an overall optimal path. The algorithm ends at the northern border of the domain, where the node on that row with the largest negative summed depths is selected as the deepest path. We then find the bathymetry associated with this deepest path. Finally, we apply a Gaussian low pass filter to the resulting bathymetry of the deepest path and record the depth profile, using the smoothed bathymetry along the deepest path. This bathymetry, with flat bathymetry added on each side for reasons discussed in Section 5.1.3, is shown in Figure 5-2.

5.1.2 Velocity Field

We assume the flow is inviscid and irrotational and that the strait is narrow enough so that rotational effects can be ignored (this is true if the ratio of the channel width to the Rossby radius is small [52], [45], [13]). For the San Bernardino Strait, the
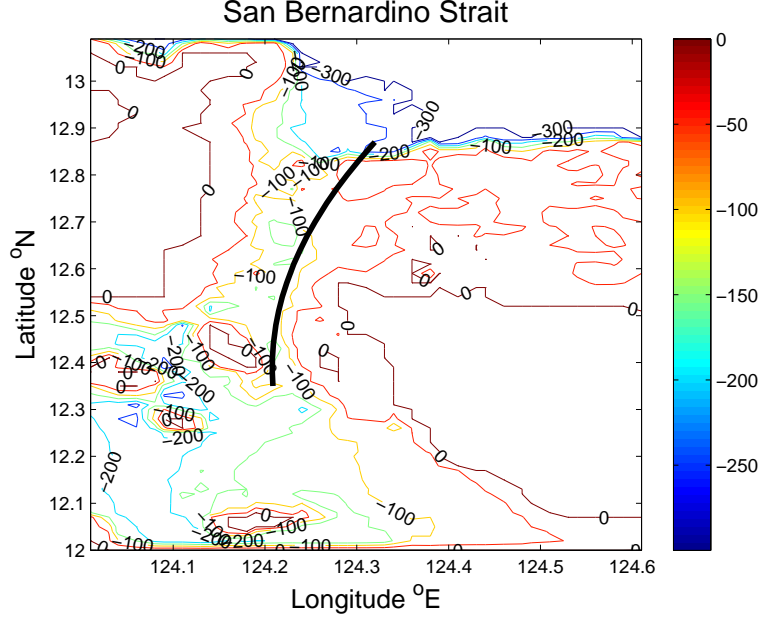
Figure 5-1: Topography of San Bernardino Strait from Smith and Sandwell. The dark line is the shortest path through the strait as described in Section 5.1.1.

channel width is about 12km. The Rossby radius is:

$$R_D = \frac{(gD)^{1/2}}{f_o} = \frac{(9.81m/s^2 100m)^{1/2}}{2 * 7.2921x10^{-5}rad/s \sin(12.5^o)} \approx 1000km$$

Therefore,

$$\frac{W}{R_D} = \frac{12km}{1000km} \ll 1$$

Therefore the ratio of the channel width to the Rossby radius is sufficiently small and rotational effects can be neglected. Additionally, for uniform bathymetry and geometry across the strait, the flow becomes two-dimensional with a rigid lid approximation if the Froude number is small and can be expressed using a velocity potential.

$$Fr = \frac{V}{\sqrt{g\frac{A}{W}}} = \frac{40cm/s}{\sqrt{9.81m/s^2 * 12km * 100m/12km}} \ll 1$$

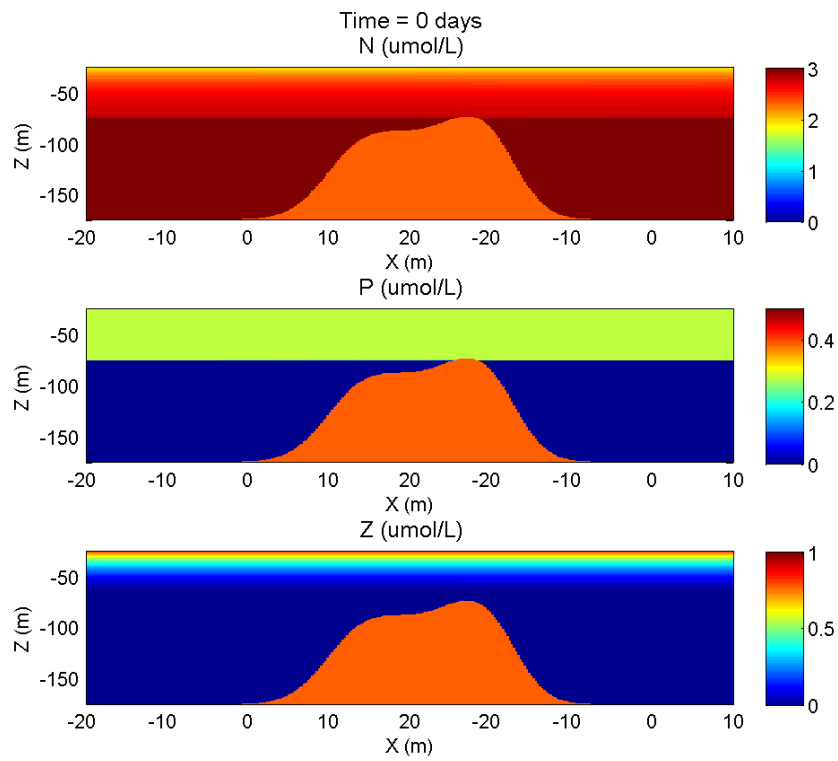Frictionless, rigid surfaces bound the top and bottom of the domain. The resulting

Figure 5-2: Bathymetry and initial condition for the two-dimensional simulations of the San Bernardino Strait.

governing equation is the Laplacian of the velocity potential. A similar setup was used by Signell [52] for tidal flow over elliptic and Gaussian-shaped coastal headlands, using the vertically averaged velocity for dynamics in the horizontal plane instead. The flow field resulting from this method does not accurately model flow at the bathymetry boundary because we assume frictionless flow. For boundary conditions, we assume no flow through the ocean bottom or air-sea interface and unit velocity at the side boundaries, which may be scaled later. The resulting streamlines are shown in Figure 5-3.
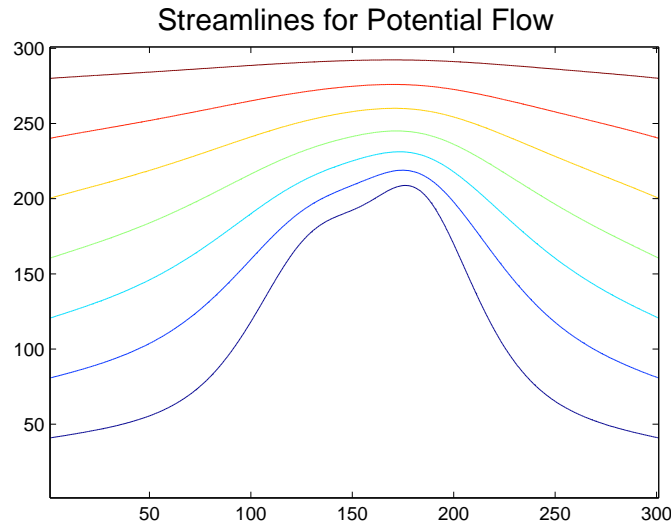

Figure 5-3: Streamlines of the potential flow resulting from the bathymetry of the San Bernardino Strait.

We studied generalized inverse high-resolution data on barotropic tides [38] to determine the magnitude and frequency of oscillation with which to force our flow. For the months of February and March, a maximum velocity of about 100 cm/s is observed for most days. Two different tidal frequencies are observed: for events with stronger flow, velocity changes direction four times in one day (semidiurnal), otherwise it changes twice in a day (diurnal). Dominant tidal constituents in the San Bernardino Strait, in order of significance, are M2, S2, K1, and O1 [38], so the semidiurnal constituents (M2 and S2) are dominant, followed by the diurnal constituents (K1 and O1). We will incorporate this into our model by examining

both cases and comparing them against an identical case without oscillating flow.

5.1.3   Biology Initialization

The biology fields were initialized using the equilibrium solution of the steady state equations without flow (Equations 3.4). We used parameter values found from the literature (see Table 5.1) which predict stable solutions (using the methods in Chapter 3). Periodic boundary conditions are imposed in the x-direction. We are able to implement a periodic boundary condition by extending the domain in the x-direction so that the problem becomes semi-infinite and the biology which leaves one side never re-enters the portion of the domain we are interested in (that is, over the bathymetry). The field far from the bathymetry (in the x-direction) is present only to create a semi-infinite domain and should not influence the dynamics over or around the strait bathymetry.

5.1.4   Cases

Four different oscillation frequencies were examined in test cases, with two frequencies corresponding to the semidiurnal and diurnal tidal constituents observed for this strait, one zero frequency case for comparison and a much lower frequency corresponding to the longer period tidal constituent. Cases with and without diffusion are compared. Additionally, different sets of parameters are examined. The twelve cases are summarized in Table 5.2.

5.1.5   Comparison of Time Scales

Using different parameter sets and oscillation frequencies leads to several different time scales. Biological interaction is more active if the time scale of the flow is longer than the time scale of the biological reaction terms. If the state variables that are at equilibrium at one depth level are moved vertically by the flow, a longer physical time scale provides the biology sufficient time to interact completely and adjust to the new depth level. Examining the terms of Equation 2.3, several time scales result

Case No.	Frequency	Period	Diffusion	Parameters
1	0 cycles/day	∞	None	Table 5.1
2	2 cycles/day	0.5 days (semidiurnal)	None	Table 5.1
3	1 cycle/day	1 day (diurnal)	None	Table 5.1
4	2 cycles/day	0.5 days (semidiurnal)	$\kappa = 0.1$	Table 5.1
5	1 cycle/day	1 day (diurnal)	$\kappa = 0.1$	Table 5.1
6	2 cycles/day	0.5 days (semidiurnal)	None	Table 5.3,[6]
7	1 cycle/day	1 day (diurnal)	None	Table 5.3,[6]
8	0.1 cycles/day	10 days (longer period)	None	Table 5.1
9	0 cycles/day	∞	None	No biology
10	2 cycles/day	0.5 days (semidiurnal)	None	No biology
11	1 cycle/day	1 day (diurnal)	None	No biology
12	2 cycles/day	0.5 days (semidiurnal)	None	Table 5.3,[6]; 2x vel

Table 5.2: Two-dimensional cases examined using the idealized numerical simulation. Varying frequencies, parameters and levels of diffusion are studied.

and are dependent upon the value of concentration and the depth level at a specific point. Figure 5-4 shows how the time scales of five reaction terms vary with depth, using the equilibrium values of N, P, and Z, where:

$$
\begin{aligned}
A &= \frac{u e^{z/h} P N}{N + k_s} \\
B &= d_p \\
C &= \frac{g}{\nu} \frac{Z}{P} (1 - e^{-\nu P}) \\
D &= \frac{ag}{\nu} (1 - e^{-\nu P}) \\
E &= d_z
\end{aligned}
\tag{5.1}
$$

From Figure 5-4, the maximum biological reaction time scale is approximately 0.08 days and the minimum is about 0.016 days for the euphotic zone. Using the region-specific parameters from Table 5.1 gives slightly longer biological reaction time scales. From Figure 5-5, we see that the time scales range from zero days to 0.2 days. Again, here we assume the equilibrium values for the state variables. The shortest time scale is dominant for any depth and set of biological state variables.

We are interested in the size of the biological reaction time scale with respect to
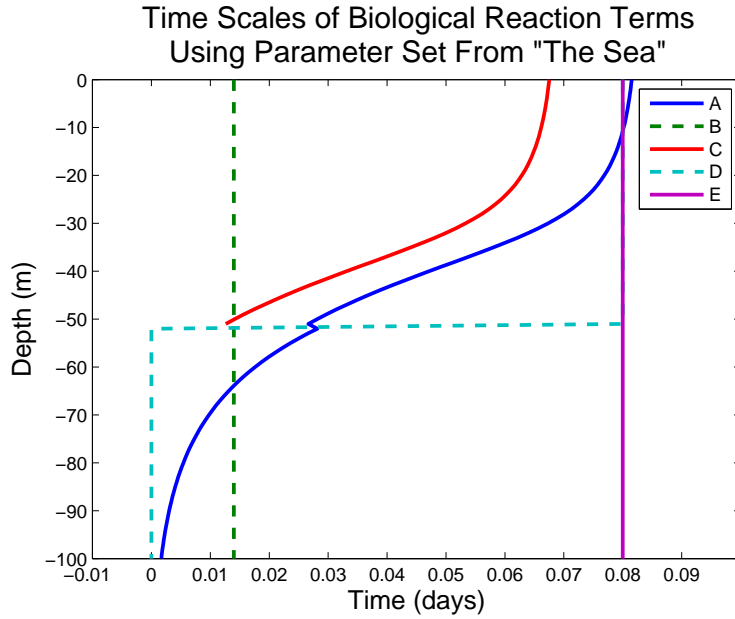
Figure 5-4: Time scales for the biological reaction terms of Equation 2.3 using parameters from Equation 3.5. These time scales vary in depth and with respect to concentration of biological variables.
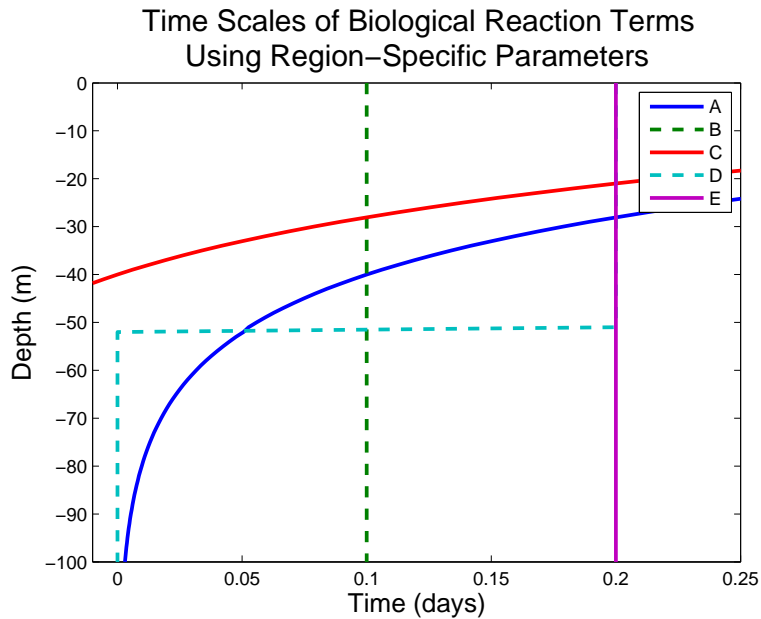

Figure 5-5: Time scales for the biological reaction terms of Equation 2.3 using region-specific parameters from Table 5.1. This set of parameters leads to slightly longer time scales than the previous set of parameters.

the physical time scale of the system. The physical time scale is either the period of oscillation (listed in Table 5.2) or the time it takes for a parcel of fluid to advect over the bathymetry (about four days), whichever is shorter. The physical time scale should be greater than the biological reaction time scale for the biological state variables to be affected by the changing depth levels. Because the biology fields are initialized using the equilibrium values, the state variables will only change if they move vertically. If they are transported too quickly and then returned to the initial depth level, very little biological activity will occur. Comparing our time scales, we see that the physical time scale is longer than the biological reaction time scale for all frequencies. Slower oscillations have longer time scales, so we expect more biological activity for longer tidal periods.

5.1.6 Results

From Case 1, we see in Figure 5-6 that non-oscillatory flow creates increased biological activity (namely a bloom in phytoplankton) because of the vertical velocities resulting from the topography. This bloom forms in the first few days and then continues to advect around because of the periodic boundary conditions, until a system equilibrium is reached. Compared to Case 9 (Figure 5-14), the case without biological reaction, the phytoplankton bloom is apparent in the top 50 meters.

For Cases 2 and 3 (Figures 5-7 and 5-8), the oscillations are too fast to allow sufficient vertical transport for nutrient-rich water to reach shallower depths. Cases 10 and 11 (Figures 5-15 and 5-16), the comparable cases without biological reaction, actually show a *more* gradual gradient in depth (most noticeably in the phytoplankton field above the bathymetry). The sharper gradient is maintained in the cases with biological reaction (in Cases 2 and 3) because the state variables attempt to move back to their steady equilibria (discussed in Chapter 3). For example, in Case 2, as high concentrations of phytoplankton travel deeper, they die quickly because of the lack of light. However, in Case 10, the tracer simply travels deeper. While the oscillations are too fast in Cases 2 and 3 to allow biology to react, the system does adjust for the bathymetry, as we can see with the evolution in time right above the bathymetry in

Figures 5-7 and 5-8. Note that some "mixing" occurs because of numerical diffusion, which becomes more severe when a thin filament of high concentration is surrounded by very low concentration (or vice versa). Adding diffusion to the oscillatory flows (Cases 4 and 5) increases mixing, as expected, but increased biological activity still is not present. These results are presented in Figures 5-9 and 5-10.

The two-dimensional and three-dimensional biological models require different sets of parameters, making it difficult to match parameters exactly. Cases 6 and 7 use a new set of parameters that more closely represent those used in the three-dimensional model (to be discussed in Section 5.2). These cases are similar to Cases 1 and 2 in that they have the same frequencies and do not include diffusion. Similarly, the frequencies are too fast to allow sufficient vertical transport. The new set of parameters results in higher zooplankton concentrations and lower nutrient concentrations, especially near the surface. While the time scales for the two biological parameter sets do differ slightly, as discussed in Section 5.1.5, the rates are usually within a factor of two so a significant difference is not seen for the cases presented here.

Case 8 uses very low frequency oscillations, representing the longer tidal periods. A physical time scale $O(10 \text{ days})$ is sufficiently longer than previous time scales and biological reaction time scales, so we expect more biological activity than in the semidiurnal and diurnal cases. Additionally, longer periods allow biomass to travel further, which is especially important in the vertical direction. As Figure 5-13 shows, our predictions are correct. Increased biological activity occurs for all three state variables, but most noticeably for phytoplankton, which blooms over the bathymetry, especially when the tide changes direction. Only the biology over the bathymetry should be studied because of the semi-infinite domain implemented to allow periodic boundary conditions.

To study the effect of physical time scales, Case 12 has high frequency oscillations (semidiurnal) and *twice* the velocity of previous cases and uses the parameters in Table 5.1. Therefore, a parcel of fluid moves an equal distance in this case and in the low frequency (diurnal) case (Case 3) with the original velocity. Although the two cases have different time scales, Figures 5-8 (Case 3) and 5-17 (Case 12) are

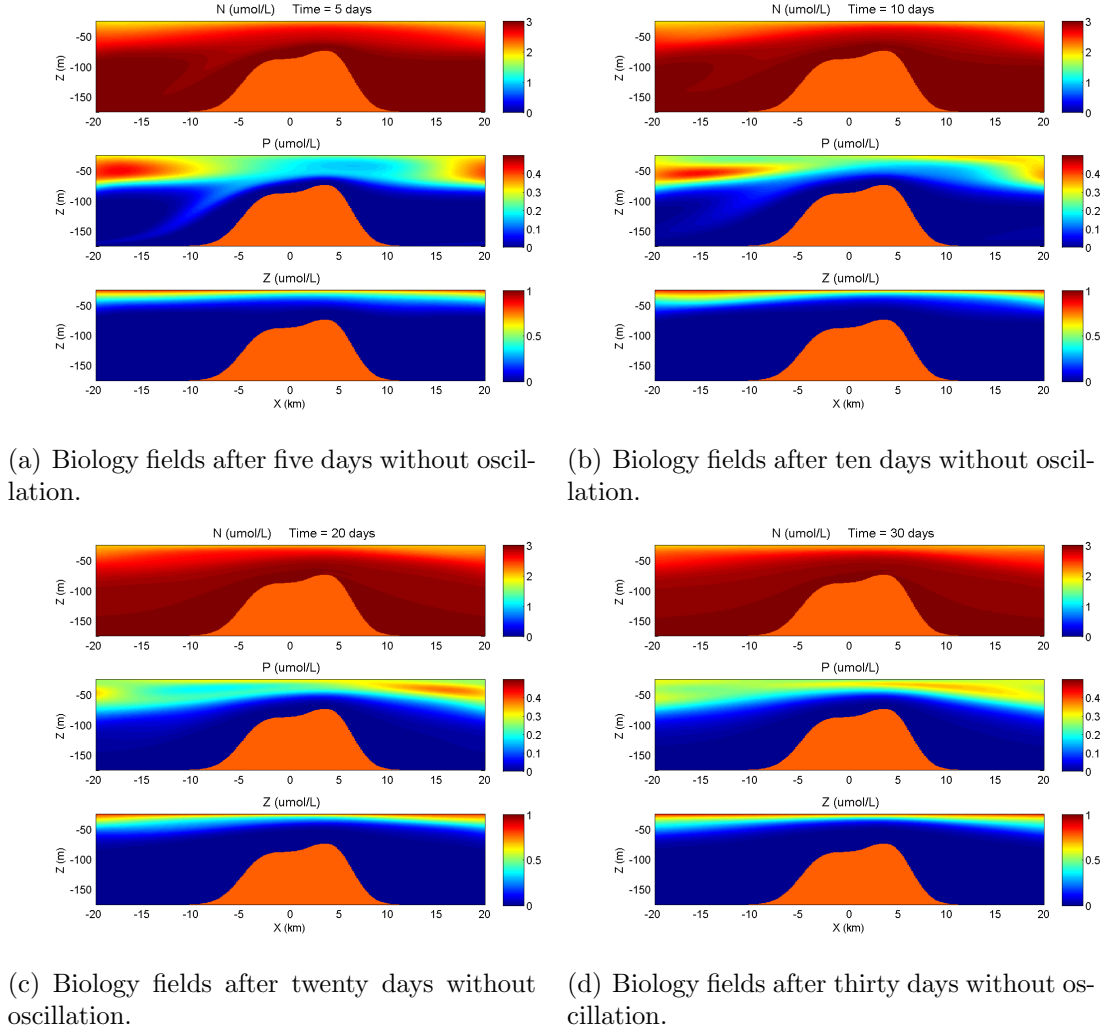remarkably similar, most likely because both are too fast to allow ample biological interaction.

(a) Biology fields after five days without oscillation.

(b) Biology fields after ten days without oscillation.

(c) Biology fields after twenty days without oscillation.

(d) Biology fields after thirty days without oscillation.

Figure 5-6: Case 1. No oscillations or diffusion, using parameters in Table 5.1. Phytoplankton blooms appear because of the vertical velocities caused by the bathymetry.

5.2 Three-dimensional Simulation

5.2.1 Problem Setup

Using three-dimensional bathymetry from Smith and Sandwell ([53]) and initialized fields of physical data, MSEAS solves for the corresponding velocity fields using output from a free surface simulation in the archipelago domain (Figure 1-2) for February
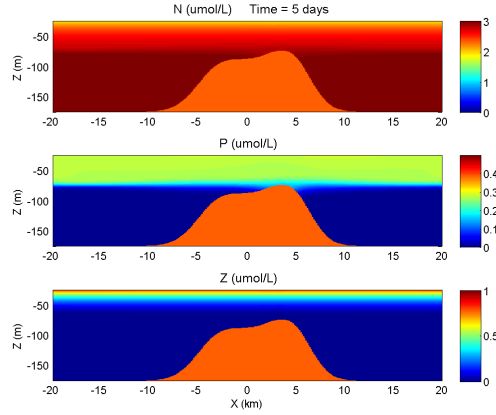
(a) Biology fields after five days with oscillation frequency of 2 cycles/day.
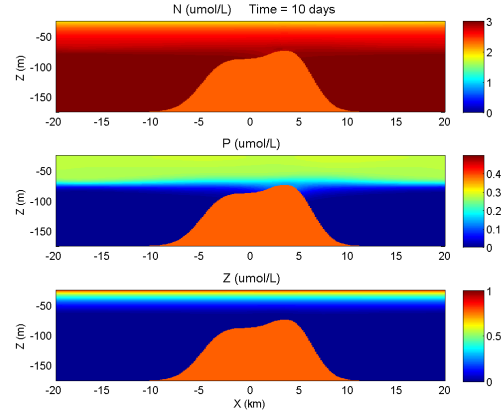
(b) Biology fields after ten days with oscillation frequency of 2 cycles/day.
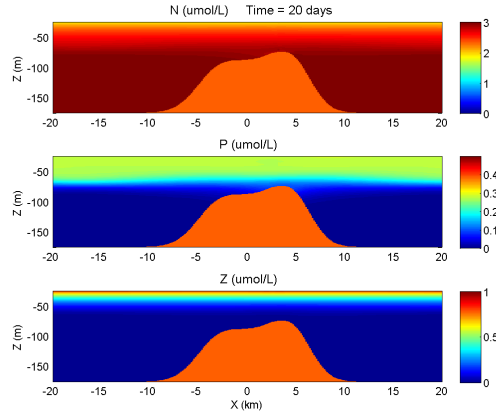
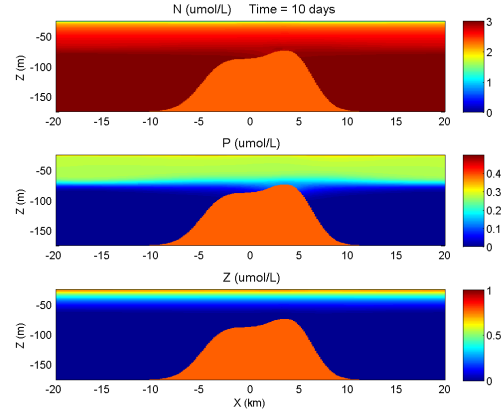(c) Biology fields after twenty days with oscillation frequency of 2 cycles/day.
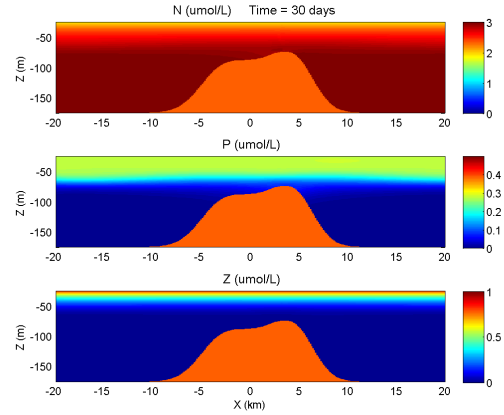
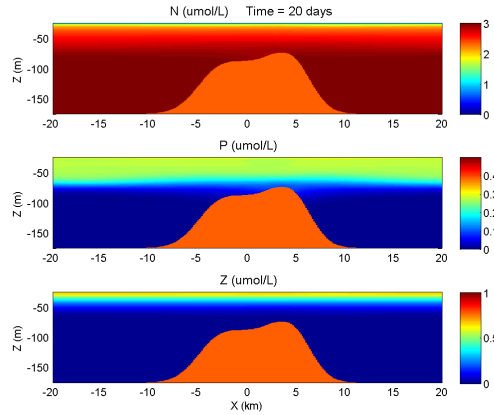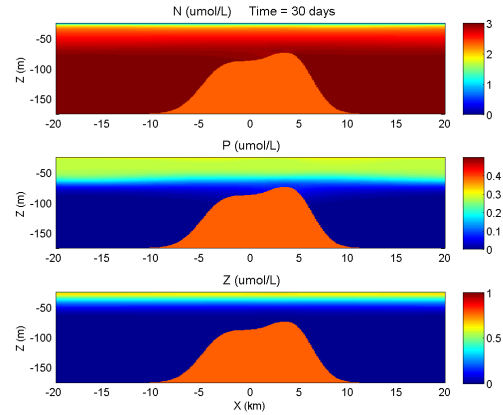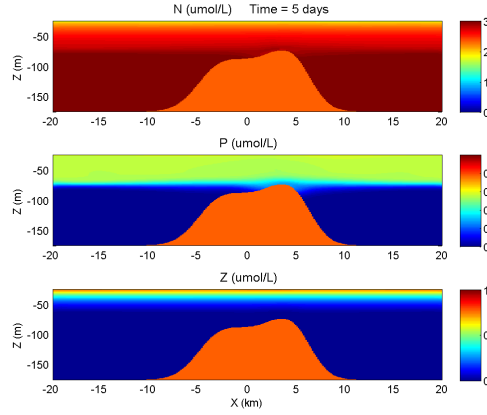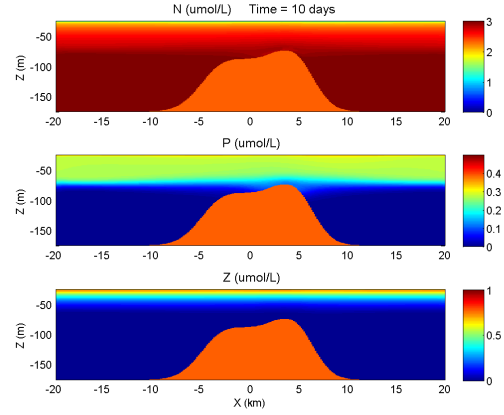(d) Biology fields after thirty days with oscillation frequency of 2 cycles/day.

Figure 5-7: Case 2. High frequency oscillations (2 cycles/day), corresponding to semidiurnal tidal constituents, without diffusion using parameters in Table 5.1. Increased biological activity seen in Case 1 is not present and the system has less variation than the similar case without biology (Figure 5-14).
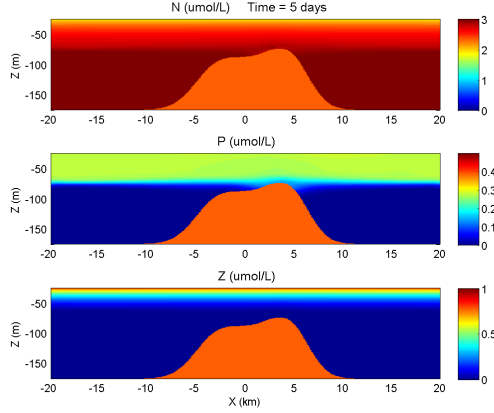
(a) Biology fields after five days with oscillation frequency of 1 cycle/day.
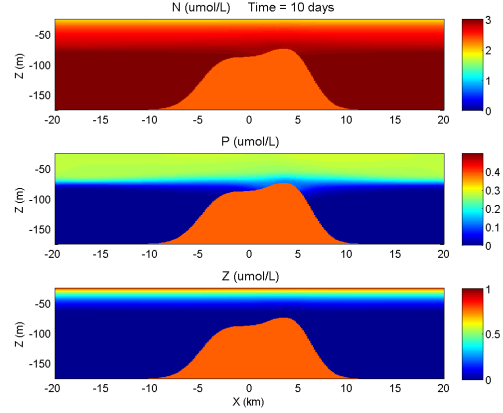
(b) Biology fields after ten days with oscillation frequency of 1 cycle/day.
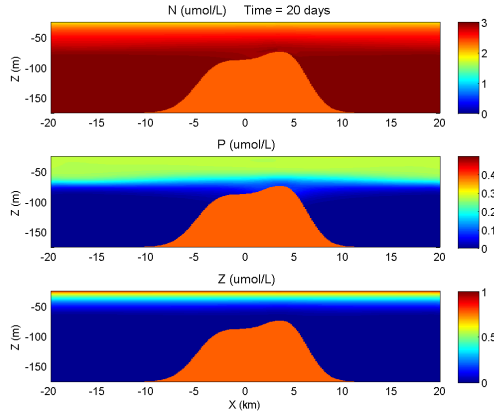
(c) Biology fields after twenty days with oscillation frequency of 1 cycle/day.
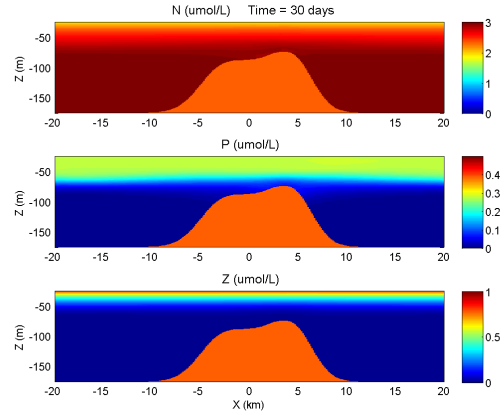
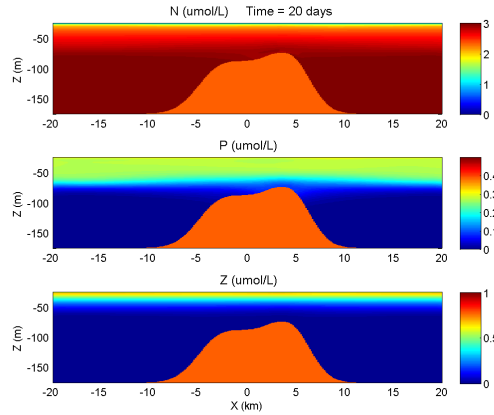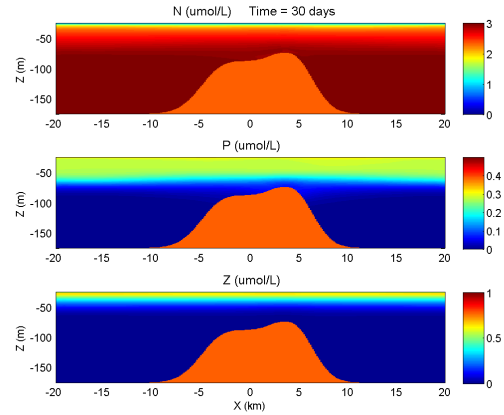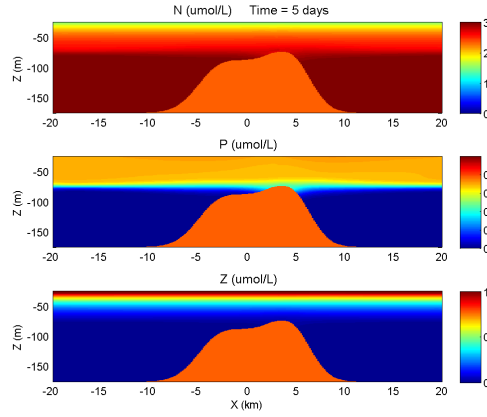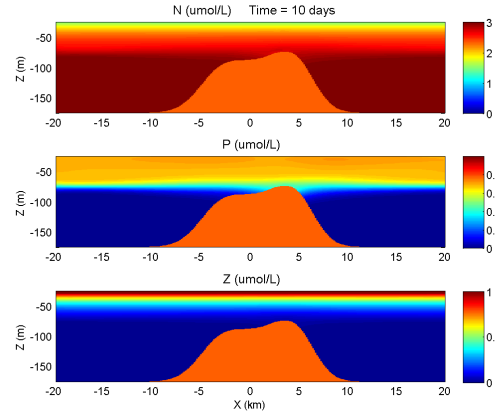(d) Biology fields after thirty days with oscillation frequency of 1 cycle/day.

Figure 5-8: Case 3. Low frequency oscillations (1 cycle/day), corresponding to diurnal tidal constituents, without diffusion using parameters in Table 5.1. Increased biological activity similar to Case 1 is still not present and the system has less variation than the similar case without biology (Figure 5-15).
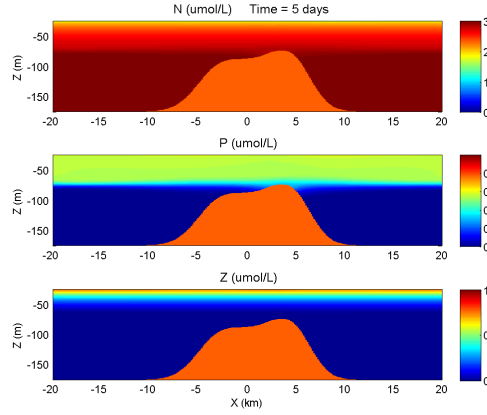
(a) Biology fields after five days with oscilla-
tion frequency of 2 cycles/day.

(b) Biology fields after ten days with oscilla-
tion frequency of 2 cycles/day.

(c) Biology fields after twenty days with oscil-
lation frequency of 2 cycles/day.

(d) Biology fields after thirty days with oscil-
lation frequency of 2 cycles/day.

Figure 5-9: Case 4. High frequency oscillations (2 cycles/day), corresponding to
semidiurnal tidal constituents, with diffusion using parameters from Table 5.1 leads
to more mixing than Case 2.

(a) Biology fields after five days with oscillation frequency of 1 cycle/day.

(b) Biology fields after ten days with oscillation frequency of 1 cycle/day.

(c) Biology fields after twenty days with oscillation frequency of 1 cycle/day.

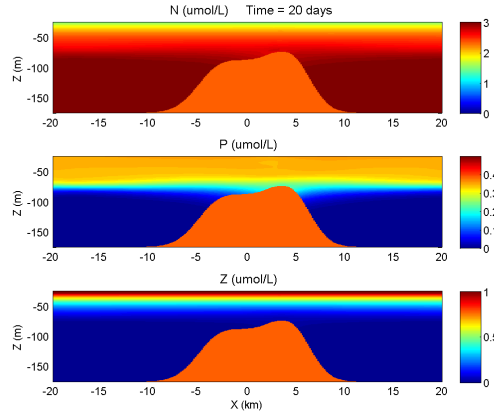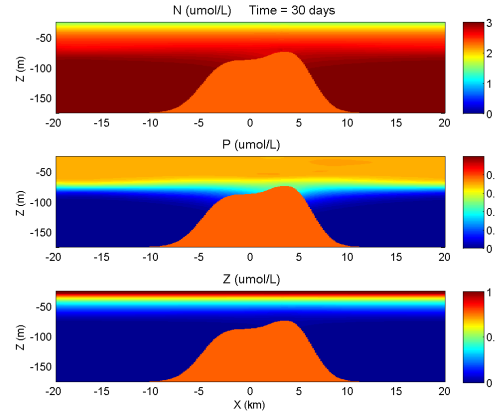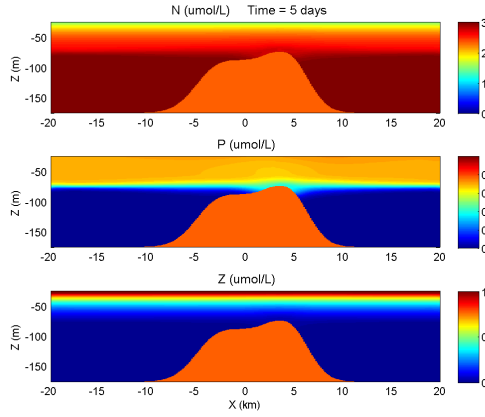(d) Biology fields after thirty days with oscillation frequency of 1 cycle/day.

Figure 5-10: Case 5. Low frequency oscillations (1 cycle/day), corresponding to diurnal tidal constituents, with diffusion using parameters from Table 5.1 leads to more mixing than Case 3.

(a) Biology fields after five days with oscillation frequency of 2 cycles/day.

(b) Biology fields after ten days with oscillation frequency of 2 cycles/day.

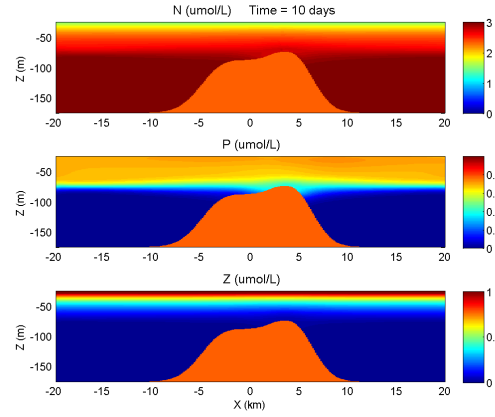(c) Biology fields after twenty days with oscillation frequency of 2 cycles/day.

(d) Biology fields after thirty days with oscillation frequency of 2 cycles/day.
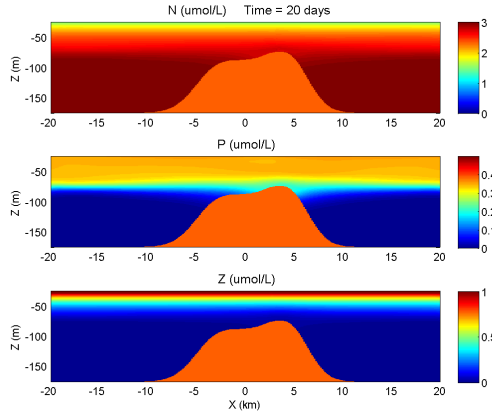
Figure 5-11: Case 6. High frequency oscillations (2 cycles/day), corresponding to semidiurnal tidal constituents, without diffusion using parameters matching the three-dimensional case.
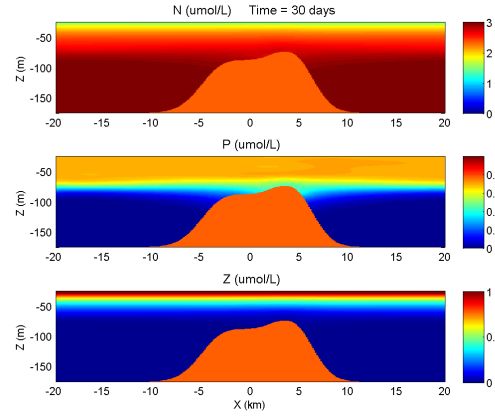
(a) Biology fields after five days with oscillation frequency of 1 cycle/day.

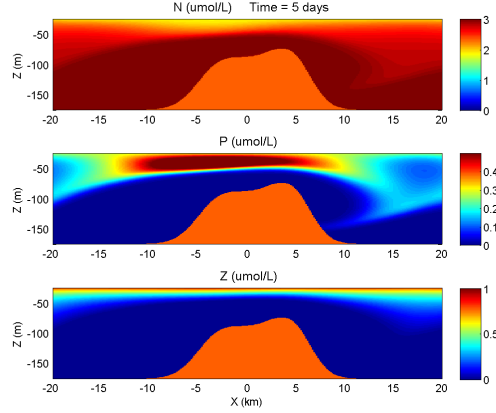(b) Biology fields after ten days with oscillation frequency of 1 cycle/day.

(c) Biology fields after twenty days with oscillation frequency of 1 cycle/day.
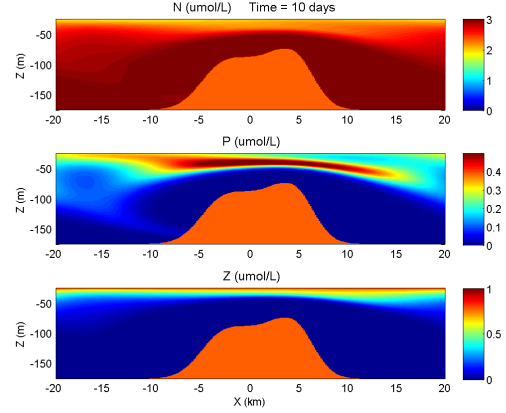
(d) Biology fields after thirty days with oscillation frequency of 1 cycle/day.

Figure 5-12: Case 7. Low frequency oscillations (1 cycle/day), corresponding to diurnal tidal constituents, without diffusion using parameters matching the three-dimensional case.
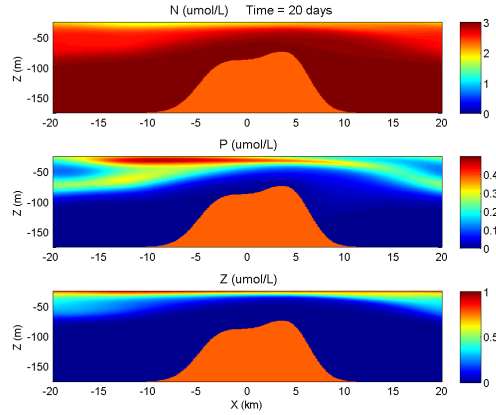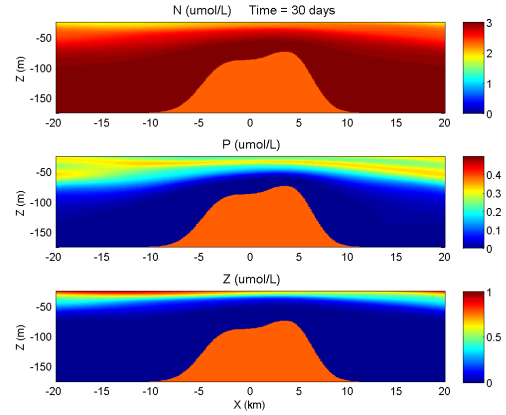
(a) Biology fields after five days with oscillation frequency of 0.1 cycles/day.

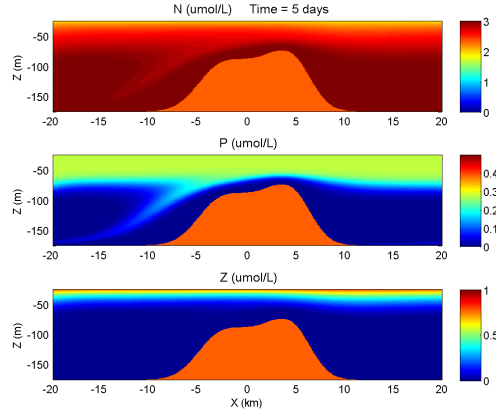(b) Biology fields after ten days with oscillation frequency of 0.1 cycles/day.

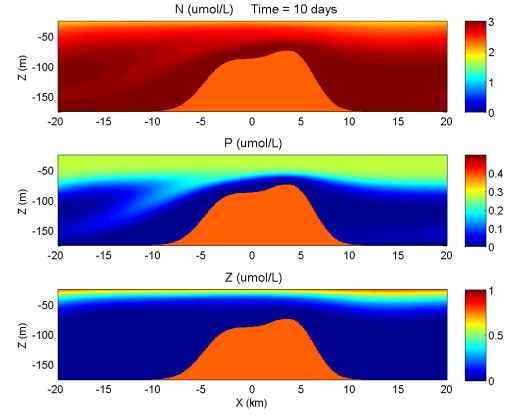(c) Biology fields after twenty days with oscillation frequency of 0.1 cycles/day.

(d) Biology fields after thirty days with oscillation frequency of 0.1 cycles/day.

Figure 5-13: Case 8. Very low frequency oscillations (0.1 cycles/day), corresponding to the longer tidal constituents, without diffusion using parameters from Table 5.1. Increased biological activity is seen, as tidal period is similar to the biological time scale.
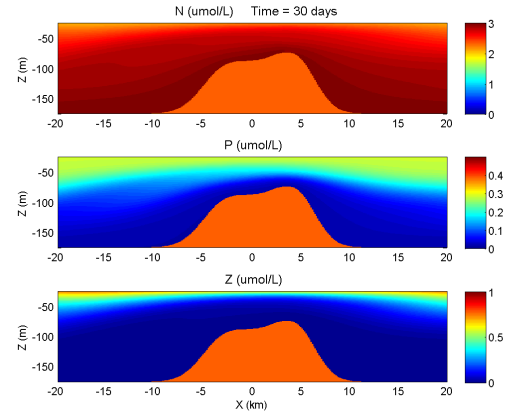
(a) Biology fields after five days without oscillation.

(b) Biology fields after ten days without oscillation.
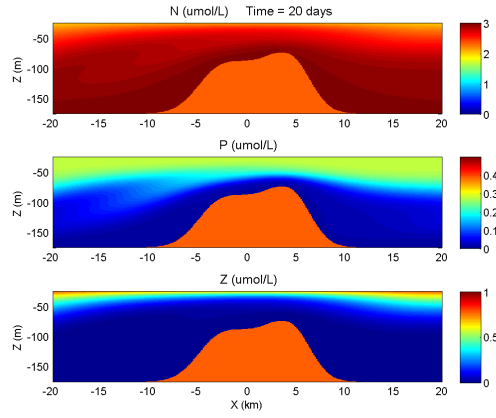
(c) Biology fields after twenty days without oscillation.

(d) Biology fields after thirty days without oscillation.

Figure 5-14: Case 9. Non-oscillatory flow without diffusion or biological reaction.
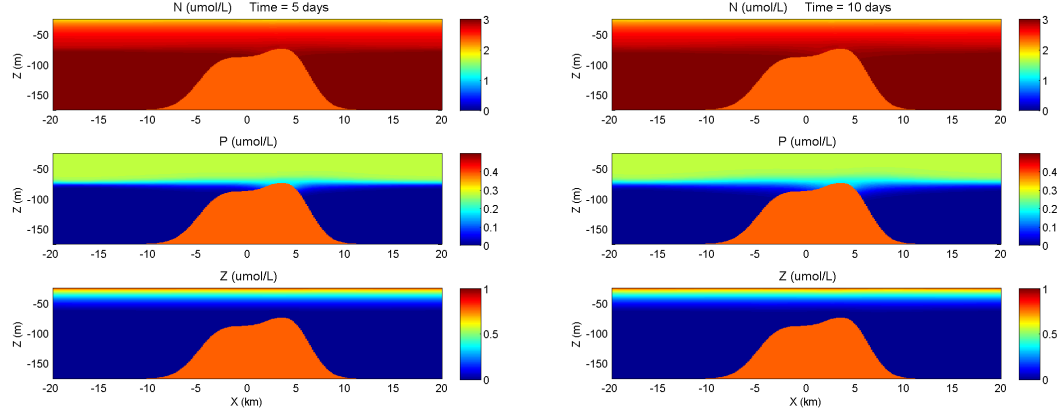
(a) Biology fields after five days with oscilla-
tion frequency of 2 cycles/day.

(b) Biology fields after ten days with oscilla-
tion frequency of 2 cycles/day.
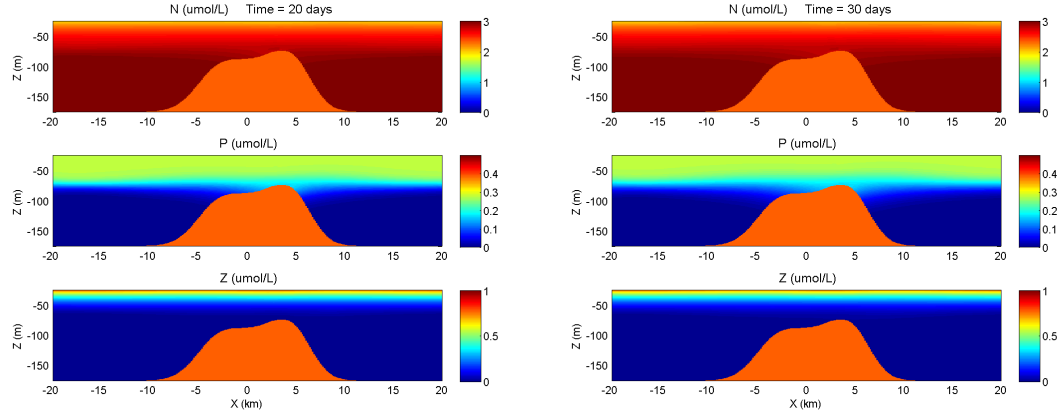
(c) Biology fields after twenty days with oscil-
lation frequency of 2 cycles/day.

(d) Biology fields after thirty days with oscil-
lation frequency of 2 cycles/day.

Figure 5-15: Case 10. High frequency oscillations (2 cycles/day), corresponding to
semidiurnal tidal constituents, without diffusion or biological reaction.

(a) Biology fields after five days with oscillation frequency of 1 cycle/day.

(b) Biology fields after ten days with oscillation frequency of 1 cycle/day.

(c) Biology fields after twenty days with oscillation frequency of 1 cycle/day.

(d) Biology fields after thirty days with oscillation frequency of 1 cycle/day.

Figure 5-16: Case 11. Low frequency oscillations (1 cycle/day), corresponding to diurnal tidal constituents, without diffusion or biological reaction.

(a) Biology fields after five days with oscillation frequency of 2 cycles/day.
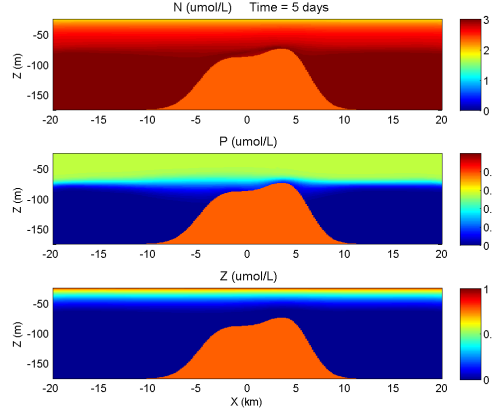
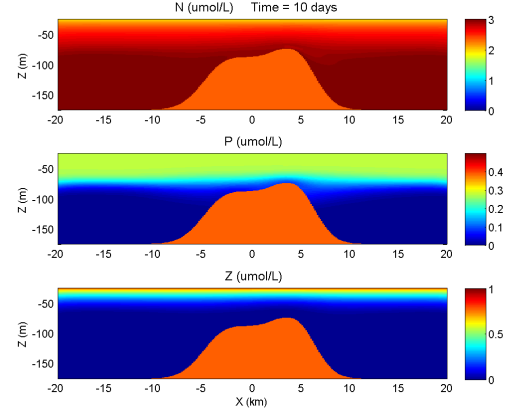(b) Biology fields after ten days with oscillation frequency of 2 cycles/day.

(c) Biology fields after twenty days with oscillation frequency of 2 cycles/day.

(d) Biology fields after thirty days with oscillation frequency of 2 cycles/day.
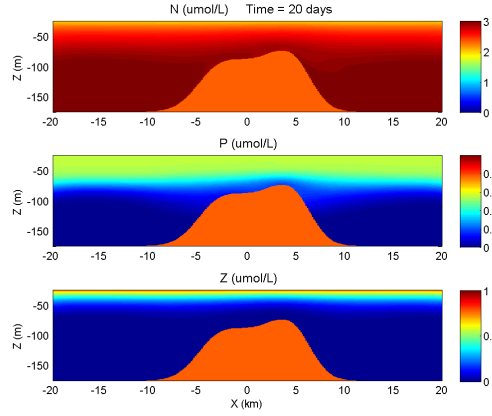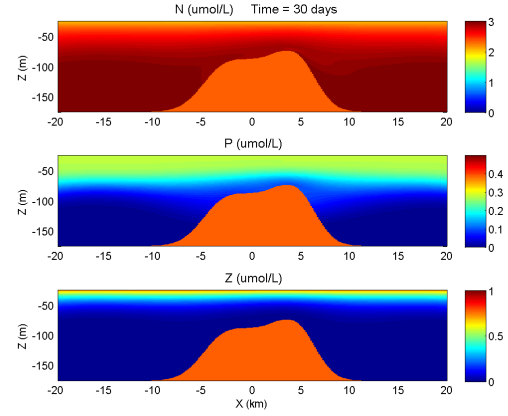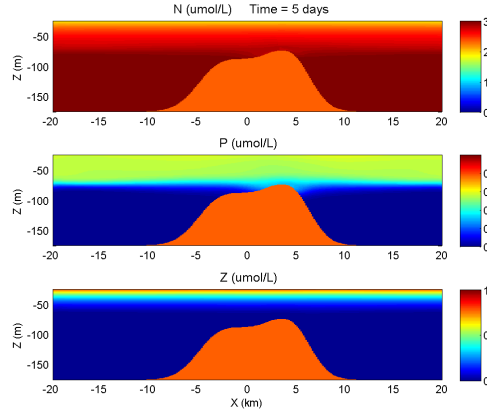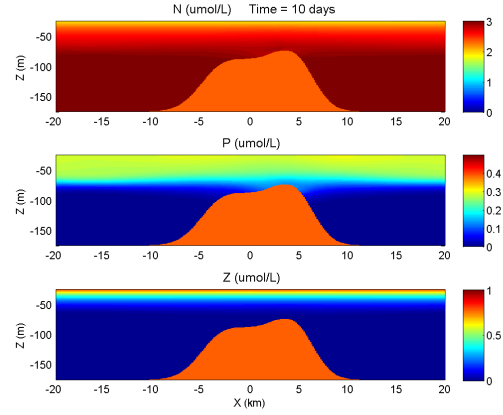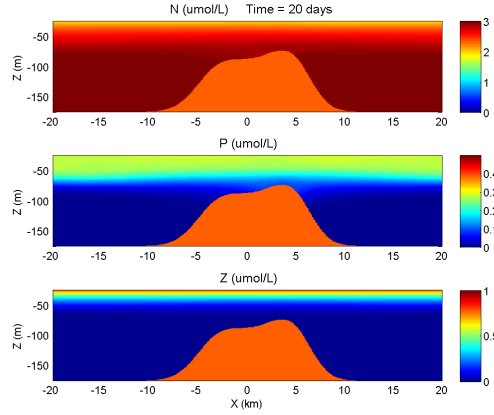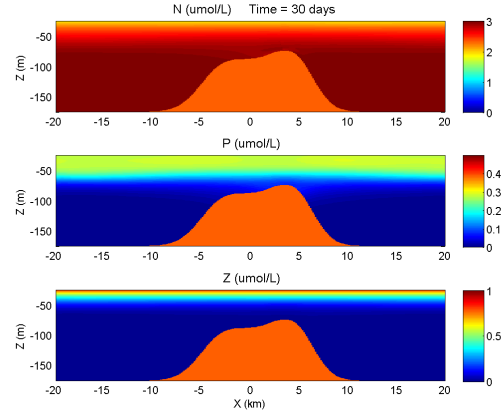
Figure 5-17: Case 12. High frequency oscillations (2 cycles/day), corresponding to longer tidal constituents, without diffusion using parameters from Table 5.1. This case has *double* the velocity of previous cases.

and March 2009. The simulation is forced with combination of wind stress from the Coupled Ocean/Atmosphere Mesoscale Prediction System (COAMPS, developed by the Naval Research Laboratory) and heat flux and Eliassen–Palm (E–P) flux from the U.S. Navy Operational Global Atmospheric Prediction System (NOGAPS) model. Large-scale open boundary conditions are weakly forced by the Hybrid Coordinate Ocean Model (HYCOM) fields. All simulations are forced with Generalized Inverse High-Resolution Barotropic Tides [38]. Remotely-sensed sea surface height anomalies and sea surface temperature are the only synoptic data utilized for initialization and assimilation, as no hydrographic data are currently available. To include biology, we initialized the biological fields in MSEAS to enable analysis of coupled physics and biology in the Philippine Archipelago as part of the *PhilEx* program. The details of this process and the resulting solutions are discussed in this section.

5.2.2 Biology Initialization

After simulations for physics in the Philippine Archipelago were sufficiently tuned, coupled physics-biology model simulation studies and forecasts were initiated, prompting the need for initial conditions for the biological variables used in the model. The Dusenberry-Lermusiaux biological model [6], discussed in Chapter 2, is used to model the advection, diffusion, and reaction of six state variables: chlorophyll, nitrate, ammonium, detritus, phytoplankton and zooplankton. Thus, we need three-dimensional fields of each of these variables to initialize the model. Our new methodology to do so is described next.

A combination of biogeochemical, climatological, satellite, and historical data was used for initialization, as data is extremely limited in the Philippines. We gathered MODIS weekly calibrated satellite images of chlorophyll-a concentration for February and March 2009 as ASCII files from OceanWatch [44]. This satellite data was mapped onto the modeling grid also used for physics. Cloud cover prevented complete coverage in the region, so the first two weeks of February were combined by averaging any point present in both the weeks and taking the value of whichever point is present otherwise. Even when two weeks of data were merged, full coverage was still not achieved, so the

field was smoothly interpolated to give full coverage [24]. This completed the initial surface field for the euphotic-zone integrated chlorophyll for February. We applied the same techniques to the MODIS satellite data for the last week of February and the first week of March to obtain the initialized integrated surface chlorophyll field for March.
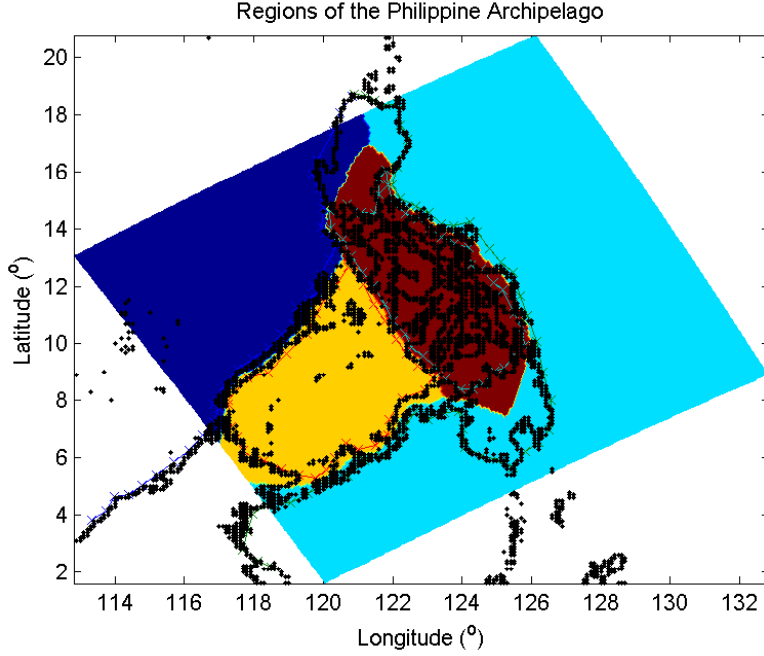
Figure 5-18: Regions of the Philippine Archipelago with different chlorophyll profiles. Dark blue represents the South China Sea, yellow is the Sulu Sea, cyan is the Pacific, and red represents the interior seas.

To create a three-dimensional field from the surface chlorophyll, we divided the domain into regions (Figure 5-18) which are distinctive biologically and created a generic profile for each (Figure 5-19). These profiles are based on experimental data [10]. We modeled them as a combination of two "shifted" Gaussian-like curves (Equation 5.2).

$$B(z_u) = B_o + \frac{a}{\sigma_u \sqrt{2\pi}} e^{-\frac{(z_u - z_m)^2}{2\sigma_u^2}}$$

$$B(z_l) = B_o + \frac{a}{\sigma_u \sqrt{2\pi}} e^{-\frac{(z_l - z_m)^2}{2\sigma_l^2}}$$

(5.2)

where $B(z_u)$ is the profile above the deep chlorophyll maximum, $B(z_l)$ is the profile

below the deep chlorophyll maximum, B_o is the background value, σ_u is the standard deviation of the upper profile, σ_l determines the spread of the lower profile, a determines the peak value and z_m is the depth of the deep chlorophyll maximum. Note that the two profiles meet and are continuous at z_m. We then fit (scaled) these analytical profiles (Equation 5.2) at each point so that the integrated chlorophyll value (from the merged satellite data) matched the value of the integrated profile. Figure 5-19 shows three generic profiles for three different regions in the Philippines. The *deep chlorophyll maximum* is highest for the Visayan Sea and other interior seas and lowest for the Pacific Ocean.
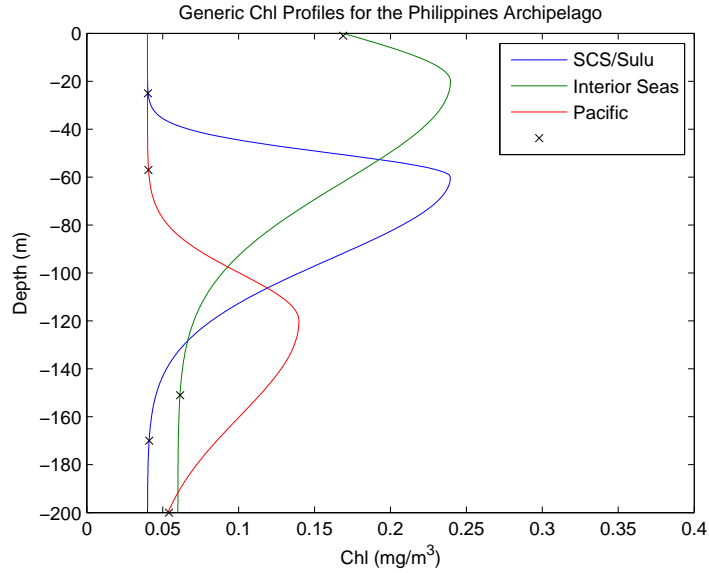
Figure 5-19: Example of generic profiles for chlorophyll were scaled according to the surface integrated chlorophyll value from satellite images. xs distinguish peaks from the background value.

We then generated initial fields of nitrate (NO_3^-) by using Objective Analysis (OA) methods to obtain profiles from climatology data (horizontal fields in 1° resolution for specified depth levels) from World Ocean Atlas [1] for February and March. For future simulations, we will use a novel Objective Analysis approach [3] based on the Fast Marching Method, which accounts for the coastline constraints by using the optimal path length (minimum distance between two points without going across landforms), an important consideration for a domain with several islands and complex coastlines,

such as the Philippine Archipelago. OA can be used for any variable, for example, an OA field of chlorophyll using the Fast Marching Method is presented in Figure 5-20.
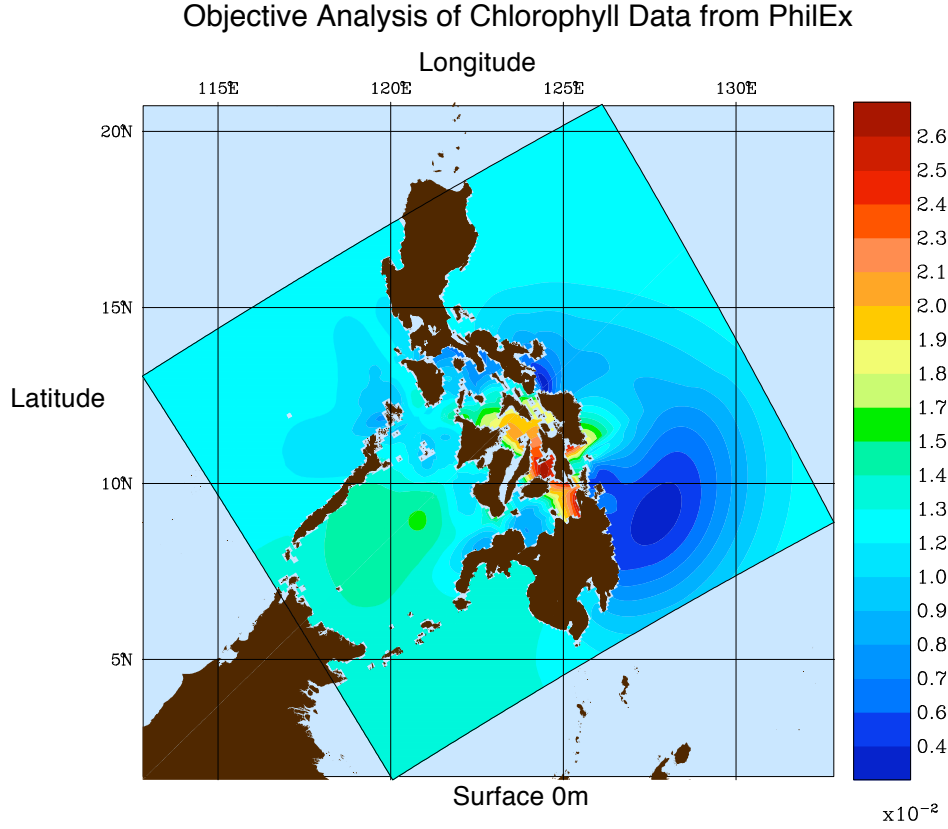
Figure 5-20: Objectively analyzed chlorophyll field from the *PhilEx* IOP09 cruise data using the Fast Marching Method. The scales used in the OA are: synoptic decay–90km, mean decay–360km, synoptic zero crossing–270km, mean zero crossing–1080km.

In collaboration with the MSEAS group, we then created initial ammonium (NH_4^+) and zooplankton fields by obtaining a first guess for NH_4^+ by setting the NO_3^- reaction terms to zero and two first guesses for zooplankton, one by setting the zooplankton terms to zero and the other by setting the phytoplankton reaction terms to zero [24], [34]. The minimum of the result of the phytoplankton reaction equation and 1.15 times the result from the zooplankton reaction equation are then used to assign an updated estimate of zooplankton. Ammonium is computed again by setting the NH_4^+ reaction equation to zero and taking the minimum of this result times 1.15 and the

Light attenuation parameters	k_w=0.0375
	$k_c = 0.028$
Photosynthesis parameters	P_m=1.4e-3 mgC(mgChl)$^{-1}s^{-1}$
(assuming C:Chl = 40)	α=3.00e-5 mgC(mgChl)$^{-1}$s^{-1}(μmol photons m^{-2}s^{-1})$^{-1}$
P-uptake of nutrients	$k_{NH_4^+}$=0.06 Half-saturation for NH4 uptake
Zooplankton grazing	R_m=0.83 Max grazing rate
	λ=0.42 Ivlev's constant
Ammonium to NO_3^-	k_N=0.2 Nitrification timescale (day$^-$1)

Table 5.3: Parameters used in the four-dimensional biological-physical simulations for the *PhilEx* real-time IOP09 experiment.

original estimate of ammonium. The iteration process is then repeated a few times, starting with the first estimates for zooplankton.

We initialized phytoplankton by assuming a direct proportionality to chlorophyll, accounting for unit conversion. Lastly, detritus fields were produced by balancing the source and reaction terms associated with this state variables.

In setting the reaction equations to zero, a daily mean solar radiation value was computed at each point (including phytoplankton self-shading) assuming a peak solar radiation value of 600 $\frac{W}{m^2}$ (an approximate average of the peak values in the domain including clouds).

Parameters for the biological model were from [6] or motivated by observations in the region. The parameters in Table 5.3 were also specifically chosen to yield O(1) initial values and allow for deeper chlorophyll maxima than in [6]. This MSEAS methodology for initialization of biological fields leads to initial fields and parameters that are dynamically adjusted. No spurious and large "biological adjustment" occurs at the start of the simulations.

It is important to note that this is a first step in initializing biology for the Philippines. As more biological data and information is gathered, we expect to use better parameters, improve our understanding of relationships between the state variables, and increase the accuracy of the model. The methods presented here are very general and can be applied to any region with sparse data. Using only satellite data (available for any region), climatological data and data from literature, we initialized biology

fields for six state variables.

5.2.3   Results

The ocean field estimates from MSEAS show increased activity above bathymetric features. For our purposes, we will focus on the San Bernardino Strait. Plots of nitrate, phytoplankton, and zooplankton estimates along a cross-section of the San Bernardino Strait (along 12.13ºN, 123.98ºE to 13.33ºN, 124.66ºE) are presented in Figure 5-21. From February 2, 2009 to March 5, 2009, plots were analyzed for noon and midnight of each day. From these, we see that nitrate consistently has higher values across and above the strait under $50m$ (Figure 5-21(a)), with higher concentration tongues sometimes appearing over the sloped bathymetry, as in Figure 5-21(b). Phytoplankton always had maximum values above the bathymetry (Figure 5-21(c)), which sometimes extended toward the Pacific Ocean (Figure 5-21(d)). Zooplankton had similar behavior, with consistent maximum values above the bathymetry (Figure 5-21(e)) that sometimes extended further northeast (Figure 5-21(f)). Other state variables were similar qualitatively to those presented here.

## 5.3   Discussion and Future Work

The results from the two-dimensional and three-dimensional cases are very difficult to compare, even qualitatively, because of the varying levels of complexity between the two. Case 8, which has a much longer tidal period than other cases, is the most similar to the three-dimensional results, with increased biological activity focused over the bathymetry sometimes extending towards the Pacific Ocean. Cases 2 through 7 of the two-dimensional model are not very similar to the three-dimensional results, which may indicate that the lower frequencies dominate the biological activity. However, these differences could also be attributed to having different flow fields (two-dimensional versus three-dimensional), bathymetries, and initial conditions. The two-dimensional results did clearly show that long physical time scales, compared to
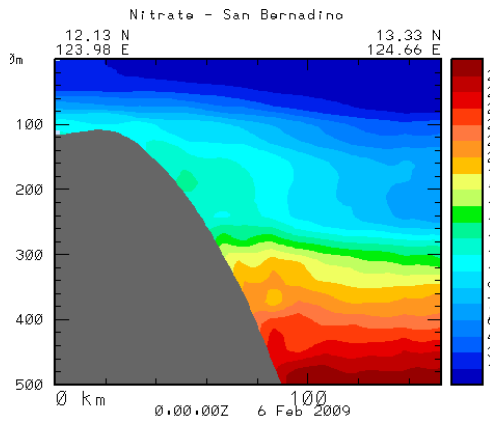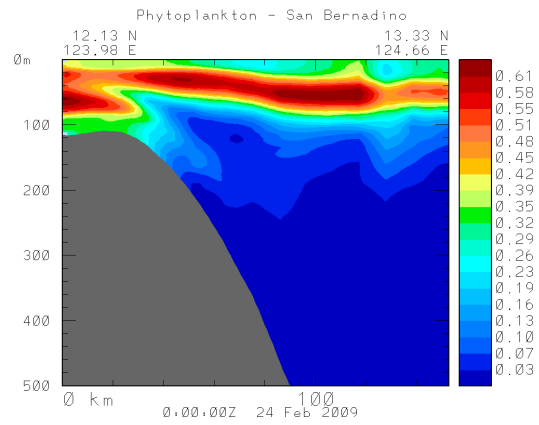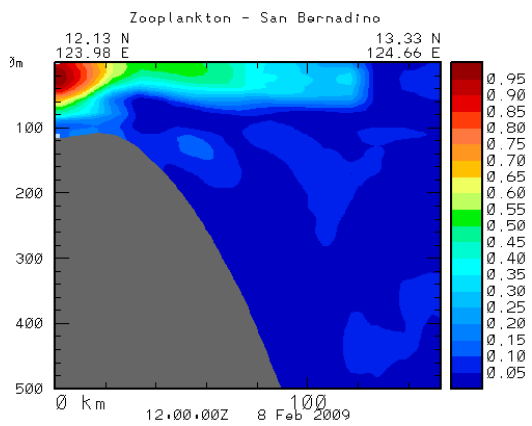
(a) Nitrate for February 6, 2009.
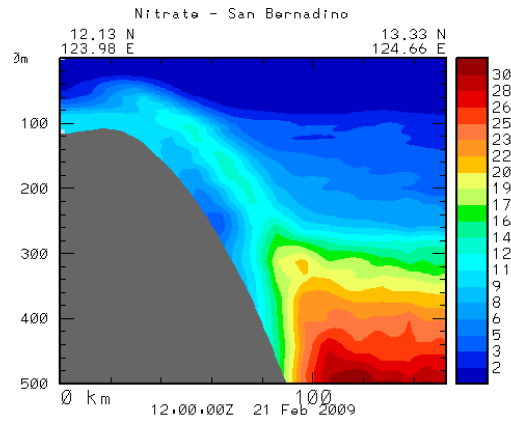
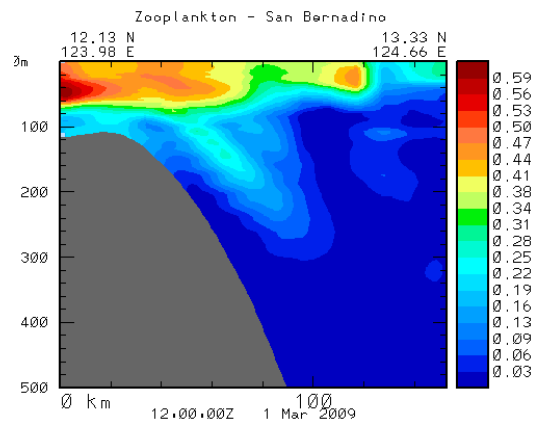(b) Nitrate for February 21, 2009.
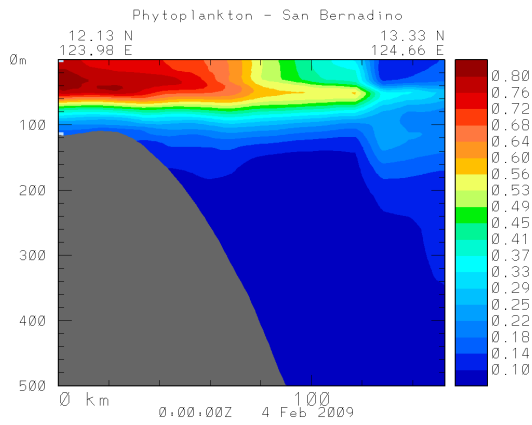
(c) Phytoplankton for February 4, 2009.

(d) Phytoplankton for February 24, 2009.

(e) Zooplankton for February 8, 2009.

(f) Zooplankton for March 1, 2009.

Figure 5-21: Results from MSEAS for the San Bernardino Strait.

the biological reaction time scales, allowed more biological activity throughout the water column.

Additionally, a new method for initializing the biological fields was developed and utilized. With region-specific chlorophyll profiles, the three-dimensional chlorophyll field developed from satellite data accounted for regional differences, which can be vast for a domain like the Philippine Archipelago.

For future work, an averaged velocity field from MSEAS could be used in the two-dimensional simulation for better comparison. Additionally, the initialized fields could be matched more closely. A noticeable difference seems to be the critical depth (where phytoplankton receives enough light to grow); it is much lower in the three-dimensional model. For the two-dimensional case, it would be interesting to investigate cases which combine several different tidal frequencies. These results would likely be dominated by the lowest frequency, which allow the furthest vertical transport. When nutrient-rich water is able to reach shallow depths where nutrients have been depleted, increased biological activity and blooms are likely because of the increase in food sources.

Chapter 6

Conclusion

In this thesis, we presented research toward understanding coupled physics-biology processes in ocean straits. We performed new analytical studies and higher-order simulations of idealized dynamics that are relevant to generic biology in straits and applied them to the San Bernardino Strait in the Philippine Archipelago with tidal forcing.

In Chapter 2, we motivated our research, discussing the importance of understanding coupled physics and biology interactions and the sparsity of data, especially in the Philippine domain. Further, we completed an overview of lower trophic level biological models in the ocean, including the Nutrient-Phytoplankton-Zooplankton (NPZ) model and a more complicated six state variable model. We also discussed the validity of NPZ models, explained the reaction terms, and compared different ways of modeling biological reactions.

In Chapter 3, we performed novel global equilibrium and local stability analyses for the NPZ model in terms of system parameters with and without physics. This included finding and classifying equilibria states as stable or unstable, developing a new method of determining appropriate parameter values given some known parameter values, and specifying critical stability depths and regions where stability properties change. Phase portraits verified our predictions and simulations in the domain (including flow). They indicated that the stability analysis for the regime without physics gives a conservative range of appropriate parameter values, as advection, and

especially diffusion, act to stabilize the biological dynamics.

In Chapter 4, we developed, verified, and analyzed a two-dimensional physical-biological model. We presented and studied a novel numerical scheme to solve the NPZ equations for physical-biological modeling. The new scheme combines Arakawa C-grid with masking for easy implementation of boundary conditions, the operator splitting method for computational efficiency and the WENO scheme to avoid oscillations in advection-dominated flows. We showed that the WENO scheme was also less numerically diffusive and more computationally efficient than the donor-cell, hybrid, and classic central difference schemes. The central difference scheme produced oscillatory results when tracers accumulated at the boundary and was shown to be appropriate only for smooth problems. The results from the donor cell scheme were not oscillatory because enough numerical diffusion in the system smoothed the discontinuities. A hybrid scheme, which combines the donor-cell and central difference scheme, depended on a critical value to avoid oscillations, making it still more diffusive than WENO scheme and requiring tuning of a case-specific parameter. Additionally, the WENO scheme was more computationally efficient for comparable resolution, which is important when resolving biological features. A comparison to an independent simulation using Discontinuous Galerkin on an unstructured grid showed excellent agreement, suggesting that both schemes are accurate.

In Chapter 5, we applied the physics-biology model to a realistic representation of the San Bernardino Strait in the Philippine Archipelago under the influence of tidal forces and compared the results to a high fidelity three-dimensional model from MSEAS. First, we conducted new studies of the effect of tides on biology in a test case motivated by the San Bernardino Strait in both two and three dimensions. Different frequencies, parameters, and levels of diffusion were examined for the two-dimensional case. For the three-dimensional case, we proposed a new method of initializing biological variables for regions with sparse data, which includes objective analysis and region-specific profiles. Examining different frequencies of physical forcing (e.g. tides) in the two-dimensional case revealed that faster oscillations had less effect than slower oscillations. The time scale of this motion was too short (compared to the biological

time scales) to allow phytoplankton to bloom.

The results presented serve as preparation for future work. The two-dimensional idealized numerical simulation can be used to analyze interaction between physics and biology for many different straits and physical features, simply by implementing the appropriate parameters and flow field. The method to analyze the stability of the NPZ model should be performed to ensure effects seen are realistic results of the interactions between physics and biology. Additionally, the initialization of the biological fields for the three-dimensional model is very general and is useful for many regions and many different models.

More specifically, additional physical features in the San Bernardino Strait should be isolated and examined in both the two-dimensional and three-dimensional models to identify their effect on biology. As *PhilEx* continues, more biological data will be available and those results should be compared to the results from the computational models and used to improve future modeling of physical-biological interactions in the San Bernardino Strait.

Appendix A

Number of valid Z equilibrium based on ρ and s

The following figures hold N_T constant for $N_T = 2, 2.2$, and 3 $\mu mol/L$ (values in each of the different stability regions). For each N_T value, there is a figure showing s, ρ, and ρ^2 with β versus zooplankton concentration Z (these expressions are defined in Equation 3.4). Figures are shown for the entire depth range (in terms of β) and also focused on the depth region where the stability transitions occur.

Z	Region 1 $0 \leq \beta < \beta_{c1}$ $-\infty < z < z_{c1}$	Region 2 $\beta_{c1} < \beta < \beta_{c2}$ $z_{c1} < z < z_{c2}$	Region 3 $\beta_{c2} < \beta \leq u$ $z_{c2} < z \leq 0$
$0 < N_T < N_{Tc\rho}$	$s > 0$ $\rho < 0$ No solutions	$s < 0$ $\rho < 0$ One solution	$s < 0$ $\rho > 0$ One solution
$N_{Tc\rho} < N_T < N_{Tcs}$	$s < 0$ $\rho < 0$ One solution	$s < 0$ $\rho > 0$ One solution	$s < 0$ $\rho > 0$ One solution
$N_T > N_{Tcs}$	$s < 0$ $\rho > 0$ One solution	$s > 0$ $\rho > 0$ Two solutions	$s > 0$ $\rho > 0$ Two solutions

Table A.1: Number of zooplankton equilibrium based on total biomass (N_T), depth, and the sign of ρ and s. Figures included in this Appendix show that ρ and s can be plotted easily to determine the number of solutions for a given depth.
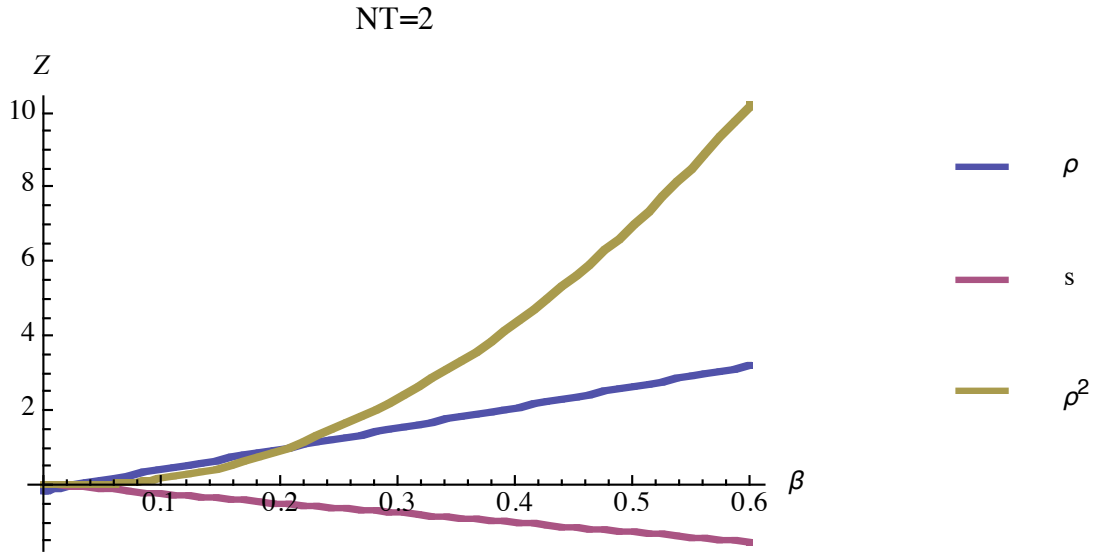
Figure A-1: ρ, s, and ρ^2 for $N_T = 2$ $\mu mol/L$ over entire depth range β. Transitions only occur for very small β (deep water), shown in Figure A-2.

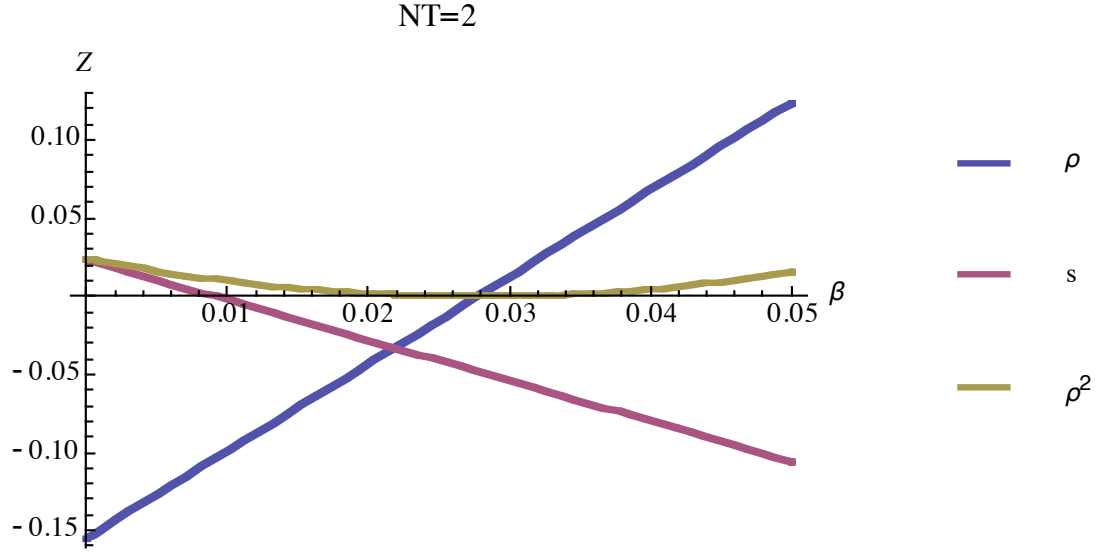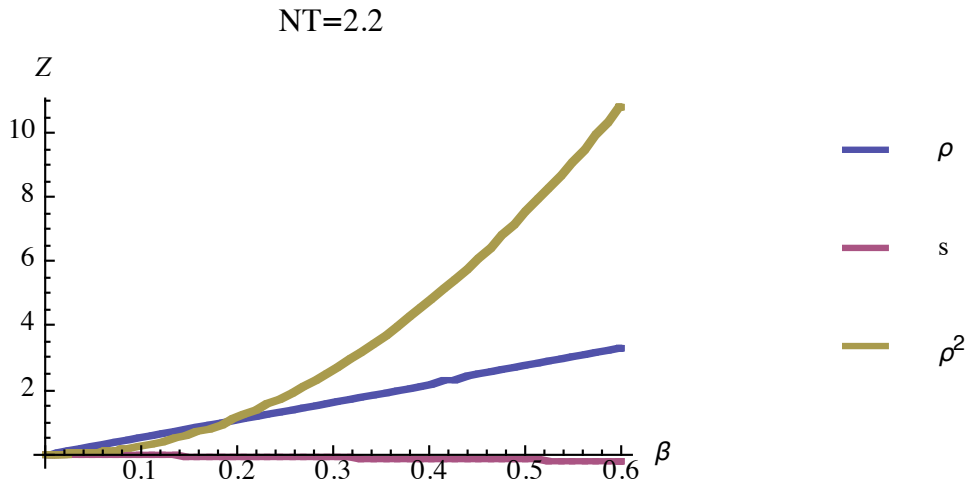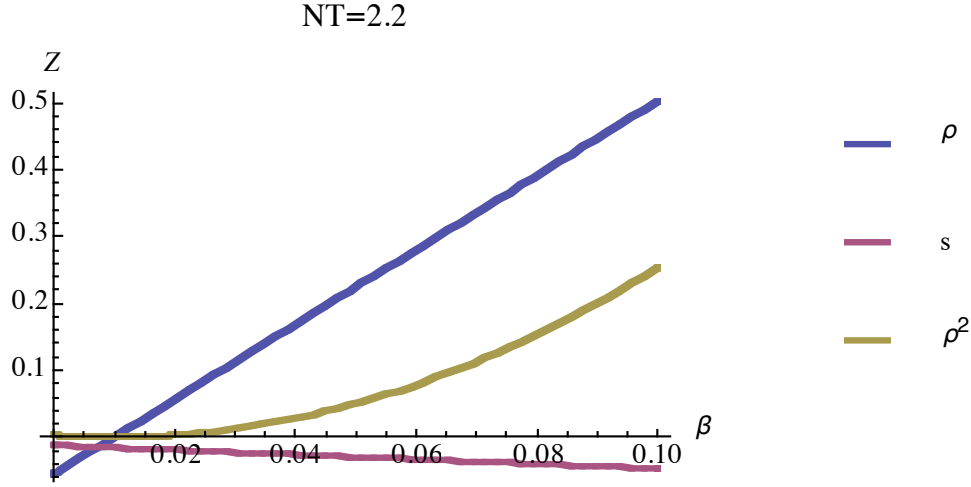Figure A-2: At $\beta = 0$, $\rho < 0$ and $s > 0$, so no solutions are present. After approximately $\beta = 0.01$, $s < 0$ and one solution appears. At about $\beta = 0.0275$, $\rho > 0$ and only one solution is still present. This corresponds to $N_T = 2$ $\mu mol/L$, which is the second row of Table A.1.
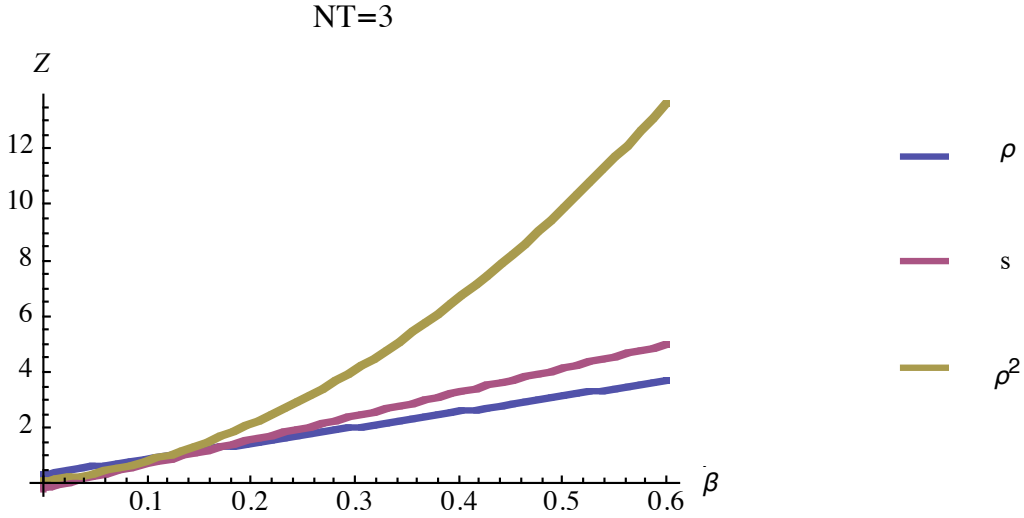

Figure A-3: ρ, s, and ρ^2 for $N_T = 2.2$ $\mu mol/L$ over entire depth range β. Transitions only occur for very small β (deep water), shown in Figure A-4.

Figure A-4: For all β, $s < 0$. For $\beta < 0.01$, $\rho < 0$ (one solution) and for $\beta > 0.01$, $\rho > 0$ (again, one solution). This corresponds to $N_T = 2.2 \; \mu mol/L$, which is the third row of Table A.1.

Figure A-5: ρ, s, and ρ^2 for $N_T = 3 \; \mu mol/L$ over entire depth range β. Transitions only occur for very small β (deep water), shown in Figure A-6.
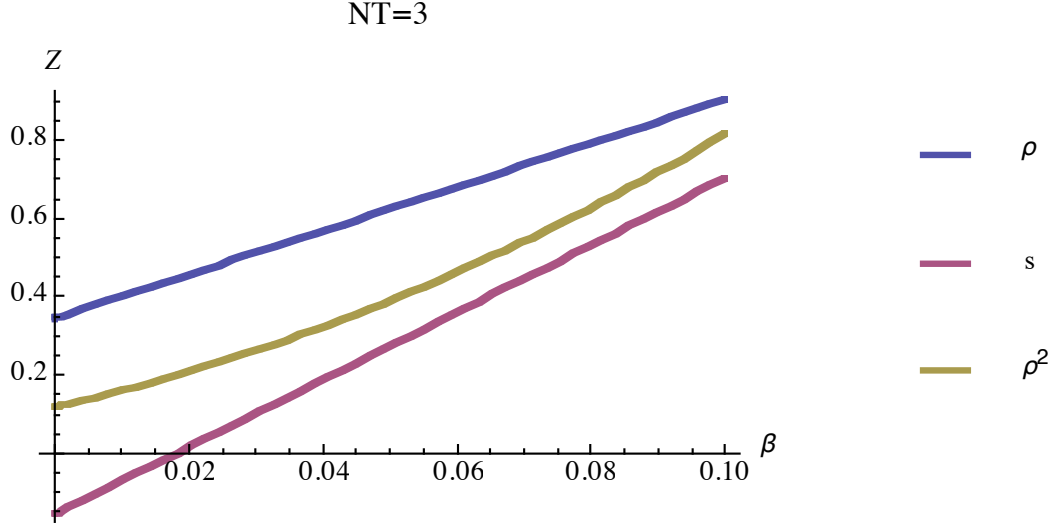
Figure A-6: For all β, $\rho > 0$. For $\beta < 0.02$, $s < 0$ (one solution) and for $\beta > 0.02$, $s > 0$ (two solutions). This corresponds to $N_T = 3 \; \mu mol/L$, which is the last row of Table A.1.
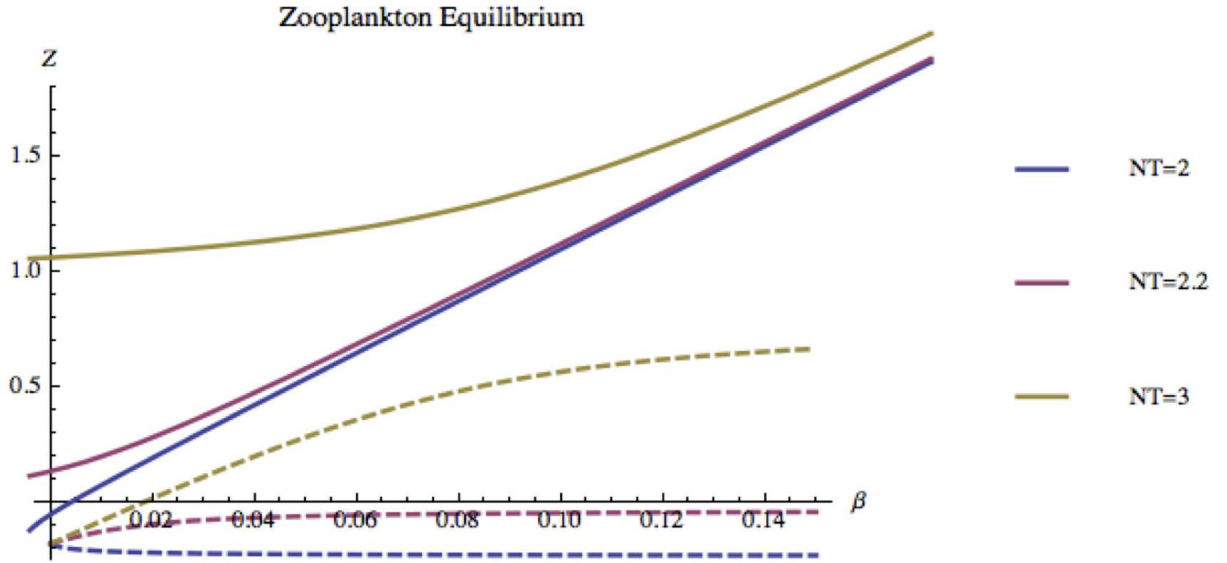

Figure A-7: Zooplankton equilibrium for various N_T values with the solid line representing the positive root of zooplankton and the dashed line representing the negative root. The number of physical solutions corresponds to the predictions made in the previous figures. For $N_T = 2 \; \mu mol/L$, we see that for very small β, there are no solutions, then the positive root becomes a physical solution for all β above a critical value. For $N_T = 2.2 \; \mu mol/L$, we always have one solution and for $N_T = 3 \; \mu mol/L$, we have one solution for small β, then two solutions as β grows.
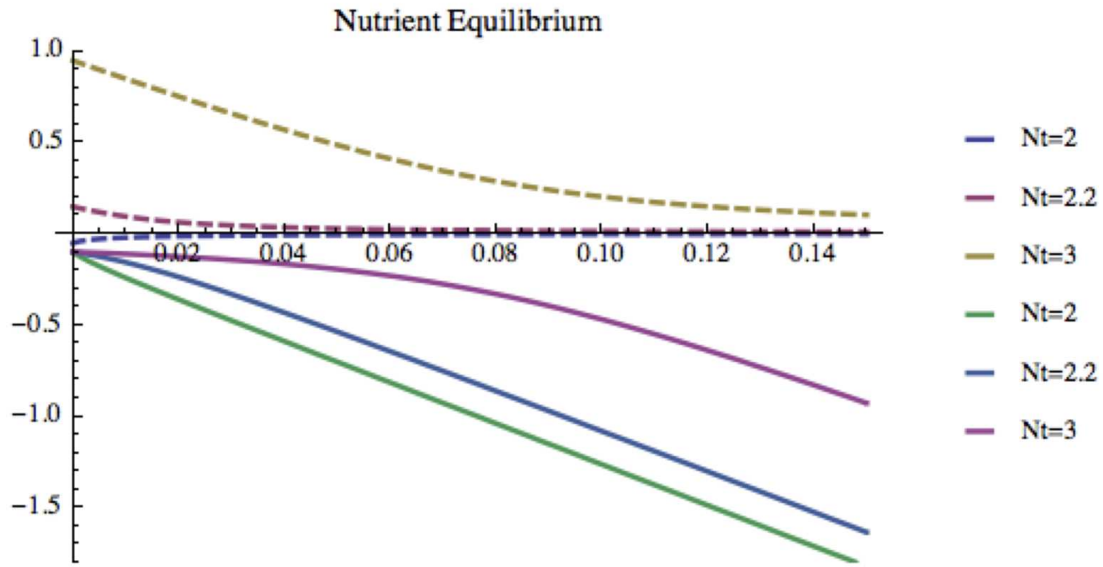
Figure A-8: Nutrient equilibrium for various N_T values with the solid line representing the positive root of nutrient and the dashed line representing the negative root. The number of physical solutions corresponds to the predications made in the previous figures. For $N_T = 2 \ \mu mol/L$, we see that for very small β, there are no solutions, then the negative root becomes a physical solution for all β above a critical value. For $N_T = 2.2 \ \mu mol/L$, we always have one solution and for $N_T = 3 \ \mu mol/L$, we have one solution all β.
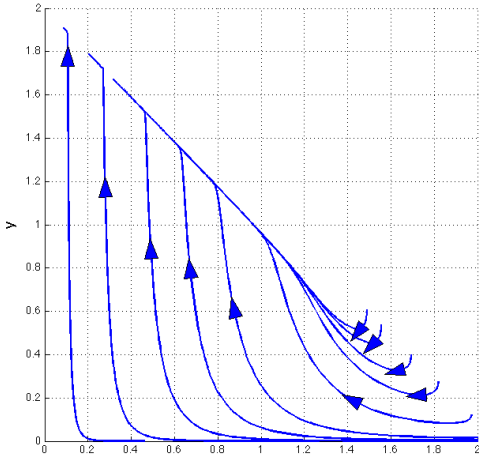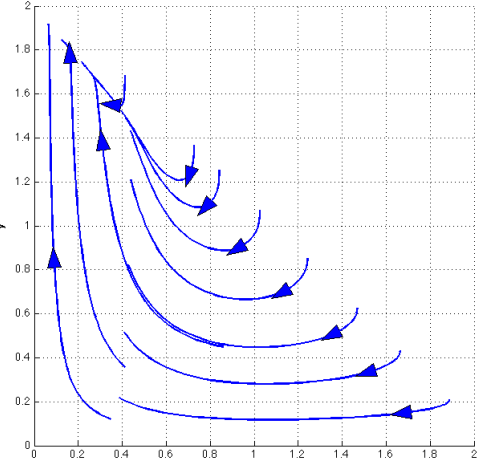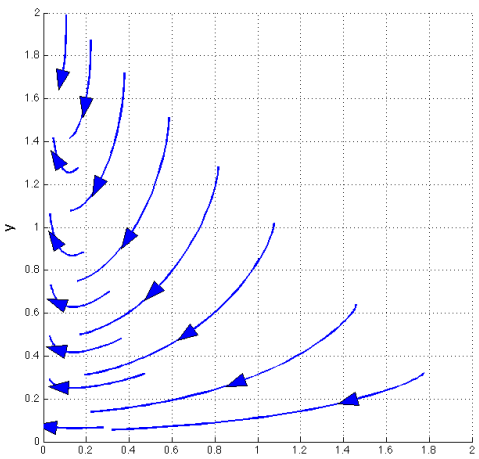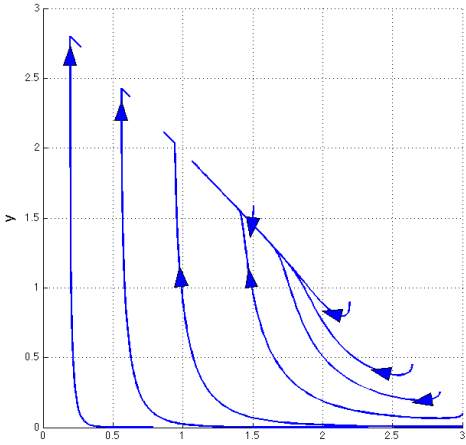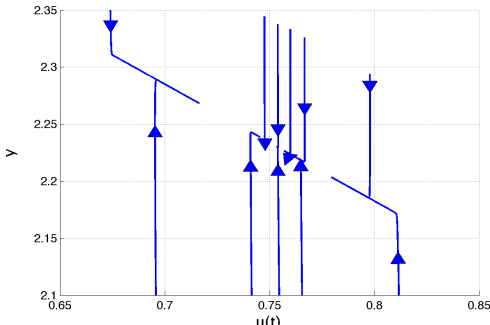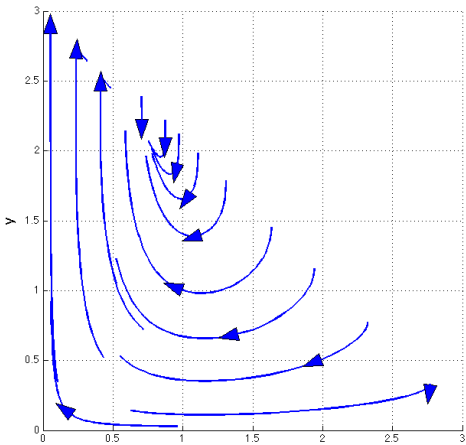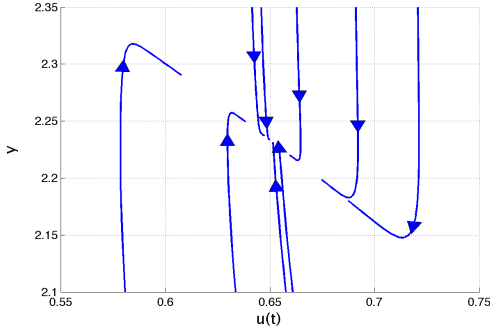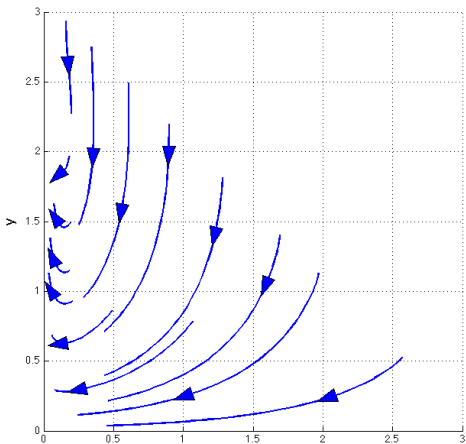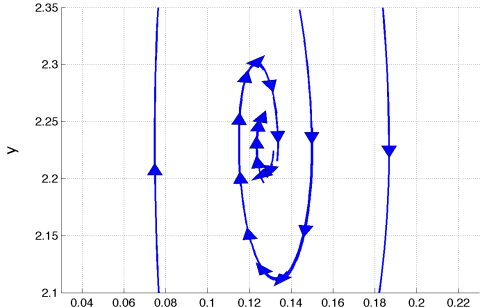
Appendix B

Phase Portraits
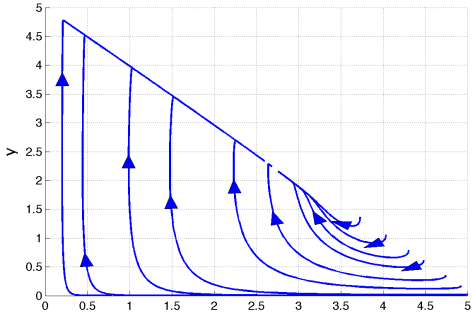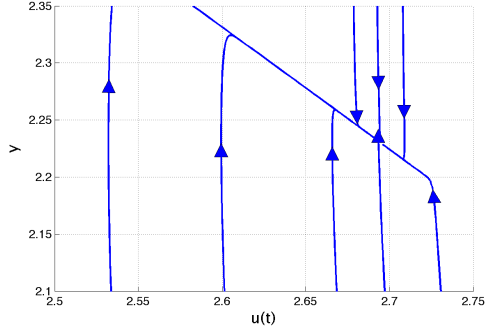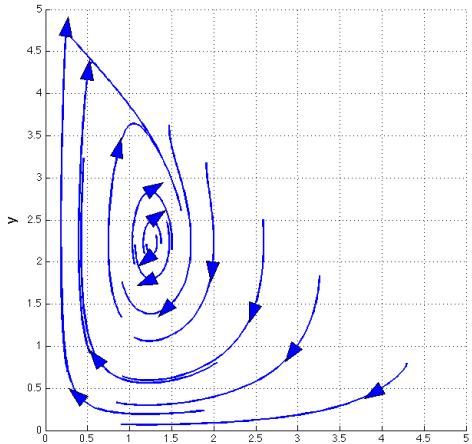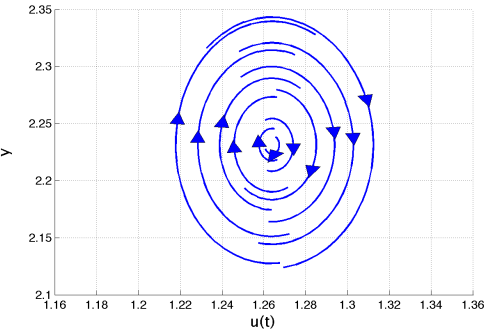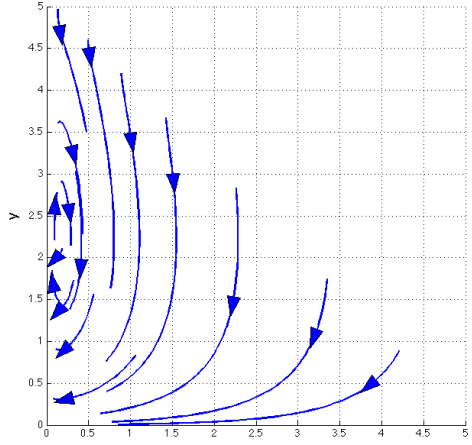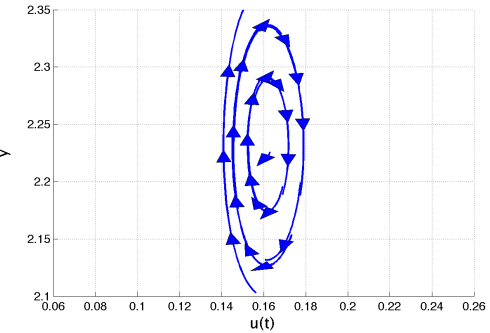
We created phase portraits of P versus Z using the nonlinear coupled NPZ equations without advection or diffusion (Equations 3.1). This appendix shows these phase portraits for $N_T = 2, 3, 5$, and 8 $\mu mol/L$. For the last three values, phase portraits are shown both for the full range of values as well as for a smaller range surrounding the analytical equilibrium point ($N_T = 2$ $\mu mol/L$ has an equilibrium point outside of the physical region and therefore is not shown). The x-axis is concentration of zooplankton Z while the y-axis is phytoplankton concentration P. The equilibrium points are listed for each depth level and N_T value. Only values under the line $P = N_T - Z$ are considered, as this defines the region where the solutions are physical (from the restriction $N_T = N + P + Z$).
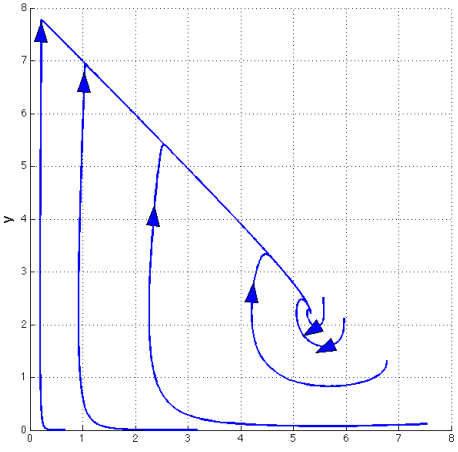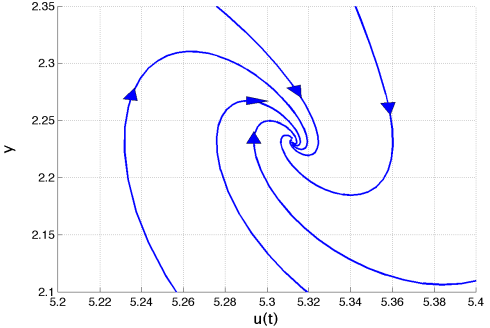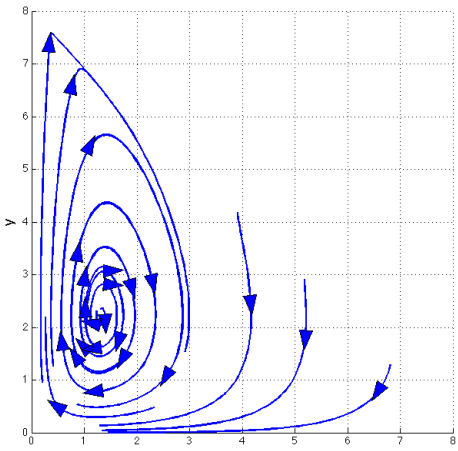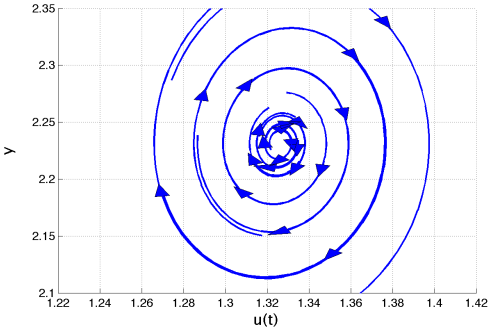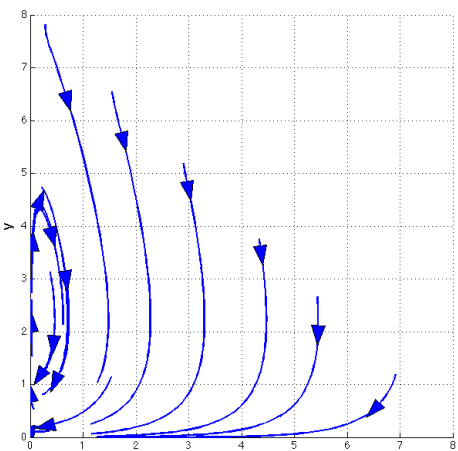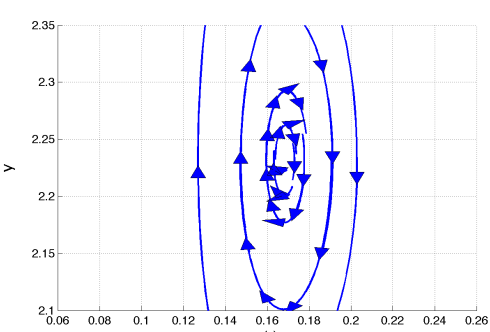
Stability	$z = 0m$	$z = -25m$	$z = -50m$
$N_T = 2$ $\mu mol/L$	U	U	U
$N_T = 3$ $\mu mol/L$	S	S	S
$N_T = 5$ $\mu mol/L$	S	U	U
$N_T = 8$ $\mu mol/L$	S	U	U

Table B.1: Predicted stability of the phase portraits for P versus Z.

$N_T = 2$	Equilibrium Point	Whole Range $x-$axis is Z, $y-$axis is P	Around Equilibrium Point $x-$axis is Z, $y-$axis is P
z=0	P=2.2314, Z=-0.2306 Unstable		N/A
z=-25	P=2.2314, Z=-0.2283 Unstable		N/A
z=-50	P=2.2314, Z=-0.2208 Unstable		N/A

$N_T = 3$	Equilibrium Point	Whole Range $x-$axis is Z, $y-$axis is P	Around Equilibrium Point $x-$axis is Z, $y-$axis is P
z=0	P=2.2314, Z=0.7524 Stable		
z=-25	P=2.2314, Z=0.6514 Stable		
z=-50	P=2.2314, Z=0.127 Stable		

$N_T = 5$	Equilibrium Point	Whole Range $x-$axis is Z, $y-$axis is P	Around Equilibrium Point $x-$axis is Z, $y-$axis is P
z=0	P=2.2314, Z=2.6934 Stable		
z=-25	P=2.2314, Z=1.2639 Unstable (Almost Neutral)		
z=-50	P=2.2314, Z=0.1619 Unstable		

$N_T = 8$	Equilibrium Point	Whole Range $x-$axis is Z, $y-$axis is P	Around Equilibrium Point $x-$axis is Z, $y-$axis is P
z=0	P=2.2314, Z=5.3123 Stable		
z=-25	P=2.2314, Z=1.3259 Unstable		
z=-50	P=2.2314, Z=0.1687 Unstable		

Bibliography

[1] World ocean atlas 2005, data sets and products. *http://www.nodc.noaa.gov/OC5/WOA05/*, 2005.

[2] Multidisciplinary simulation, estimation, and assimilation systems. *http://modelseas.mit.edu/*, 2009.

[3] A Agarwal. Statistical field estimation and scale estimation for complex coastal regions and archipelagos. *SM thesis, MIT*, 2009.

[4] A Arakawa and V Lamb. Computational design of the basic dynamical processes of the ucla general circulation model. *General circulation models of the atmosphere*, Jan 1977.

[5] R Barber and M Hiscock. A rising tide lifts all phytoplankton: Growth response of other phytoplankton taxa in diatom-dominated blooms. *Global Biogeochem. Cycles*, 20, Jan 2006.

[6] ŞT Beşiktepe, PFJ Lermusiaux, and A Robinson. Coupled physical and biogeochemical data-driven simulations of massachusetts bay in late summer: real-time and postcruise data assimilation. *Journal of Marine Systems*, 40:171–212, 2003.

[7] CC Chen, FK Shiah, S Chung, and K Liu. Winter phytoplankton blooms in the shallow mixed layer of the south china sea enhanced by upwelling. *Journal of Marine Systems*, Jan 2006.

[8] YLL Chen, HY Chen, and CW Chung. Seasonal variability of coccolithophore abundance and assemblage in the northern south china sea. *Deep-Sea Research Part II*, 54(14-15):1617–1633, 2007.

[9] SD Conte and C deBoor. *Elementary Numerical Analysis.* Apr 1972.

[10] K Cordero. Estimating integrated phytoplankton biomass in the seas around the philippines. *Unpublished Report*, 2007.

[11] G Cossarini, PFJ Lermusiaux, and C Solidoro. The lagoon of venice ecosystem: Seasonal dynamics and environmental guidance with uncertainty analyses and error subspace data assimilation. *J. Geophys. Res.*, pages 1–79, Apr 2009.

[12] D Cushing. *Upwelling and fish production.* Jan 1969.

[13] Benoit Cushman-Roisin. Introduction to geophysical fluid dynamics. Jan 1994.

[14] EW Dijkstra. A note on two problems in connexion with graphs. *Numerische Mathematik*, Jan 1959.

[15] MJR Fasham, HW Ducklow, and SM McKelvie. A nitrogen-based model of plankton dynamics in the oceanic mixed layer. *Journal of Marine Research*, 48:591–639, Dec 1990.

[16] W Fennel and T Neumann. *Introduction to the modelling of marine ecosystems.* Jan 2004.

[17] G Flierl. Mit course notes for 12.823: Modeling coupled physics and biology in the ocean. 2009.

[18] G Flierl and DJ McGillicuddy Jr. Chapter 4. mesoscale and submesoscale physical–biological interactions. *The Sea*, 12:1–74, Nov 2002.

[19] PJS Franks. Sink or swim: Accumulation of biomass at fronts. *Marine ecology progress series. Oldendorf*, Jan 1992.

[20] PJS Franks. Npz models of plankton dynamics: their construction, coupling to physics, and application. *Journal of Oceanography*, Jan 2002.

[21] PJS Franks and CC Chen. Plankton production in tidal fronts: a model of georges bank in summer. *Journal of Marine Research*, Jan 1996.

[22] H Gao, S Feng, and Y Guan. Modelling annual cycles of primary production in different regions of the bohai sea. *Fisheries Oceanography*, 7(3-4):258–264, 1998.

[23] M Griebel, T Dornseifer, and T Neunhoeffer. *Numerical simulation in fluid dynamics: a practical introduction.* Jan 1997.

[24] P Haley. Personal communication. 2009.

[25] P Haley, A Robinson, and WG Leslie. Real-time forecasting in the new england shelfbreak front: Primer97. *Ocean Sciences Meeting 1998*, Jan 1998.

[26] PJ Haley, PFJ Lermusiaux, A Robinson, WG Leslie, OG Logoutov, G Cossarini, XS Liang, P Moreno, SR Ramp, JD Doyle, J Bellingham, F Chavez, and S Johnston. Forecasting and reanalysis in the monterey bay/california current region for the autonomous ocean sampling network-ii experiment. *Deep-Sea Research Part II*, 2008.

[27] W Han, AM Moore, J Levin, B Zhang, and HG Arango. Seasonal surface ocean circulation and dynamics in the philippine archipelago region. *Dynamics of Atmospheres and Oceans*, Jan 2008.

[28] A Harten, B Engquist, S Osher, and SR Chakravarthy. Uniformly high order accurate essentially non-oscillatory schemes. *Journal of Computational Physics*, 71(2):231–303, 1987.

[29] M Hayashi, T Yanagi, and ML Diego-Mcglone. Nitrogen cycling in manila bay during dry and rainy seasons. *Coastal Marine Science*, 2006.

[30] E Hofmann and M Friedrichs. Predictive modeling for marine ecosystems. *The Sea*, 2002.

[31] LE Holmedal and T Utnes. Physical-biological interactions and their effect on phytoplankton blooms in fjords and near-coastal waters. *Journal of Marine Research*, 64(1):97–122, Jan 2006.

[32] S Kimura, A Kasai, H Nakata, T Sugimoto, JH Simpson, and JVS Cheok. Biological productivity of meso-scale eddies caused by frontal disturbances in the kuroshio. *ICES Journal of Marine Science*, 54(2):179, 1997.

[33] CM Lalli and TR Parsons. *Biological Oceanography: An Introduction*. Jan 1997.

[34] PFJ Lermusiaux. Personal communication. *2009*.

[35] PFJ Lermusiaux. Adaptive modeling, adaptive data assimilation and adaptive sampling. *Physica D: Nonlinear Phenomena*, Jan 2007.

[36] PFJ Lermusiaux and A Robinson. Data assimilation via error subspace statistical estimation. *Monthly Weather Review*, Jan 1999.

[37] OG Logoutov. A multigrid methodology for assimilation of measurements into regional tidal models. *Ocean Dynamics*, 58(5-6):441–460, Jan 2008.

[38] OG Logoutov and PFJ Lermusiaux. Inverse barotropic tidal estimation for regional ocean applications. *Ocean Modelling*, Jan 2008.

[39] D Macías, AP Martin, J Garca Lafuente, CM Garca, A Yool, M Bruno, A Vázquez-Escobar, A Izquierdo, DV Sein, and F Echevarra. Analysis of mixing and biogeochemical effects induced by tides on the atlantic–mediterranean flow in the strait of gibraltar through a physical–biological coupled model. *Progress in Oceanography*, 74(2-3):252–272, 2007.

[40] DJ Mackey, J Parslow, HW Higgins, FB Griffiths, and JE O'Sullivan. Plankton productivity and biomass in the western equatorial pacific: biological and physical controls. *Deep-Sea Research Part II*, 42(2-3):499–533, 1995.

[41] L Meñez, CL Villanoy, and LT David. Movement of water across passages connecting philippine inland sea basins. *Science Diliman*, 2006.

[42] MSEAS. Mseas philex website. *http://modelseas.mit.edu/Research/Straits/*, 2009.

[43] MSEAS. Mseas real time results from philex iop09. $http$: $//mseas.mit.edu/Sea\_exercises/Philex\_IOP09/$, 2009.

[44] NOAA. Oceanwatch las. *http://oceanwatch.pifsc.noaa.gov/las/servlets/dataset*, 2009.

[45] Joseph Pedlosky. Geophysical fluid dynamics. Jan 1998.

[46] WH Press. *Numerical recipes in C/C++: The Art of Scientific Computing.* Jan 2002.

[47] W Reed and T Hill. Triangular mesh methods for the neutron transport equation. *Los Alamos Report LA-UR-73-479*, Jan 1973.

[48] A Robinson, P Haley Jr, and PFJ Lermusiaux. Application of the generic harvard ocean prediction system (hops) to real-time forecasting with adapative sampling off the central california coast during aosn-ii. *people.seas.harvard.edu*, Jan 2004.

[49] A Robinson and PFJ Lermusiaux. Data assimilation for modeling and predicting coupled physical-biological interactions in the sea. *The Sea*, 2002.

[50] IR Santos, WC Burnett, T Dittmar, IGNA Suryaputra, and J Chanton. Tidal pumping drives nutrient and dissolved organic matter dynamics in a gulf of mexico subterranean estuary. *Geochim Cosmochim Ac*, 73(5):1325–1339, Jan 2009.

[51] CW Shu. Essentially non-oscillatory and weighted essentially non-oscillatory schemes for hyperbolic conservation laws. *Advanced Numerical Approximation of Nonlinear Hyperbolic Equations*, 1697:325–432, 1997.

[52] R Signell. Tidal dynamics and dispersion around coastal headlands. *WHOI/MIT Joint Program PhD Thesis*, Jan 1989.

[53] WHF Smith and DT Sandwell. Global seafloor topography from satellite altimetry and ship depth soundings. *Science*, 277:1957–1962, 1997.

[54] R Stewart. *Introduction to Physical Oceanography.* Jan 2003.

[55] S Takeda, N Ramaiah, M Miki, Y Kondo, Y Yamaguchi, Y Arii, F Gómez, K Furuya, and W Takahashi. Biological and chemical characteristics of high-chlorophyll, low-temperature water observed near the sulu archipelago. *Deep-Sea Research Part II*, 54(1-2):81–102, 2007.

[56] R Tian, PFJ Lermusiaux, James McCarthy, and A Robinson. A generalized prognostic model of marine biogeochemical-ecosystem dynamics: Structure, parameterization, and adaptive modeling. *Harvard Reports in Physical/Interdisciplinary Ocean Science #67*, May 2004.

[57] M Ueckermann. Personal communication. *2009.*

[58] M Ueckermann, PJ Haley, and PFJ Lermusiaux. Towards structured and unstructured data assimilative modeling systems for regional physical biogeochemical dynamics. *Seventh International Workshop on Unstructured Grid Numerical Modelling of Coastal, Shelf and Ocean Flows. Dartmouth, Nova Scotia*, 2008.

[59] J Xu, PFJ Lermusiaux, P Haley, and W Leslie. Spatial and temporal variations in acoustic propagation during plusnet-07 exercise in dabob bay. *Proceedings of meetings on acoustics (POMA)*, Jan 2008.

[60] J Xu, K Yin, L He, X Yuan, A Ho, and P Harrison. Phosphorus limitation in the northern south china sea during late summer: Influence of the pearl river. *Deep-Sea Research Part I*, Jan 2008.

[61] M Zorzano, H Mais, and L Vazquez. Numerical solution of two dimensional fokker—planck equations. *Applied Mathematics and Computation*, Jan 1999.